# A Metal Percolation Path in Metal/Semiconductor Composites and its Effect on Electric Conductivity in Different Ambiances

by

**Fen Qin**

Undergraduate degree, East China University of Science and Technology, 2013

Master's degree, University of Pittsburgh, 2016

Submitted to the Graduate Faculty of the

Swanson School of Engineering in partial fulfillment

of the requirements for the degree of

Doctor of Philosophy

University of Pittsburgh

2020

UNIVERSITY OF PITTSBURGH

SWANSON SCHOOL OF ENGINEERING

This dissertation was presented

by

**Fen Qin**

It was defended on

March 19, 2020

and approved by

Ian Nettleship, PhD, Associate Professor, Department of Mechanical Engineering and Materials Science

Wei Xiong, PhD, Assistant Professor, Department of Mechanical Engineering and Materials Science

Mostafa Bedewy, PhD, Assistant Professor, Department of Industrial Engineering

Dissertation Director: Jung-kun Lee, PhD, Professor, Department of Mechanical Engineering and Materials Science

Copyright © by Fen Qin

2020

# A Metal Percolation Path in Metal/Semiconductor Composites and its Effect on Electric Conductivity in Different Ambiances

Fen Qin, PhD

University of Pittsburgh, 2020

Semiconducting oxides, owing to their unique electrical and chemical properties have been widely investigated and used as electrodes for renewable and sustainable energy system. Nevertheless, several limitations of semiconducting oxides electrodes still exist. One inherent problem is that the electric conductivity is relatively low and dependent on ambiance. This can be resolved by designing a composite with a complementary metal component.

This study is focused on the design, fabrication and characterization of metal - oxide composite with the desired configuration of a metal component and the stable electrical conductivity of the composite electrode, aiming to meet stringent requirements of energy devices including the interconnector of solid oxide fuel cells (SOFCs) and the transparent conductor (TC) of solar cells.

First, the crystallization of $(La_{1-x}Sr_x)MnO_3$ (LSM) was controlled using microwave radiation and its effect on the grain growth and electrical properties of LSM ceramics was studied. Second, Ni particles were added to LSM matrix to form a percolation path that maintains high electric conductivity in reducing ambiance. The addition of Ni particles also changed the sintering behavior of LSM ceramics using a self-induced liquid phase. The size of initial Ni particles was a critical factor influencing the formation of the percolation path and the appearance of the self-induced liquid phase. A stack of composite layers was tested as the interconnector of fuel cells by

exposing two ends to oxidizing/reducing ambiance. Compared with LSM interconnector, this new interconnector showed high conductivity at the simulated operating condition of SOFCs.

Moreover, an effect of aspect ratio of a metal component on the electric conductivity was explored. In LSM:Ni composites, a percolation threshold was reduced by employing highly anisotropic Ni particles. This concept is also applied to ZnO film to increase its electric conductivity and reduce its dependence on the ambiance. A series of experimental and computational results show that ZnO/Ag NW is a promising indium-free and affordable alternative to ITO.

Overall, this dissertation showed detailed mechanisms underlying the excellent electric conductivity and good optical transparency of the metal – oxide composites and shed light onto the design rule of the electrode for different renewable energy devices.

# Table of Contents

# List of Tables

# List of Figures

# Preface

Words are powerless to express my sincere gratitude to the people who have been so supportive and helpful during my graduate life in University of Pittsburgh.

Above all, I would like to thank my advisor, Professor Jung Kun Lee, for guiding and supporting me over the years. I truly appreciate his passion and for his willingness to share his passion with the students. He played an important role in shaping my research development and critical thinking. He always gave many inspirational suggestions to his students and helped them to purse success in their research by themselves. His knowledge and leadership provided us with a priceless impact.

I would also express my appreciation to my esteemed committee members, Professor Ian Nettleship, Professor Wei Xiong and Professor Mostafa Bedewy. Their comments, kindness and thoughtful reviews on my dissertation always guided me to finish my PhD research life.

My thanks also go to my present and past lab members, also my precious friends, Dr.Po-shun Huang, Dr.Ziye Xiong, Dr.Gillsan Han, Dr.Salim Caliskan, Dr. Matthew Lawrence Duff, Dr.Hee-Suk Roh, Dr.Hyun-Woo Shim, Seongha Lee and Yulin Liu who helped me, encouraged me and made my research life full of pleasures. I feel so blessed and lucky to have these intelligent, friendly and hardworking people in my life. The laboratory environment was always enjoyable and productive with collaboration, discussion and encouragement.

Moreover, I'm much obliged to Department of Mechanical Engineering and Materials Science, Nano-Scale Fabrication and Characterization and Material Science Characterization Lab staffs for their assistance and efficient work.

Finally, I want to specially thank my family members for their endless love and understanding. I’m extremely grateful for all what they have done for me. They would like to travel thousand miles just to see me and be with me whenever I needed them and they always showed their greatest support on any decisions that I made.  Words can never be enough to describe how much I love my family.

# 1.0 Introduction

## 1.1 Needs for Clean and Sustainable Energy

In the effort to slow down the climate change, a clean energy evolution is taking place steadily all over the world. It is forecasted that energy-related $CO_2$ emission must to decline 70% below todays' level to tackle global warming and meet our climate goals.[1] Renewable energy, involving natural phenomena – sunlight, wind or hydropower, will power at least half of the globe in next 30 years to meet the climate goal.[1-2] Additionally, renewable energy, replenished from natural process, is abundant to meet the growing demand of energy nowadays and in future. It is inexhaustible with modest impact on environment. Recently, the cost-competitiveness of renewables has been significantly improved. The advantages of fossil fuels on costs have been weakened, as shown in Figure 1.1.[3] Traditional fuels are gradually beaten out of the market by more affordable renewables with no subsidies. However, together with costs, renewables will conjointly need to improve its efficiency.

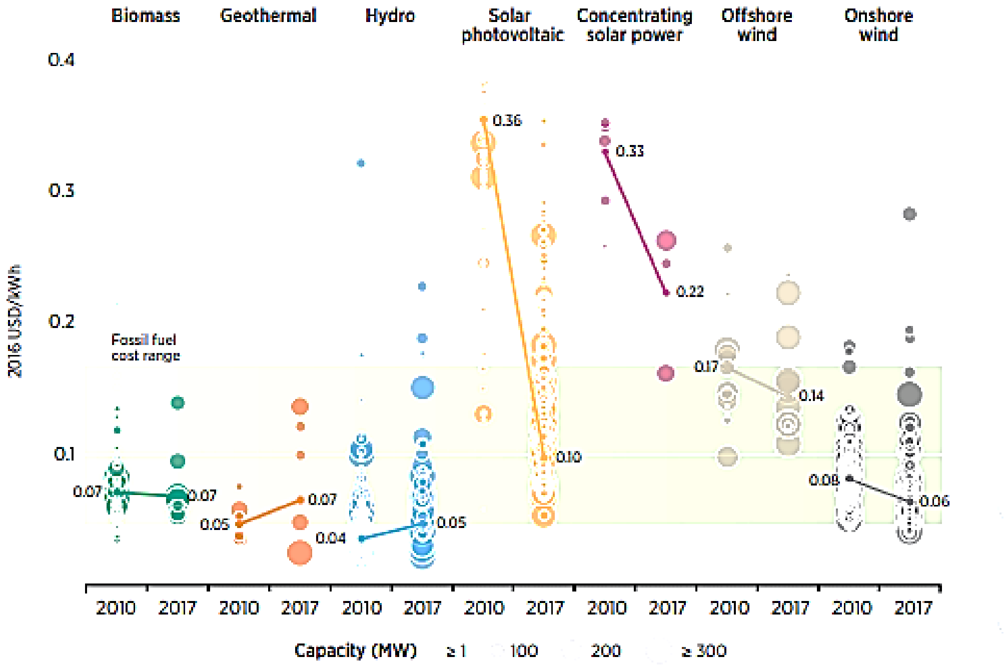

**Figure 1.1 Global cost of electricity from utility-scale renewable power generation technologies 2010-2017** [3]

Massive progress has been made in decarbonizing the electricity power industry, notably with the emerging electrical generation and storage facilities. Solar power plants generate the electricity from day-time sunshine and store the heat in molten salts or other media to compensate the electricity stability after sunset.[4-5] Fuel power plants can generate electricity from hydrogen as fuel. The excess electricity reversibly used to generate hydrogen. These smart technologies allow for providing undisrupted power by intermitted energy supply.[6-7] The performance of electrodes under operation conditions could make the most important contribution to improve the renewable efficiency. With wide variety of ongoing researches, it is promising to lower the ohmic loss and permit greater flexibility as the shares of sustainable and renewable energy develops.

## 1.2 Transition Metal Oxides

Transition metal oxides hold the inherent multivalent nature. In contradiction of traditional semiconductors, they have higher likelihood of carrier self-trapping. Their conduction mechanisms can be explained by band theory, large polaron or small polaron mechanism. This chapter concludes the carrier transport in mono-oxides (AO), di-oxides ($AO_2$), perovskite oxides ($ABO_3$) and spinel oxides ($AB_2O_4$) with increased electronic complexity of transition metal cations.

### 1.2.1 Extrinsic Defects in Transition Metal Oxides

Extrinsic transition metal oxides are materials with impurities, donors or acceptors, which introduced into lattice to possess the unique electrical properties. They are promising components of renewable devices, such as solar cells, transistors and sensors. Before doping, transition metal oxides, like $TiO_2$, $MoO_3$, NiO, and ZnO have shown many promises in the renewable technologies. The popularity of these materials is mainly caused by tunability of intrinsic defects. The defects, such as vacancies, interstitial defects and anti-site defects, are neutralized by the formation of electrons/holes. Doping process is an effective approach to enhance carrier concentration via extrinsic defects. If a semiconductor is doped with donors, it is known as n-type semiconducting materials. The majority charge carriers are electrons and the activation energy for electrons is donated by the impurities. Additional electrons may be easily promoted into the conduction band with a much smaller energy, shown in Figure 1.2. A donor level in the band gap near the conduction band can be formed. In contrast, if a semiconductor is doped with acceptors, it is recognized as p-type semiconductors. The majority charge carriers are holes and the activation energy for electrons is accepted to impurities. More holes are introduced into the valence band. An acceptor level near valence band is formed, leaving holes to propagate through. Therefore, as dopant concentration increases, the conductivity for n-type or p-type semiconductors is expected to increase.

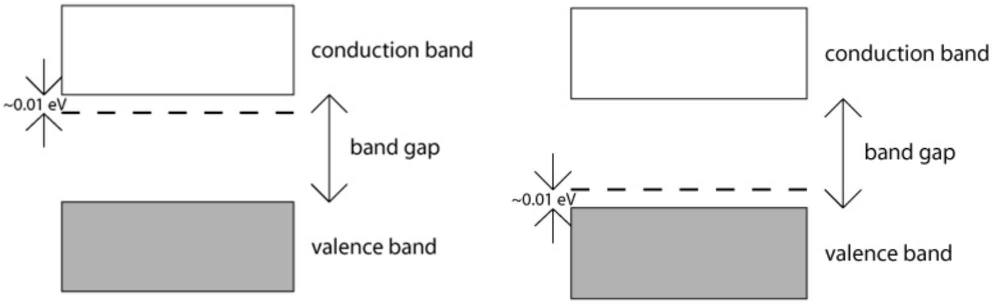

**Figure 1.2 Schematics of n-type semiconductor and p-type semiconductor**[8]

### 1.2.2 Transition Metal Oxide with $ABO_3$ Perovskite Structure

Perovskite-type oxides, in a general formula $ABO_3$, form an important class of materials of great technical value renewable energy applications due to their wide spectrum of physical properties. Ideally, perovskite oxides have relatively simple crystal structure with a cubic unit, shown in Figure 1.3.[9] Depending upon the value of tolerance factor, which governed by the relation among A, B and O ionic radius, crystal structure commonly turns into rhombohedral or orthorhombic structure after lattice distortion.

Moreover, the modification on structural, electrical or magnetic properties can also be completed by considerable doping on one or both cation sites. For instance, $La_{1-x}Sr_xMnO_3$, low valence $Sr^{2+}$ substitution on A site increases the carrier concentration. Charge neutrality is maintained by the oxidation of $Mn^{3+}$ into $Mn^{4+}$ on B-site. The coupling pairs makes it susceptible to polaron formation. The compositional change has an impact on the sintering behavior as well as the electric conductivity, since it controls the diffusion of ions at high temperature.[10-11] Vacancies of slow diffusing ions can accelerate the grain growth and densification of the perovskite oxides.

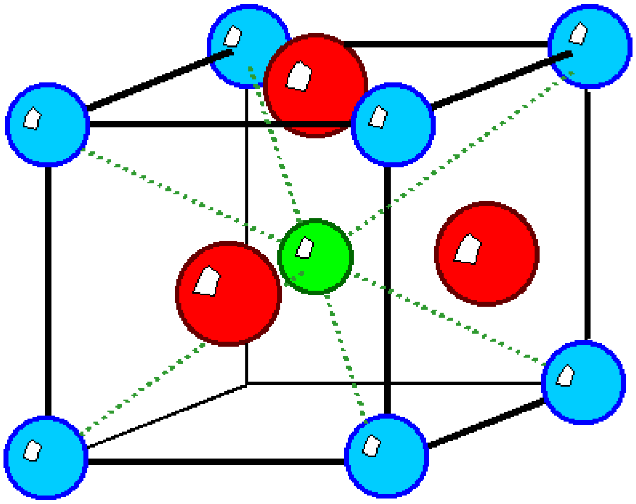

**Figure 1.3 Perovskite crystal structure $ABO_3$ (green – B; O – red; A – blue).** [9]

### 1.2.3 Transition Metal Oxide with $AB_2O_4$ Spinel Structure

Transition metal oxides of spinel structure $AB_2O_4$, sometimes also named as layered perovskite, display intriguing electric properties at high temperature as first reported by Larring and Norby.[12] Up to now, many spinel oxides, with different combination of A and B cations, have been generated and investigated for their unique physical and chemical properties, such as conductivity, corrosion resistance and variable thermal expansion coefficient. Eight tetrahedral sites and four octahedral sites are involved in a closed-packed oxygen lattice. Most spinel oxides have cubic structure shown in Figure 1.4. In the case of transition metal, for example $Mn_xCo_{3-x}O_4$, the crystal lattice distorts into a tetragonal structure due to Jahn-Tell effect.

The major conduction mechanism of spinel oxides can be explained as hopping of polarons between octahedral sites. Therefore, the oxidation status of octahedral cations is of importance. A mixed cation distribution on the octahedral lattice site is preferred for higher conductivity. For example, in $Fe_3O_4$ spinel oxide, $Fe^{2+}$ and $Fe^{3+}$ are evenly distributed in the octahedral sites, thereby its conductivity is over 100 S/cm even at room temperature. An excellent electrical conductivity has been observed in Cu-Mn spinel system. Stoichiometric $CuMn_2O_4$ shows a conductivity around 53 S/cm at 800 $^oC$. The conductivity is boosted to 225 S/cm by changing the composition to Cu-rich spinel $Cu_{1.3}Mn_{1.7}O_4$.[14]

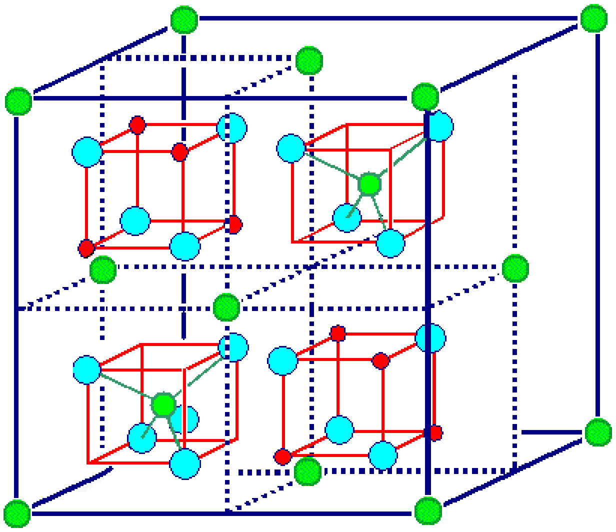

**Figure 1.4 Spinel crystal structure $AB_2O_4$ (green – B; A – red; O – blue).** [13]

## 1.3 Current Applications and Issues

### 1.3.1 Solid Oxide Energy Conversion Systems

Solid oxide conversion system, including solid oxide fuel cells (SOFCs) and solid oxide electrolysis cells (SOECs) is very potent technology for renewable and sustainable purpose. Moreover, efforts have been made on the development of reversible solid oxide cells, which can be alternatively operated in either fuel cell mode or electrolysis mode.[14-15] The operating principles of single SOFC cell and SOEC cell are illustrated in Figure.1.5. Both cells are consisted of three basic components, anode, electrolyte and cathode. Anode is exposed to reducing ambiance, while cathode is exposed to oxidizing ambiance. In fuel cell mode, electricity is generated by the electrochemical combination of fuel, such as $H_2$, $CH_4$. In electrolysis mode, hydrogen is decomposed from water. Currently, Yttria-Stabilized Zirconia (YSZ) is the most commonly used electrolyte materials. The operation temperature for SOFCs/SOECs is usually as high as 600-900$^{o}$C to achieve the excellent anionic conduction performance.

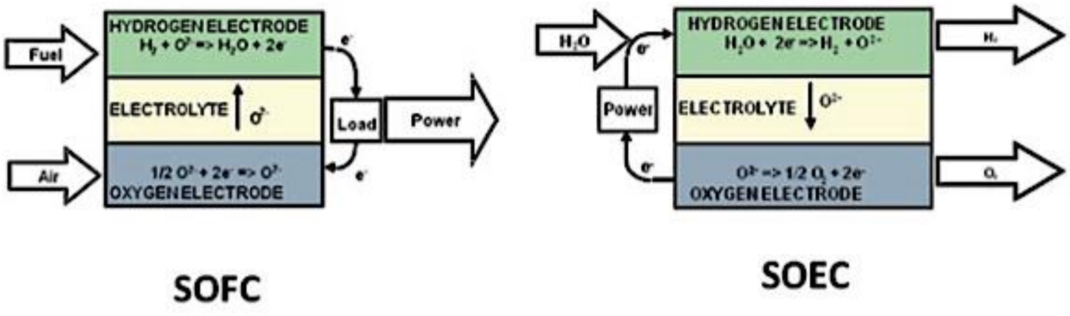

**Figure 1.5 Operation illustration of SOFCs and SOECs.**[15]

The power generated by single cell is limited and insufficient to reach large output for real applications. Accordingly, hundreds or thousands of cells are stacked and united from one end to the other with electrical connection, named interconnect to fulfill the power requirement of the applications. As shown in Figure 1.6, the SOFC power systems can provide power from 1W to 200MW. The interconnect is of great significance to transport electricity, seal and maintain the ambient difference. Metallic interconnect such as Cr-rich ferritic stainless steel (Crofer®) are good interconnect candidate for intermediate SOFCs.[16] In electrolysis mode, the interconnect has to be exposed to high temperature (above 800 °C) with high humidity. In such an environment, Cr evaporation towards fuel side along with the formation of oxidization layer in oxidant side are hardly to be neglected. The evaporated Cr species poisons the entire system and could lead to the severe degradation of the cell. In addition, the oxidation layer is resistive and holds quite different thermal expansion coefficient with metallic interconnect. Warping, cracking or other physical and mechanical failure would take place consequently.[17] To address this problem, ceramics-based materials are preferred for high temperature SOEC application with excellent chemical and mechanical stability at high operation temperature in severe corrosive environment.

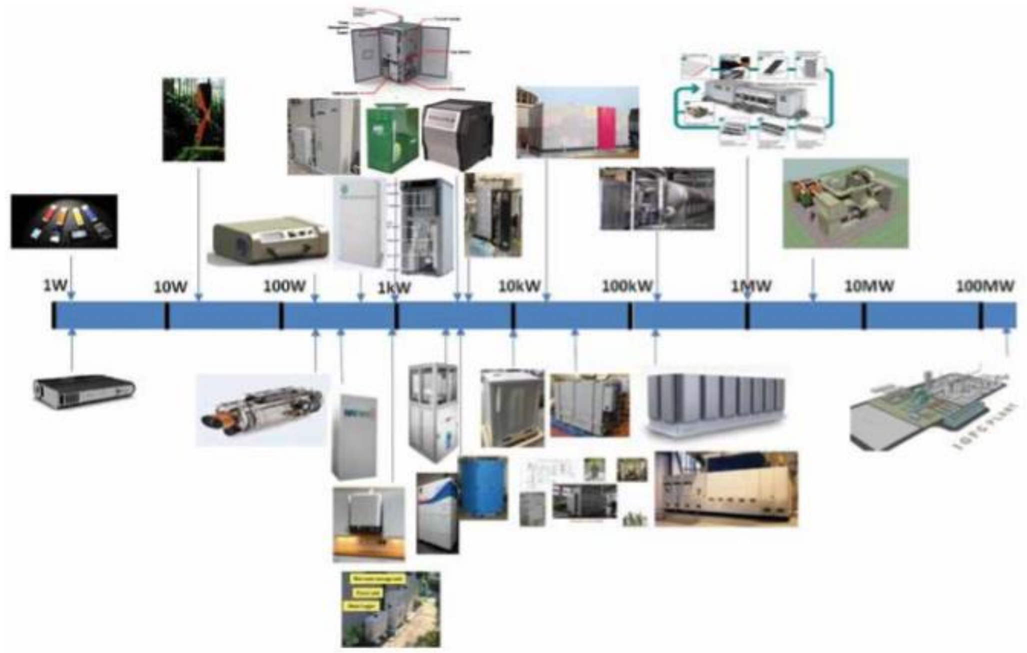

**Figure 1.6 A wide variety of SOFC power systems** [18]

### 1.3.2 Photo-voltaic System

The interest in materials offering both electrical conductivity and optical transparency has been intensified recently. There is a great need for a top electrode of photovoltaic devices, such as solar cell or touch panel, providing low resistivity and simultaneously high transparency to permit light in the visible portion of spectrum to pass through. In addition, chemical stability, costs, sustainability and sometimes flexibility are also taken into consideration for the materials to be amenable to commercial production. Extensive efforts have been taken to meet all the stringent requirements. As asserted previously, transition metal oxides with wide band gaps greater 3.1 eV may be the solution.[19] In the past several decades, Indium doped Tin oxide (ITO) has been the dominant materials used as transparent and conductive oxides (TCOs) with a sheet resistance as low as 10ohm/sq and transmittance above 80%, which becomes the standard requirement for transparent electrodes. Other post-transition metal oxides, ZnO ,$In_2O_3$, SnO are widely studies as TCOs. Many researches have gone into investigating the n-type TCOs such as Al/Ga doped ZnO or F/Sb doped $SnO_2$. [20] Due to their wide bandgap, excellent metal-oxide orbital overlap and deep conduction band minimum (CBM), these oxides are transparent in spectrum of visible light range and even in the NIR range after heavily doping with high mobility and dopability.[21] Recently, it has also been reported that ternary oxides such as $SrTiO_3$, $SrSnO_3$ or $Cd_3TeO_3$ can also be considered as alternative plasmonic component. [22]

The rare earth metals, In or Ga, are considered to have a high supply risk in the future. In the past decade, the world production of indium metal has risen from 300 to 700 tons/year.[23] Replacement of ITO electrodes with other earth abundant elements is of importance. As it stands, the main issue of TCs is the trade-off between optical transparency and sheet resistance, shown in Figure.1.7. The challenge still remains to find such a film with comparable optical transmittance and low resistance to ITO. Only few doped oxides or metal nanowires/mesh in the Figure 1.7 displays in the left top corner. The idea of nano-metal/oxide composite may be the solution to improve the electrical conductivity of oxide matrix. Besides, a work function alignment with other component of the devices, such as hole transport layer (HTL), is expected to enhance the electron injection and thereby improve the energy efficiency of photovoltaic devices.[24-25] Furthermore, modern design requires advanced mechanical properties. Curved or flexible electrodes are desired in the OLED or solar cells.

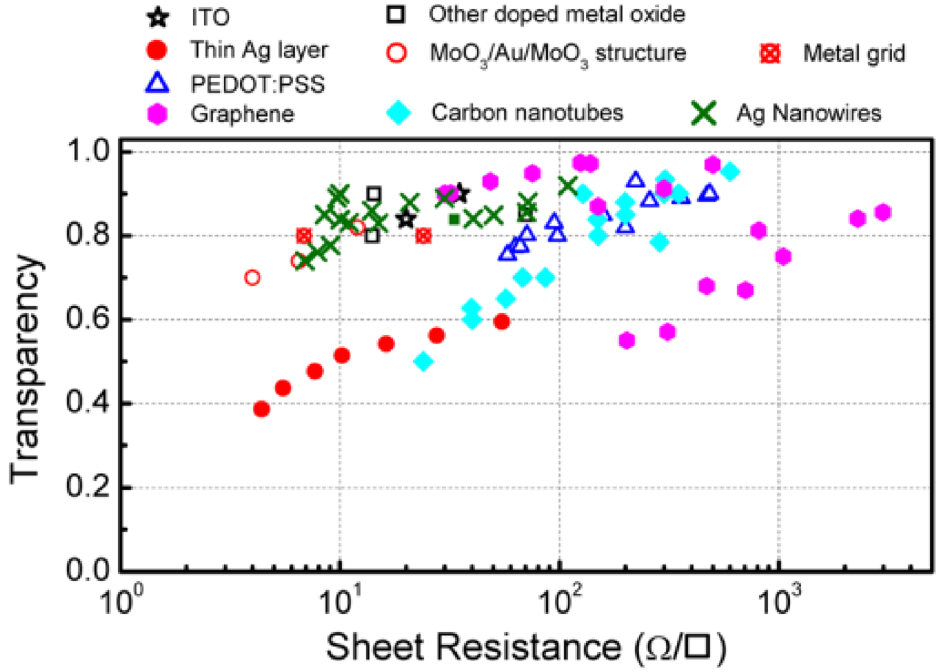

**Figure 1.7 The trade-off between optical transparency and sheet resistance.** [26]

### 1.3.3 Gas Sensor System

Transition metal oxide gas sensors has also been extensively studied based on the gas detecting process that is related to surface reaction. When operated in operation condition, like room temperature in air, the electrical resistance of the materials changes dramatically on contact with even a small amount of target gas. The sensitivity of the materials enables us to detect the concentration of target gas based on the electrical resistance. Additionally, theses metal oxides sensors are usually lower in costs and smaller in size, which improve the extensions to more portable applications in real world easily. Tremendous efforts of scientific community have been taken to transition metal oxides due to their wide variety of electronic structures, especially for those with $d_0$ and $d_{10}$ configurations, such as $TiO_2$, $V_2O_5$, $WO_3$ or ZnO and $SnO_2$.[27] In order to facilitate the understanding, the basic principle has been schematically represented in Figure 1.8.

Band gap changes with composition at the surface of the grain with and without the targeting gas CO. When exposed in CO, $CO_2$ is formed by oxidation and electrons are left near grain boundaries. Accordingly, space charging gap declines and the Schottky Barrier at grain boundary is lowered to form the electrons percolation paths. It is noticeable that this conduction mechanism is only for n-type semiconductors when grain size is larger than the depletion gaps.

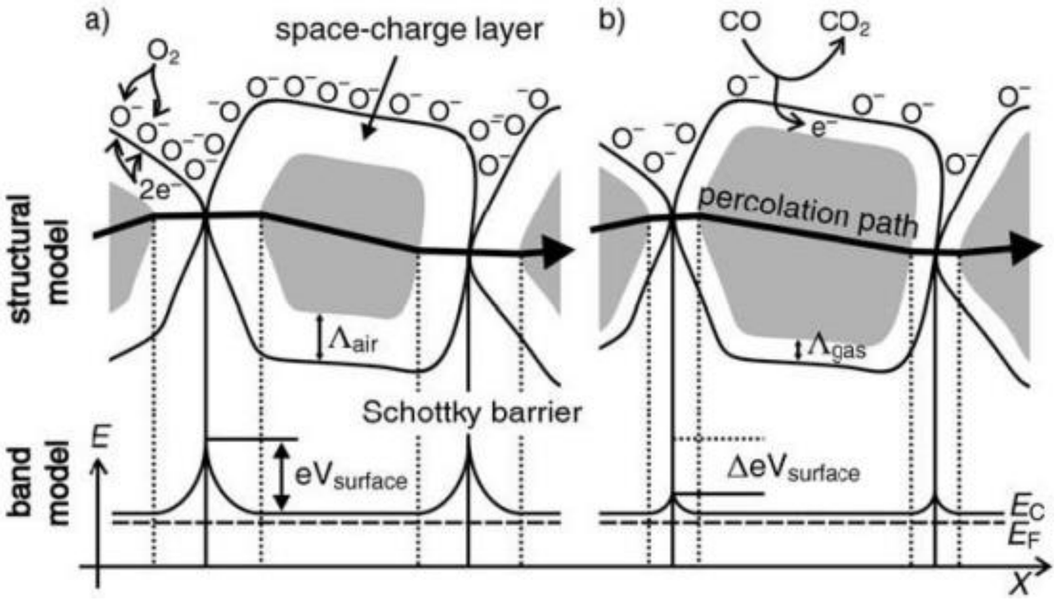

**Figure 1.8 Structural and band changes with and without target gas, CO.**[28]

### 1.4 Nanostructure Metal Addition Strategy

Conductive materials/oxide composites have garnered interest in recent years for electrode materials that have to meet with specific requirements under operation conditions. The conductive filler, such as metallic nanoparticles, carbon nanotubes (CNTs) or reduced graphene oxide (rGO),[29-30] exhibit excellent electrical properties and also show improved optical, mechanical and other properties by nano-structural modification. Moreover, the electrical properties of oxides sometimes have strong dependency on ambient variant. For p-type oxides, such as Cuprate, the formation of oxygen vacancies has detrimental influence on the electrical properties by the dramatic suppression of carrier concentration. If the operation condition is oxygen-deficient, these materials failed to maintain high electrical conductivity as electrodes. Small amount of metallic addition may be the most feasible solution.[31-32] Metal additions, furthermore, are easily modified in shape, orientation, size and etc. to meet the requirements of specific operating conditions. The prominent advantage for nanostructured metallic addition is sharp increment in electrical conductivity. Production of low-cost and high-performance transition metal-based composite for specific working conditions is of importance and significant efforts have been made by researchers to enhance the properties by embedding metal nanostructures with shape-optimization into oxides matrix. According to certain applications and specific usage, the problems can be stated into different ways. In this study, we demonstrate the enhanced electrical properties and other physical and chemical properties by addition of nanostructured metal into transition metal oxide matrix.

### 1.4.1 Oxide/Metal Bilayer Electrodes

Oxide/metal bilayer is one of the most exploited design to reduce the contact resistance and improve the performance of devices. Ablat et al.[33] reported a change in the contact resistance of organic field-effect transistors (OFETS) when the oxide/metal electrodes are applied. In the study, $WO_3$/Ag, $MoO_3$/Ag, $WO_3$/Au and $MoO_3$/Au were found to effectively lower the contact resistance due to the favorable morphological and electronic structure of organic/metal oxide/metal interface.

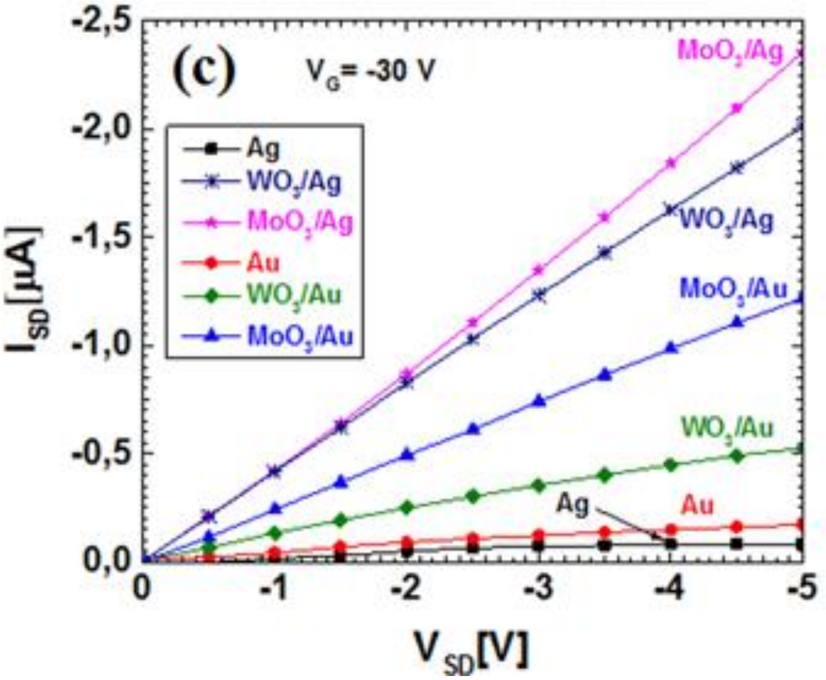

**Figure 1.9 Output curves (VGS = -30V) of OFETs devices (L=100um) with different contact.**[33]

### 1.4.2 Oxide/Metal/Oxide Sandwich-like Structure

As asserted previously, the conductivity of intrinsic metal oxides, such as ZnO, limits their practical application as transparent and conductive oxides. Meanwhile, metal thin film displays relatively low transparency with targeting absorption peak, but hold good electrical property. Therefore, various ultra-thin metal films, such as Ag, Au, Mo and Cu, have been embedded between the oxide films in order to find a compromise between the conductivity and transparency. FOM is a parameter which is developed to comprehensively evaluate the electric and optical performance of TC. Two standard FOMs (Fraser and Cook's FOM[34] and Haake's FOM[35]) are commonly used. They bring out a value by considering both transmittance and conductivity. It is noticeable that there is a tradeoff between transmittance and conductivity. By controlling the relative thickness of a metal layer, it is possible to find out the best FOM in the sandwich structure. Also, this structure provides the long-term stability over heat and humidity, since the metal layer is passivated by two oxide layers.

Cu films with 8nm in thickness embedded Al doped ZnO (AZO) film has high transmittance around 80% and low resistivity around $1.94\times10^{-2}$ $\Omega^{-1}$ [36] AZO/Mo/AZO films can achieve a really high FOM and low resistivity $2.23\times10^{-4}$ $\Omega^{-1}$ by tuning the thickness of oxide layer and metal layer. [37] In table 1.1, the values of Fraser Cook and Haacke FOM for different sandwich-structured composites with ultra-thin Au layer ~7nm in the middle, have been listed.

**Table 1.1 Oxide Semiconductors/ metal/ oxide semiconductors progress on FOM**

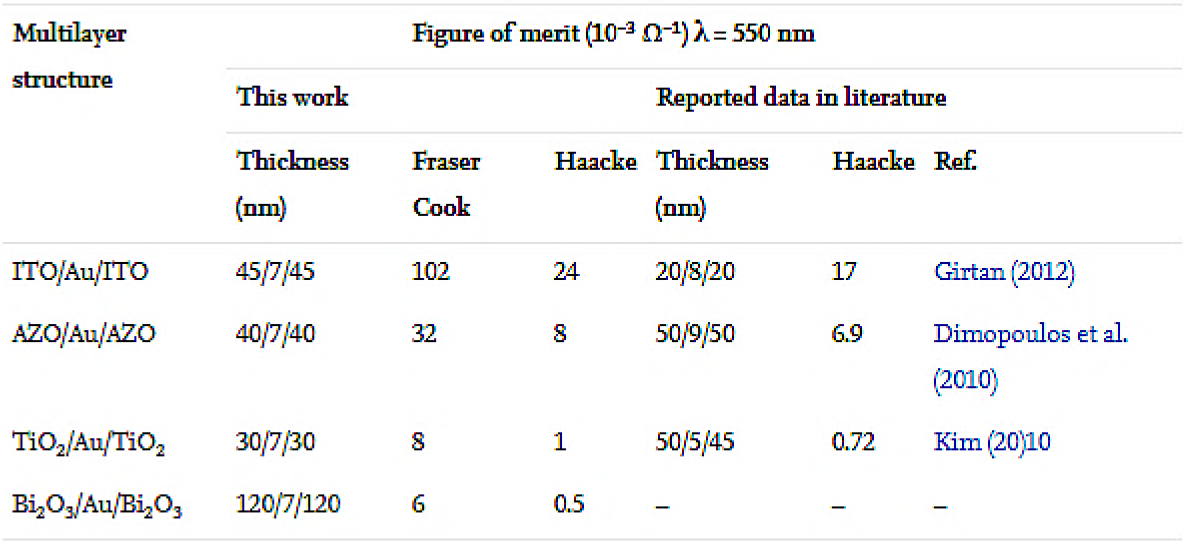

| Multilayer structure | Figure of merit ($10^{-3}$ $\Omega^{-1}$) $\lambda$ = 550 nm | | | | | |
|---|---|---|---|---|---|---|
| | This work | | | Reported data in literature | | |
| | Thickness (nm) | Fraser Cook | Haacke | Thickness (nm) | Haacke | Ref. |
| ITO/Au/ITO | 45/7/45 | 102 | 24 | 20/8/20 | 17 | Girtan (2012) |
| AZO/Au/AZO | 40/7/40 | 32 | 8 | 50/9/50 | 6.9 | Dimopoulos et al. (2010) |
| $TiO_2$/Au/$TiO_2$ | 30/7/30 | 8 | 1 | 50/5/45 | 0.72 | Kim (20)10 |
| $Bi_2O_3$/Au/$Bi_2O_3$ | 120/7/120 | 6 | 0.5 | – | – | – |

### 1.4.3 Random-Dispersed Nanostructure

Nanostructured metallic additions have remarkable electrical and optical properties due to their high conductance and surface plasmonic resonance. Their use as conductive fillers in oxide matrix is an alternative way to design the electrodes for renewable energy system. Furthermore, an increase in aspect ratio of metallic filler can further reduce the amount of metal needed for percolation. [30,31] Nanostructured metallic additions with various aspect ratio, noting as the ratio of length-to-width, and surface coverage, allow tuning of the transparency and electrical conductivity in a broad range. Silver nanowire (Ag NW) networks demonstrate to be a promising alternative to ITO films for photovoltaic devices due to its excellent low sheet resistance < 10ohm/sq and high transmittance ~ 88% at 550nm.[38] Furthermore, they also offer simple and low-cost fabrication and better flexibility.[39-40] It's pointed out that Ag NW networks face several issues, involving local oxidization, limited contact area and corrosion resistance. A protecting coverage of oxide may be the solution. Transparent and conductive oxides, ITO, ZnO or AZO, could effectively hold back the oxidation of Ag NWs. For instance, the sputtered ZnO has a sheet resistance $1.3\times10^5$ ohm/sq with a transmittance around 82% at 550nm; meanwhile a ZnO/AgNW/ZnO film has a sheet resistance 8 ohm/sq, that decreased several orders of magnitude, with an even higher transmittance 91.91%. [41] In addition, the composite of Ag NWs covered with ZnO showed mechanical flexibility and excellent performance in bending cycle test where ITO didn't preserve performance.

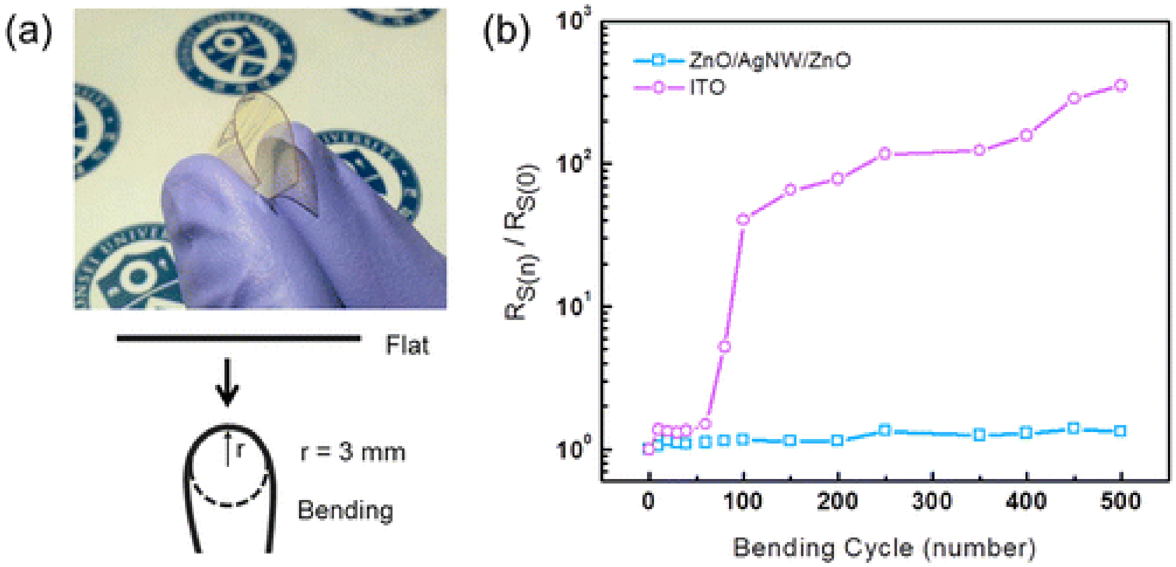

**Figure 1.10 The flexibility of oxide/metal/oxide film with lower sheet resistance than ITO** [4]

## 1.5 Thesis Outline

In this thesis, two different conducting oxides are modified by adding the nanostructured metal and their electric and optical properties are studied. Basic principles, motivations, experimental, result and discussion of each topic are presented in individual chapter.

Chapters 2 – 4 are dedicated to the electrical property and microstructure evolution of the (La,Sr)$MnO_3$ (LSM) - Ni composites for their potential application to the ceramic interconnect of SOECs:

a) The effect of powder preparation method on the sintering behavior, crystallinity and polaron hopping in LSM ceramics,

b) Effect of Ni size on the microstructure, phase evolution and electrical properties of for LSM:Ni composites,

c) The design of LSM/LSM:Ni double layer electrodes for the interconnect application in SOFCs/SOECs.

Chapter 2 provides background information on the properties of Sr doped LaMnO3 and how we are about to manipulate the electrical properties by synthesis method or Sr dopant amount. The major conduction mechanism for LSM is small polaron hopping mechanism. Therefore, the change in electrical properties is explained in details with the understanding of polaron hopping.

In Chapter 3, nanostructured Ni with different sizes are added into LSM to build the LSM:Ni composites as high temperature conductors in oxidizing or reducing atmosphere. Ni compensates the polarons loss of LSM in reducing ambiance to assist the composite to maintain high electrical conductivity. Ni size was reduced in regards to improvement on sintering behavior by a self-induced liquid phase sintering process.

In Chapter 4, LSM and LSM:Ni studied in Chapter2,3 are applied to build a double layer interconnect on YSZ:NiO anode support. Compositions of LSM and LSM:Ni are carefully selected to eliminate the shrinkage mismatch. The shrinkage of YSZ-NiO anode support further improves the densification of interconnect coating on the top. Then, the interfacial reaction between interconnect and anode is limited by fine tuning of A/B ratio of the perovskite structure. At the end, the feasibility of the double-layer interconnect on anode support is examined by the Area-specific-resistance (ASR) stability test in a dual atmosphere (air in one side, $H_2/N_2$ in the other side) at operation temperature.

Chapters 5 and 6 are focused on how a change in the aspect ratio of a metal component influences the formation of a percolation path, the electric conductivity and the tradeoff between the conductivity and the transparency:

a) Aspect ratio effect on LSM:Ni composite (AR = 0.1, 1 and 10),

b) Aspect ratio effect on Al:ZnO/Ag Nanowires composite (AR = 67~ 450),

The effect of aspect ratio of nanostructure metal additions on the properties of metal-conducting oxides for specific conditions has been discussed in this group. In Chapter 5, following the discussion in the previous chapter, the aspect ratio of Ni has been changed and studied. By 2-D smashing Ni spheres into Ni plates or by 1-D elongation Ni seeds into Ni nanowires, the aspect ratio Ni nanostructured additions was changed and monitored to reduce the percolation threshold of Ni in LSM:Ni composite. Eventually, less amount of Ni is expected to be added into LSM:Ni to solve the trade-off problems between electrical conductivity and sintering inhibitor behavior of Ni.

In Chapter 6, the effect of aspect ratio of nano-structured Ag embedded Al:ZnO composites are studied and discussed. With the aspect ratio boosts to several hundreds, the composites show unique optical properties and work as transparent and conductive electrodes. So, the trade-off problem is to compromising the electrical properties and optical transparency. Ag NWs with different length have been synthesized and the effect of Ag junctions in Al:ZnO are discussed by both computational calculation and experiments.

The final chapter is conclusion of all and future remarks.

# 2.0 Sintering, Crystallinity and Polaron Hopping in Microwave Irradiated $La_{1-x}Sr_xMnO_3$ Ceramics

## 2.1 Background & Methods

$La_{1-x}Sr_xMnO_3$ (LSM) perovskite oxides have been actively studied because of their unique properties. The properties, especially those in magnetic and electrical field, are usually attributed the transition metal cations $Mn^{3+}$/$Mn^{4+}$. They are widely used as cathodes and interconnect materials for solid state electrolysis cells and fuel cells (SOECs/SOFCs) due to their excellent electrical conductivity, good stability and compatibility with other components at high temperature (500°C-800°C).[42-43] The interactions on B sites of the perovskite also makes it a promising materials for the application like magnetic sensors, reading heads for magnetic memories as its excellent catalytic and magnetic properties.[44]

As it all known, synthesis and preparation method affect the properties of LSM via changing the microstructure, crystallinity and grain growth. Traditional preparation method, such as solid-state method,[45] sol-gel method,[46] Pechini method[47], co-precipitation method[7] and combustion method[48] have been investigated and discussed elsewhere. Although solid-state preparation technique is cheap and facile, the calcination period needed to get the single phase LSM is usually ~ 20hr, which results in coarse grains with a wide distribution. Conversely, wet chemical preparation method is more reliable to provide fine particles with narrow distribution.

The main effort of the present chapter is to examine the properties of LSM prepared by two wet chemical synthesis methods, microwave-assisted method and co-precipitation method under two different pH value, pH = 9 and pH = 11. Microwave irradiation was applied, since it can provide rapid and homogenous heating and thus, is often used to improve the crystallinity and prevent the formation of second phase. pH value has been changed to control the solubility. The temperature-dependent electrical conductivity was compared and discussed.

### 2.1.1 $La_{1-x}Sr_xMnO_3$ Composition and Defect Models

Undoped $LaMnO_3$ is an intrinsic p-type $ABO_3$ perovskite, shown in Figure 2.1. Its conductivity can be improved by replacing A-site ions with divalent ions, such as Sr and leaving holes on the B-site. The electroneutrality can be expressed as:

$$LaMnO_3 \xrightarrow{SrO} La_{1-x}^{3+}Sr_x^{2+}Mn_{1-x}^{3+}Mn_x^{4+}O_3 \tag{2-1}$$

Li *et al.* reported the effect of $Sr^{2+}$ on the electrical conductivity of $La_{1-x}Sr_xMnO_3$ (x = 0 ~ 0.9). The conductivity boosts from 40 to 485 S $cm^{-1}$ at $1000^oC$.[49] Because L $La_{1-x}Sr_xMnO_3$ contain Mn cations in the mixed $Mn^{3+}$-$Mn^{4+}$ valence state, thereby follow polaron hopping conduction mechanism. The electrical conductivity of $La_{1-x}Sr_xMnO_3$ is reported to be a function of doping level x and it obtained the maximum when x = 0.5 because the carrier concentration is in a relationship as c(1-c) for hopping mechanism, where c is the ratio of $Mn^{3+}/Mn^{4+}$. The crystal structure displays from high symmetric cubic structure into hexagonal-rhombohedral system. Due to the substitution of $La^{3+}$ (1.36A) with larger $Sr^{2+}$ (1.44A), a reduction in Mn-O length as well as an increment of Mn-O-Mn angle occur. Under different doping level, lattices derived into rhombohedral (x=0~0.5), tetragonal (x=0.5) and cubic (x=0.7), with distortion and relaxation of oxygen octahedra along [111]. [49,52]

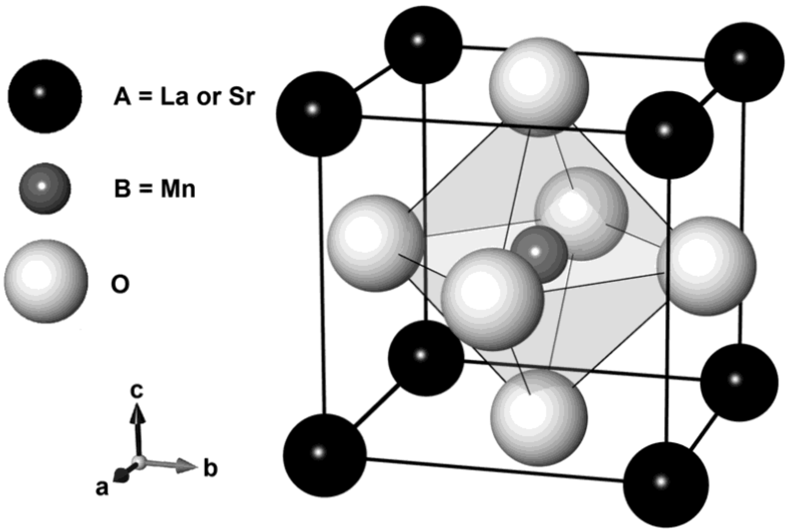

**Figure 2.1 Perovskite structure of Sr doped LaMnO3** [9]

### 2.1.2 Polaron Hopping Conduction Mechanism

Conduction mechanism for conventional semiconductors is well knows as band theory. However, in this study, electrical conductivity shows a strong temperature-dependence at high temperature and therefore doesn't obey the conventional electron conductive mechanism. Generally, in insulating semiconductors, such as perovskite and spinel oxides, a polaron is favorably formed when lattice is distorted and carriers are "self-trapped", shown in Figure 2.2. Polaron hopping theory instead of band theory works well to explain the conduction mechanism in these semiconductors. There are two classifications for polaron conduction mechanisms:[50] larger polaron hopping (Frohlich mechanism) and small polaron hopping (Holstein mechanism) depending on the size of the polaron to lattice constant. The size of large polaron is much larger than the unit cell of the lattice. The movement of this kind of polaron is always simultaneously associated with the lattice distortion and inertia. In this study, the polarization is comparable to the size of lattice constant. Therefore, we will focus on the discussion on small polaron hopping conduction mechanism.

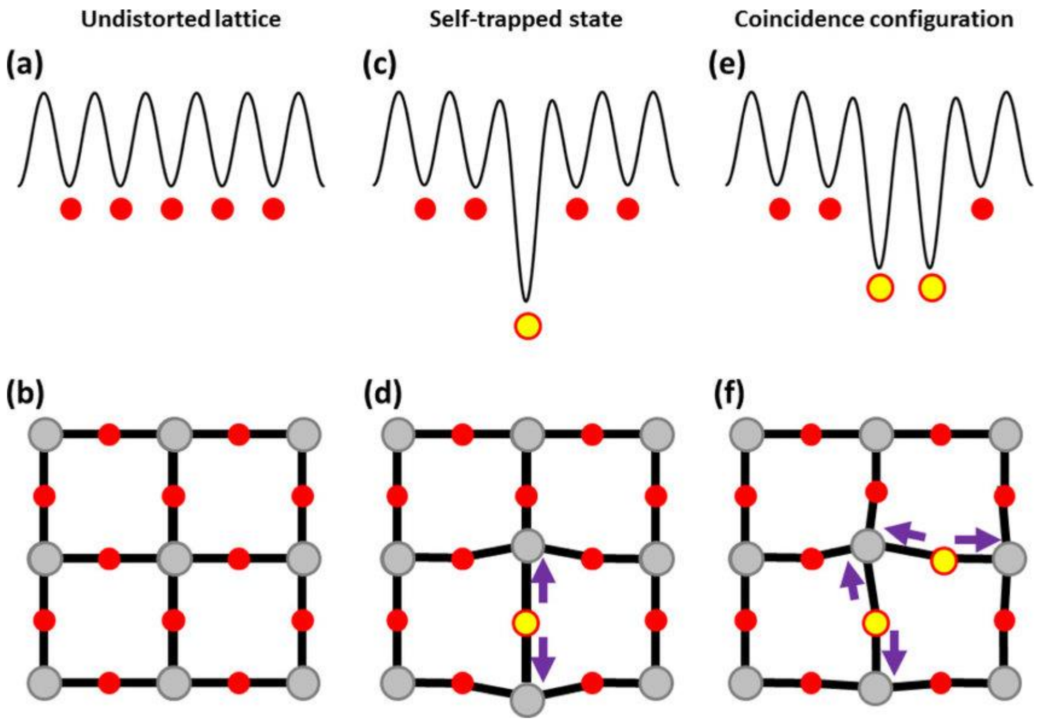

**Figure 2.2 Schematics showing the formation of small polarons and their hopping: (a),(b) undistorted lattice (holes are delocalized); (c),(d) self-trapped state (hole is trapped and polaron is formed) and (e),(f) coincidence configuration (polarons of a similar low energy are formed close and they can hop by exchanging their sites).** [51]

For small polaron, the electrical field produced by ionic dislocation and electron (or hole) is confined to the size of lattice or even smaller.  At high temperature, the conduction mechanism can be simplified as the carriers hopping from one site to the other, namely the hopping mechanism. The activation energy for hopping follows Arrhenius relations by two models, Adiabatic (Emin-Holstein) model and non-adiabatic (Holstein model).[50]

In adiabatic model, it assumes that the carriers are relaxed in the lattice distortion created by the electric field of the transition metal ions. The role of thermal fluctuation is low and the probability of the carrier hopping is very high. Therefore, the movement of carriers is much faster than that of the lattice distortion. The polaron mobility can be represented as:

$$\mu_{hop} = \frac{3}{2}\frac{ea^2 v_0}{k_B}\frac{1}{T}\exp\left(-\frac{W_p - 2J}{2k_B T}\right) \tag{2-2}$$

where a is the hopping distance;  is the effective frequency for hopping (optical phonon frequency); is the polaron binding energy; *J* is the polaron kinetic energy, due to the rapid carrier hopping back and forth between neighboring lattice sites before lattice distortion ends. The activation energy ($W_p$ - 2*J*) is directly related with the doping level of $Sr^{2+}$ in the perovskite LSM. As the $Sr^{2+}$ concentraion increases, ($W_p$ - 2*J*) decreases and polarons hop more easily.

In non-adiabatic model, the kinetic energy of polarons is small and electronic wavefunctions are overlapped less. Therefore, electron-polaron coupling is large and the probability of a charge carrier to hop after an energy coincidence occurs, is smaller than 1. The lattice is easily relaxed after the carrier hops to the new position.  The movement of carrier is lower than that of lattice distortion. The polaron mobility of the non-adiabatic process is expressed as:

$$\mu_{hop} = \frac{ea^2 v_0}{k_B}\frac{\pi J^2}{h}(\frac{2\pi}{W_p k_B})^{1/2}\frac{1}{T^{3/2}}\exp(-\frac{W_p}{2k_B T}) \tag{2-3}$$

Compared with the adiabatic model, the conductivity of non-adiabatic model is linearly proportional to $T^{3/2}$) instead of 1/T.

Usually, the change of conductivity with temperature is in between the adiabatic and non-adiabatic models. The value of J should be smaller than $W_P$ in the non-adiabatic model. If J gets close to $J_{max}$ at high temperature, even the small polaron hopping follows the adiabatic model.

### 2.1.3 Microwave-Assisted Reaction

Compared with traditional heat treatment, such as oil bath, sand bath and heating mantles, microwave-assisted reaction takes the advantage on its rapid reaction rate, which provides uniform and selective heating with lower energy consumption.[52] As shown in the Figure2.3, the temperature distribution between traditional heating and microwave heating is different. During traditional heating process, heat transferred from oil bath to the surface of the reaction container first, and then the hot surface further heats the solution. This process introduces some problems like local overheating or uneven heating, which may lead to decomposition or reaction of partial solution. However, during the microwave heating process, microwave irradiation directly reacts with the dipoles or ions existing in the solution. Also, it could pass through the reaction container into the solution in very short time that the heating process works efficiently with very rapid ramping rate. [51-52] Therefore, the products with higher purity and minor second phases are expected. In addition, microwave irradiation also allows for faster lattice diffusion and magnetic ordering properties which is promising to obtain the products with better crystallinity.

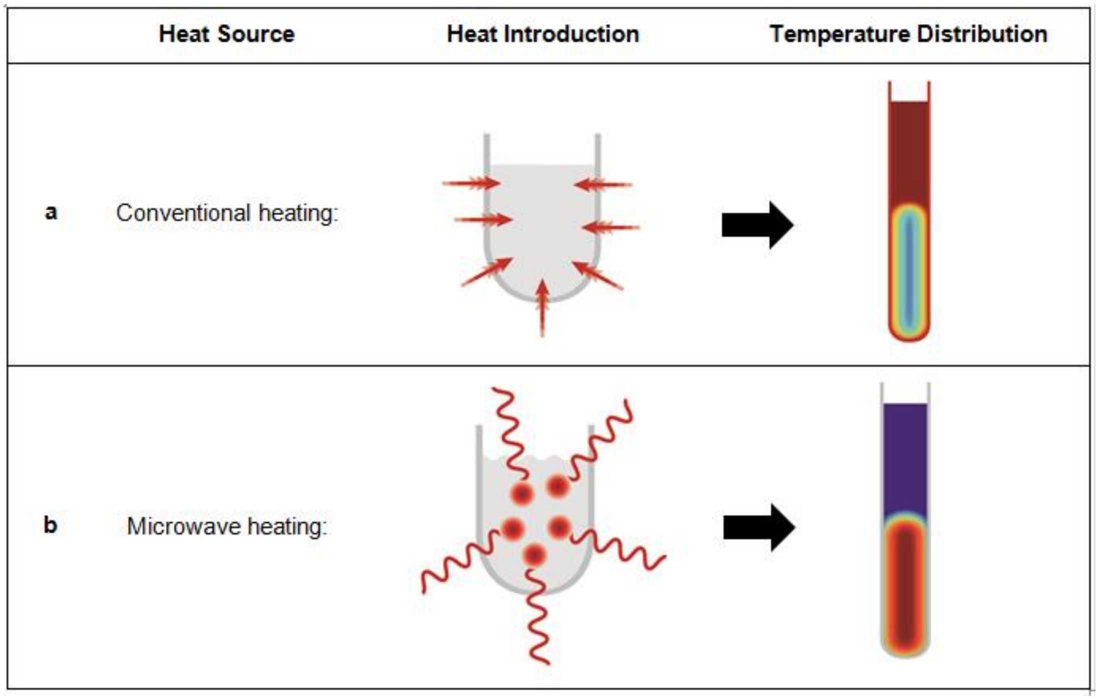

**Figure 2.3 Temperature distribution comparison between traditional heating and microwave heating** 13

### 2.1.4 Solid-State Sintering and Grain Growth

Sintering processes has been investigated and practiced for thousands of years, involving many variants, such as solid-state sintering, liquid-phase sintering, and pressure-assisted sintering. It is of tremendous relevance and importance to influence the resultant microstructure, density, mechanical strength and other physical and chemical properties. The microstructural evolution during a solid-state sintering process has been the focus of our efforts to understand the possible mechanisms to better predict the microstructure of products.

Thereby, the understanding on solid sintering process would be critical for our study. Sintering occurs when the powders are well packed into ‘green body’ and heat at the sintering temperature. Notably, the driving force for densification during sintering process is always to reduce the interfacial free energy via material transport mechanisms. Figure 2.4 (a) illustrates the three cases of mass transport allowing the control of microstructural evolution: surface diffusion, volume diffusion, vapor diffusion. They usually occur in different temperature range and can be distinguished by the activation energy Q. Surface diffusion is effective on surface smoothing, pores rounding and particle necking but no densification due to the limit volume shrinkage. Volume diffusion and grain boundary diffusion contributes more on the densification. During the intermediate and final stages of sintering, diffusion of atoms across the grain boundaries and causes the replacement of grain boundaries. Heating leads to the growth of some grains at the expense of the shrinkage of others. The overall grain size becomes larger with a reduction of total free energy.

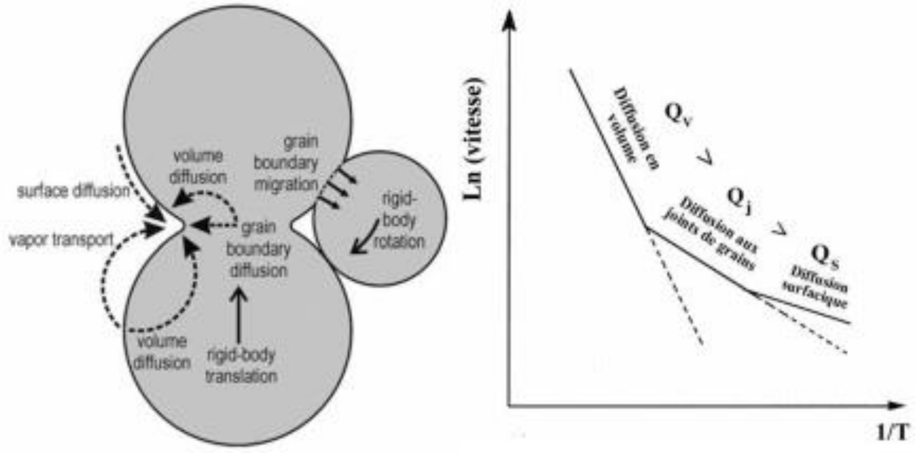

**Figure 2.4 Sintering mechanism at different stages: surface diffusion, grain boundary diffusion and volume diffusion**[55]

The densification is usually accompanied by the grain growth. Generally, grain growth refers to normal grain growth and abnormal grain growth. The distinct between normal and abnormal sintering is mainly according to the distribution of grains and its temperature-dependency. A linear relation of average grain size and time is expected for normal grain growth, when the grains are homogenous in size. When the grain size distribution is wide, fine grains have much higher activation energy than the coarse grains. Resultantly, the grain size distribution becomes bimodal until the grains are competitive in size and return to normal grain growth.

Annealing temperature and time are two controllable parameters to obtain fully dense compacts. The characteristics of grain growth are best demonstrated by the Arrhenius equation. Say, to determine the grain growth kinetics, the average grain size and annealing temperature and time follows[55]:

$$D_t^n - D_0^n = k \exp(-\frac{Q}{RT})t \tag{2-4}$$

where n is the grain-growth exponent, T is the sintering temperature, t is the sintering time, $D_t$ is the average grain size at time t and temperature T, $D_0$ is the average initial grain size, Q is the activation energy, and k is a grain-growth constant. Ideally, for normal grain growth, the grain-growth exponent n is 2 when diffusion is dominant. However, grain growth is sensitive to grain size distribution, precipitations, pores or liquid phase formation. Non-uniform coarsening, or say abnormal grain growth would take place. If these mechanisms work together to drive the grain growth, the grain-growth exponent n may be increased to 2 ~ 5. In sum, when the grain growth exponent n is approximately constant in a temperature range, according to the equation, it’s possible to calculate the activation energy Q, by experimental measuring the average grain size and temperature and plotting in log(D) vs. 1/T. It should be remembered that the activation energy in different temperature ranges is instructive to compare, followed different diffusion mechanisms, like surface diffusion, grain boundary diffusion and self-diffusion, shown in Figure 2.4 (b).

## 2.2 Enhancement of Grain Growth and Electrical Conductivity of La0.8Sr0.2MnO3 Ceramics by Microwave Irradiation

Highly crystalline $La_{0.8}Sr_{0.2}MnO_3$ (LSM) perovskite with larger grain and high electrical conductivity was synthesized by microwave-assisted procedures, under pH = 11. The reaction different to co-precipitation was investigated by the crystallization evolution analyzed by X-ray diffraction (XRD) confirming the formation of the perovskite and second phases. Microwave radiation directly agitates electric dipoles of precursors, providing rapid and uniform heating. Its product was expected of high crystalline nanoparticles with a narrow size distribution and less second phases. Moreover, microwave radiation and pH value influence the electrical conductivity. Thus, suppressing the formation of the second phase and rapid grain growth are of importance in the optimal synthesis of LSM.

### 2.2.1 Sample Preparation

$La(NO_3)_3{\cdot}6H_2O$ (99.99 %, Sigma Aldrich), $Sr(NO_3)_2$ (≥ 90.0 %, Sigma Aldrich) and $Mn(CH_3CO_2)_2$ (≥ 99 %, Acros) were used without further purification. First, the precursor solution was prepared by dissolving the chemicals with an atomic ratio of La, Sr and Mn = 0.8:0.2:1 in deionized water completely. Then methylamine solution was added to the precursor. Ammonia was added to adjust the pH dropwise until the pH reaches pH=9 and 11with a color change to light brown. The solution was collected and centrifuged at a speed of 5000rpm. In a typical co-precipitation synthesis, the precipitated particles were washed several times and dried at 95 $_{o}$C for 6hr. To microwave-assisted synthesis, the resultant mixture was transferred to 100 mL Teflon autoclave, and further sealed and placed in a microwave instrument at 150C (maximum power:

1.5GHz). The final products were marked as Co09, Co11, MW09 and MW11 following the synthesis method and pH value applied, respectively. The first two letters denote the synthesis method (Co : as co-precipitated state and MW: microwave-irradiated state) and last two letters denote the final pH of the reaction solution. The products were calcinated at 1000 $_{o}$C and then grounded for 24 h via ball milling. Finally, the fine powders were pressed into pellets under a constant pressure of 8000 psi and sintered 1400 $_{o}$C in air for final densification.

### 2.2.2 Characterization and Measurement

X-ray diffraction (XRD) pattern of the synthesized powder heat-treated under different temperature was recorded using PANalytical Empyrean Diffractometer with Co-Kα ($\lambda = 0.187$ nm) as radiation source. The XRD pattern was collected in the 2θ ranged in 10 - 80° with a step size .042 $_{o}$ and a scan speed 5.5 $_{o}$/min. ICSD collection codes were used for phase indexing.

The microstructure of pellets were characterized using scanning electron microscopy (SEM, FEI Apreo). High temperature Ag paste was screen-printed and fired at 900 $_{o}$C as electrodes. The electrical conductivity was measured in the temperature range from 25 $_{o}$C to 800 $_{o}$C in air using Keithley Digital Multimeter.

### 2.2.3 Results and Discussions

Figure 2.5 shows SEM images of nanoparticles synthesized through different paths. Insets provides a size distribution of nanoparticles. The average size of nanoparticles ranges from 40 nm for Co09 to 80 nm for MW11. In both co-precipitated and microwave-irradiated cases, an increase in pH from 9 to 11 promotes the growth of nanoparticles. A increment on pH value allows for the changes in solubility, surface energy and isoelectric point of nanoparticles in aqueous solutions. Jolivet *et al.*, developed the semi-empirical model on the size of precipitated oxide nanoparticles in the aqueous system using the electrostatic surface charge density, the interfacial tension and the surface energy.[56] A decrease on the surface energy, along with the nucleation rate of the nanoparticles and an increment on the solubility of the nanoparticles were obtained with pH value change. In ZnO, $Cr_2O_3$ and anatase $TiO_2$, larger nanoparticles are found in the aqueous solution of higher pH.[57] In contrast, an increase in pH decreases the size of and $Fe_3O_4$ and Copper nanoparticles.[58] Since the surface energy of co-precipitated nanoparticles in LSM is yet to be known, the nanoparticle size cannot be quantitatively predicted. However, results in Figure 1 suggest that the increase in pH increases the surface energy of LSM nanoparticles, suppresses the nucleation and destabilizes smaller nanoparticles.

In addition to pH effect, the growth of nanoparticles by the microwave irradiation is attributed to Oswald ripening of the precipitated nanoparticles.[18] When the aqueous solution in a sealed vessel is irradiated by the microwave, temperature and pressure inside the vessel increase and solid nanoparticles dissolve more dynamically. This is a driving force of the Oswald ripening. During the microwave irradiation, nanoparticles smaller than the critical nucleus radius are dissolved preferentially while larger nanoparticles continue growing to reduce the total surface energy. Oswald ripening by the microwave irradiation have been reported in oxide ($TiO_2$, NiO), metal (Pt, Pt/Ru) and non-oxide (CdSe, CoS) systems, which is consistent with this study. The combined effect of pH and microwave irradiation on the solubility of LSM precursor nanoparticles is responsible for the largest nanoparticle size of MW11.

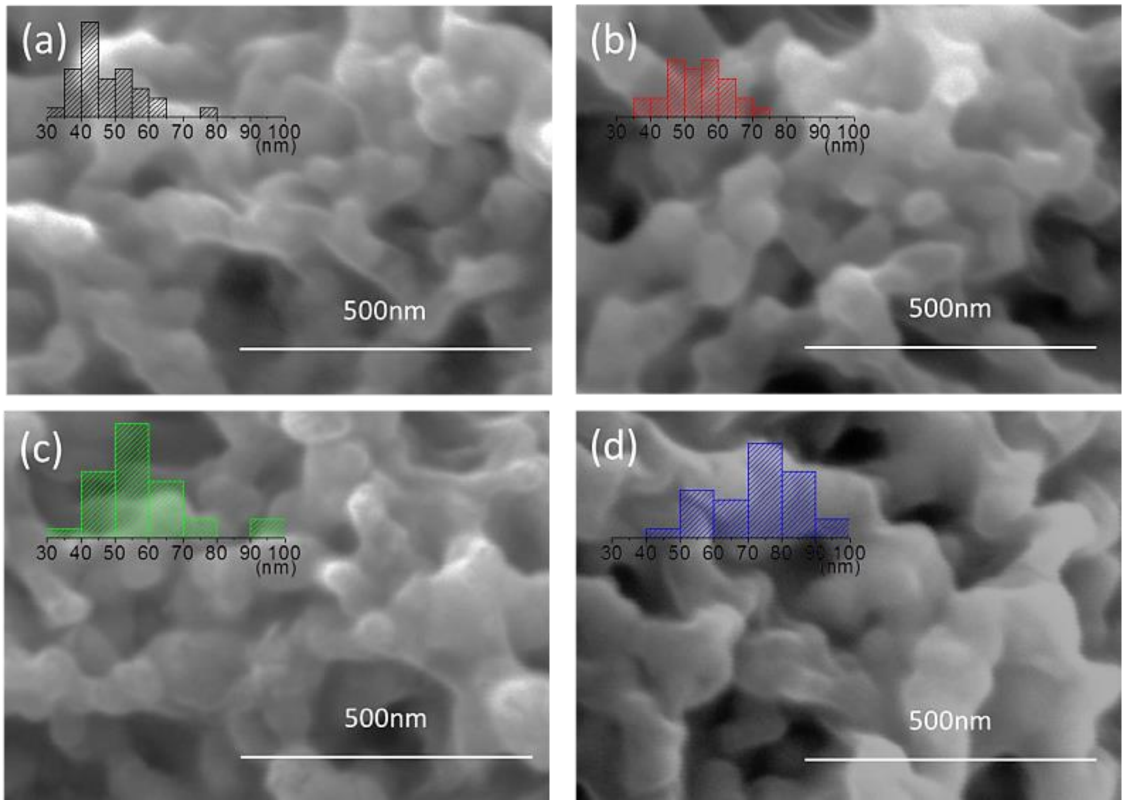

**Figure 2.5 SEM images of nanoparticles after synthesis (before any heat treatment): (a) Co09, (b) MW09, (c) Co11 and (d) MW11**

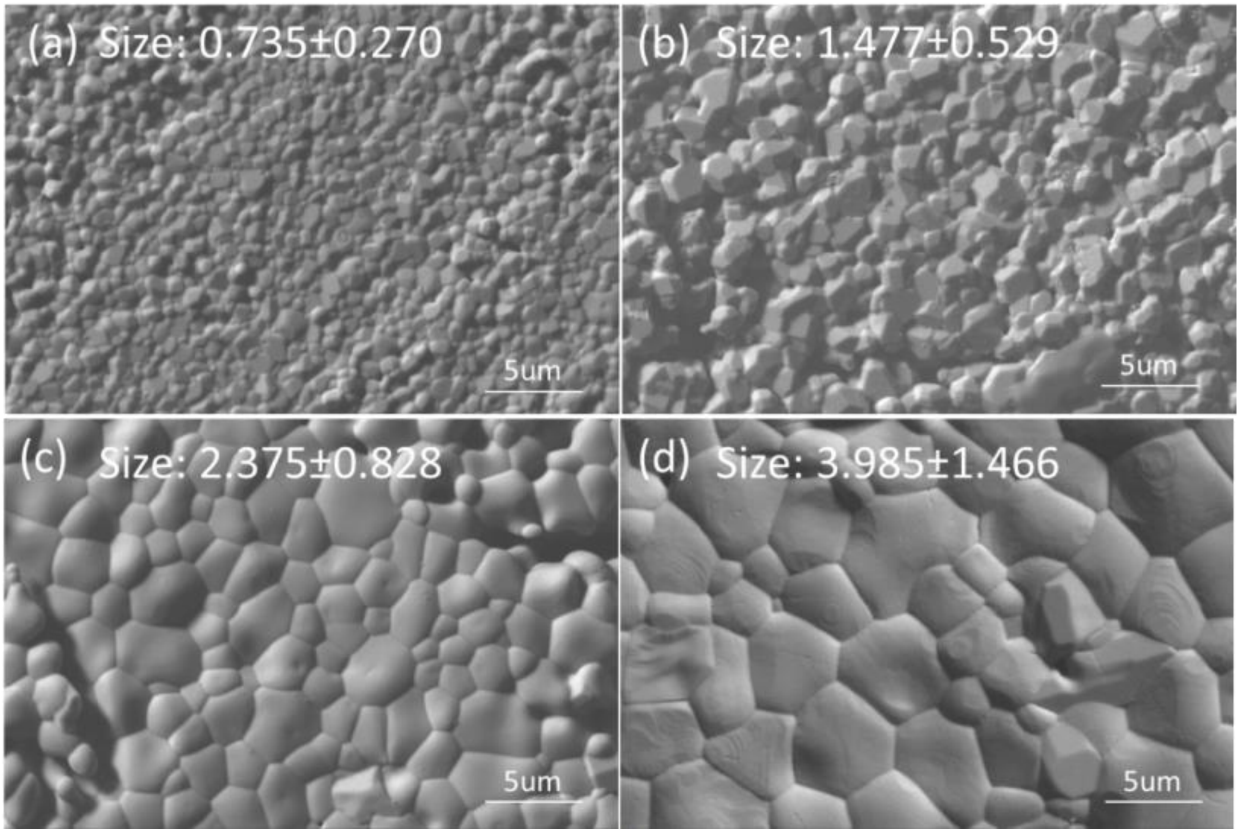

**Figure 2.6 Microstructures of LSM pellets after sintering: (a) Co09, (b) MW 09, (c) Co11 and (d) MW11.**

Figure2.6 presents the morphologies of LSM pellets after sintering at 1400 $_o$C. A more rapid grain growth is observed for MW11. To indicate the growth mechanism difference, a change in an average grain size (*D*) of Co11 and MW11 were investigated as a function of annealing temperature. Figure2.7 ln *D* versus 1/*T* was plotted. The grain growth for single phased materials is empirically expressed as follow:[55]

$$D_t^n - D_0^n = k \exp(-\frac{Q}{RT})t \tag{2-5}$$

where *n* is the grain-growth exponent, *T* is the sintering temperature, *t* is the sintering time, $D_t$ is the grain size at time *t* and temperature *T*, $D_0$ is the initial grain size, *Q* is the activation energy, and *k* is a grain-growth constant. Since $D_0$ (in nanometer-scale) is much smaller than $D_t$ (in micrometer-scale), $D_0$ can be neglected in equation (1). Also, the grain size after annealing for a constant time t can be further expressed:

$$\log D = \log k - \frac{Q}{n}\frac{1}{RT} \tag{2-6}$$

In Figure 2.7, a slope of Q which is known to the activation energy for grain growth always associated with the lattice self-diffusion and grain boundary diffusion based on the mechanisms that involved. A more significant change in grain size for MW11 sample was observed, reaching value around 3.985 μm. This observation indicates that structural and compositional difference might be found for Co11 and MW11. Second phase or precipitation might retard the normal grain growth temperature range for Co11.

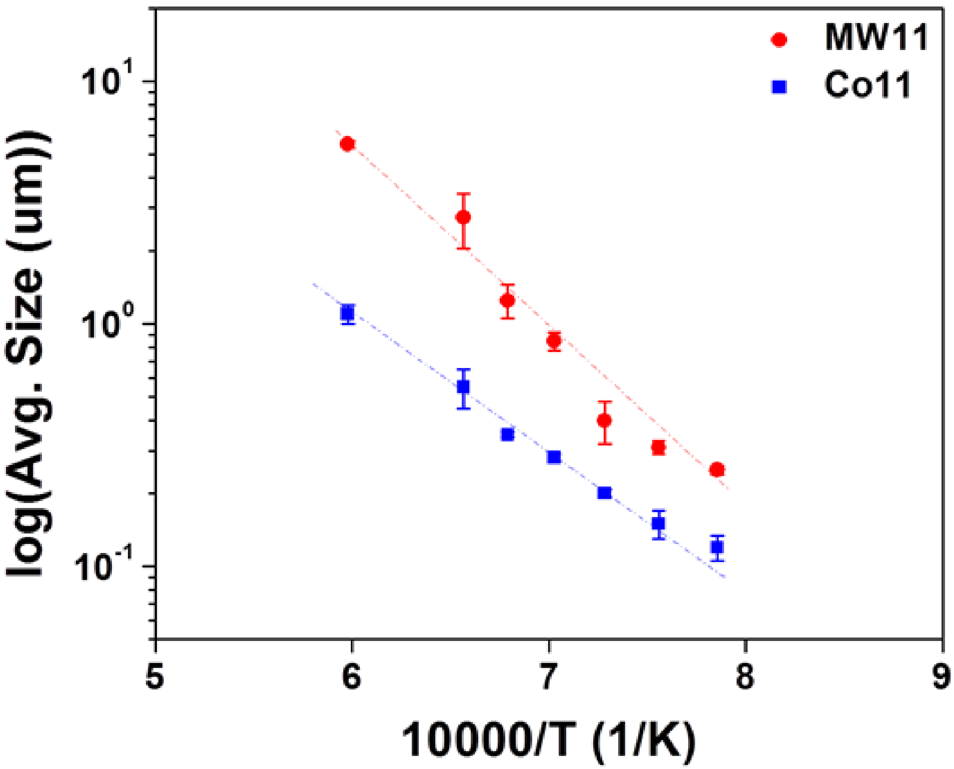

**Figure 2.7 (log (Average grain size in μm)) vs. (10000/T) of Co11 and MW11 ceramics: a change in the average grain size as a function of temperature**

Figure 2.8 shows the crystallographic evolution patterns of the isothermally annealed samples, Co11 and MW11 at 150 oC, 400 oC, 500 oC, 700 oC, 1000 oC and 1300 oC. The phases indexed from each pattern have been summarized in Table2.1. At high temperature 1300 oC, single phased LSM are obtained for both Co11 and MW11, which indicates that normal grain growth are expected in this temperature range. However, the phase evolution paths are different. At intermediate temperature (700-1000 oC) annealing, notably, the amount of second phases, such as $La_2O_3$ and $La(OH)_3$ is much larger in Co11, compared to the amount in MW11. These precipitations may hinder the growth of LSM due to the association with normal and abnormal grain growth. For a normal grain growth, the grain growth exponent (n) of single phase is 2. When the formation of second phases takes place, the migration of grain boundaries is inhibited with an increment of grain growth exponent (n). The abnormal grain growth would not cease until the single phased LSM has been obtained. Regardless the residual second phase in MW11 above 1000$_{o}$C, the grain growth is already close to normal grain growth. In addition, the crystallization starts at low temperature (400-550 $_{o}$C). An intermediate phase, $La_2Mn_2O_7$ is found in only MW11samples. Given that the integrated intensity of the perovskite phase is almost same for Co11 and MW11, the appearance of $La_2Mn_2O_7$ indicates that more Mn reacts with lanthanum ions. Subsequently, the intermediate phase is more easily to turn into perovskite, leaving less residual La to form the second phases. According to the phase evolution analysis, it’s concluded that the difference in grain growth between Co11 and MW11 is attributed to the compositional difference below 1000$_{o}$C.

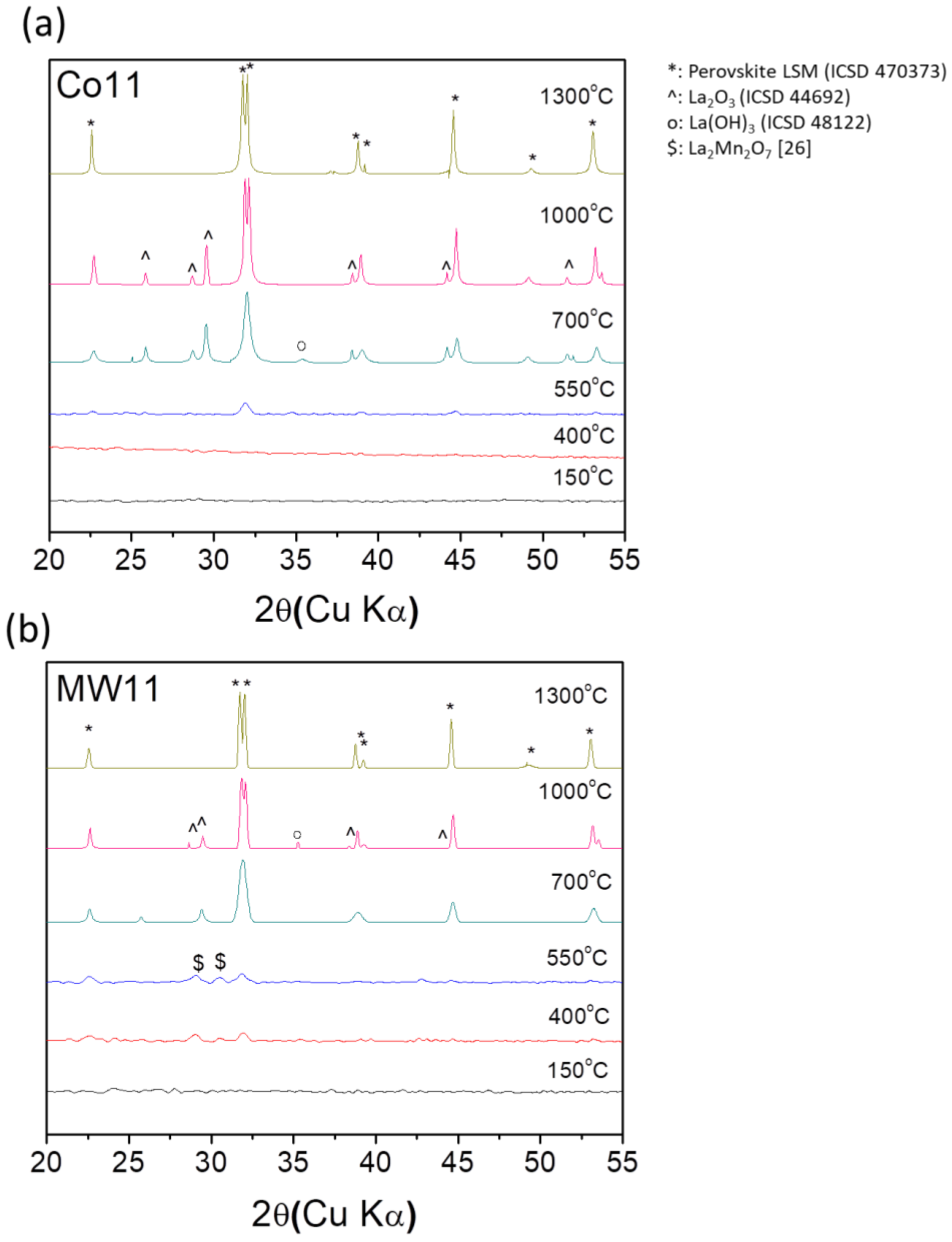

**Figure 2.8 XRD patterns of (a) Co11 and (b) MW11 which are calcined at different temperature**

**Table 2.1 Phase evolution paths of nanoparticles (Co11 and MW11) as a function of temperature in air**

| **Temperature** | **Co11** | **MW11** |
|---|---|---|
| 1300 $_{o}$C | Perovskite LSM | Perovskite LSM |
| 700 $_{o}$C - 1000 $_{o}$C | Perovskite LSM + $La_2O_3$ (more) + $La(OH)_3$ | Perovskite LSM + $La_2O_3$ (less) + $La(OH)_3$ |
| 550 $_{o}$C | Perovskite LSM | Perovskite LSM + **$La_2Mn_2O_7$** |
| 400 $_{o}$C | Amorphous | Perovskite LSM + **$La_2Mn_2O_7$** |
| As-synthesized | Amorphous | Amorphous |

The samples were subjected to temperature-dependent electrical conductivity. In Figure 2.9, ln(σT) versus 1/T has been plotted. At high temperature, the conduction mechanism is dominant by small polaron hopping mechanism.[60] Holes are always relaxed in a potential well caused by the lattice distortion. As electric field is applied, polarons hop to the neighboring potential wells. The probability of hopping P equals to 1. And this is called adiabatic hopping following the well-established Emin-Holstein model: [61]

$$\sigma_{hopping} = \frac{3}{2}\frac{ne^2a^2v_0}{k_B}\frac{1}{T}\exp\left(-\frac{W_H}{2k_BT}\right) \qquad (2\text{-}7)$$

where $n$ is polaron density, $a$ is the polaron hopping distance, $v_0$ is frequency of optical phonons, $W_H$ is the activation energy for holes to move to adjacent sites. $v_0$ and $a$ of LM bulk is $1.66\times10_{13}$ Hz and 0.39 nm, respectively.[62-63] When the hole concentration is a constant (proportional to $Sr_{2+}$

doping level), the polaron density (*n*) is supposed to be fixed and  is a constant in this study. Then, equation (3) may be further simplified as:

$$\ln(\sigma_{hopping}T) = \ln A - \frac{W_H}{2k_B}\frac{1}{T} \tag{2-8}$$

Figure 2.9 presents a linear relation ln(σT) versus 1/T. According to equation (4), the conduction of all the samples fits the adiabatic model well.  The activation energy of Co09, MW09, Co11 and MW11 is calculated as 0.35, 0.33, 0.27 and 0.24 eV. As reported previously, the activation energy of the small polaron hopping was also slightly larger than 0.2 eV.[64-65] The larger the LSM grains are, the smaller the activation energy of small polaron hopping will be. Give that structural and compositional defects at the grain boundary, such as oxygen vacancies, polarons tend to be trapped, which slows down transport of carriers. It has concluded that an increase in the grain size is expected to reduce the grain boundary area and effectively decline the energy needed for polaron hopping.[66-69]

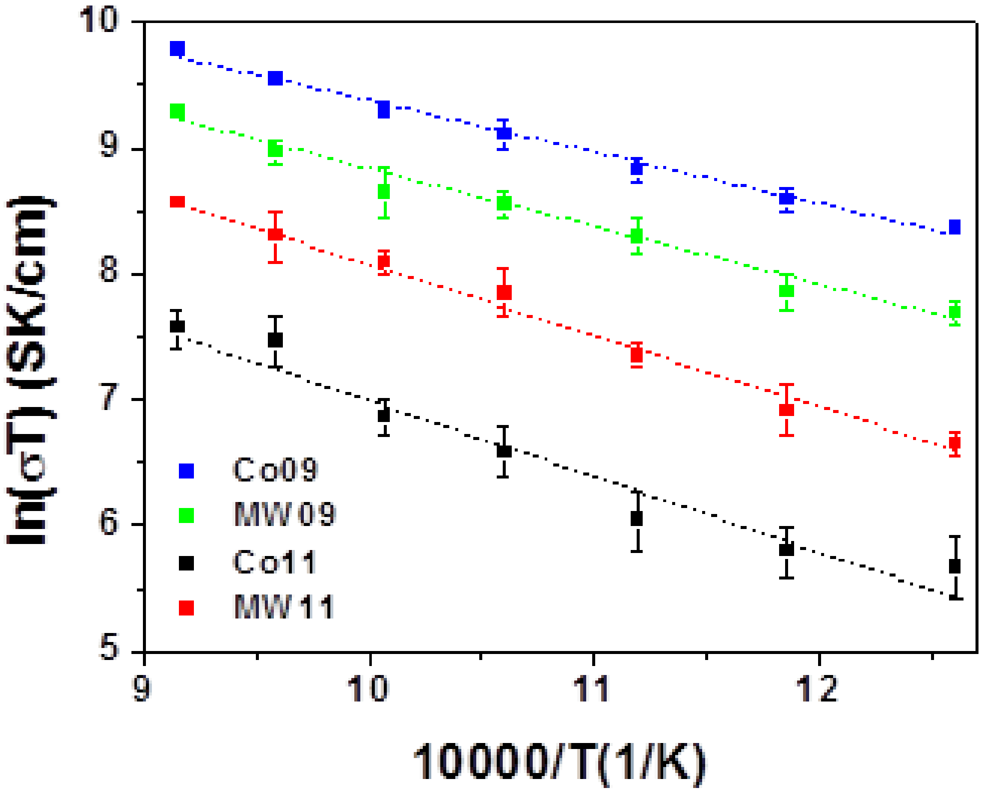

**Figure 2.9 Temperature dependence of electric conductivity of different LSM ceramics which were sintered at 1400 ₒC in air.**

Moreover, to examine the potential to be applied as interconnect or symmetric electrode, the chemical stability at high temperature is an indispensable requirement. With direct contact with YSZ/Ni, the commonly used anode materials in SOFCs/SOECs, the resistive phases such as $LaZr_2O_7$ and $SrZrO_3$ are favorably formed in oxygen-deficient environment.[28] The chemical stability of our LSM products with YSZ and NiO was tested via thermally annealing the mixture of LSM, YSZ and NiO powders in air or reducing (95% $N_2$ + 5% $H_2$) ambiance at 900 ₒC and 1100 ₒC. Minor second phases have been found from the XRD patterns in Figure 2.10 (a) for both MW11 and Co11 even the temperature tops as 1100 $_{o}$C, which is higher than operation temperature, in the air ambiance. When placed in the reducing ambiance, Co11 exhibits worse chemical stability than MW11. More second phases, such as $SrZrO_3$ and $MnO_x$ were found in Co11/YSZ/NiO mixture at 1100 $_{o}$C. Since the second phases may precipitate first at grain boundaries, where more oxygen vacancies are preferentially formed. MW11 with less grain boundary area, has better chemical stability with other components, YSZ and NiO in reducing ambiance. This result indicates that the microwave-assisted LSM may be the good candidate as the interconnect and symmetric electrode for high temperature applications, SOFCs and SOECs with exposure to oxidizing or to reducing ambiance.

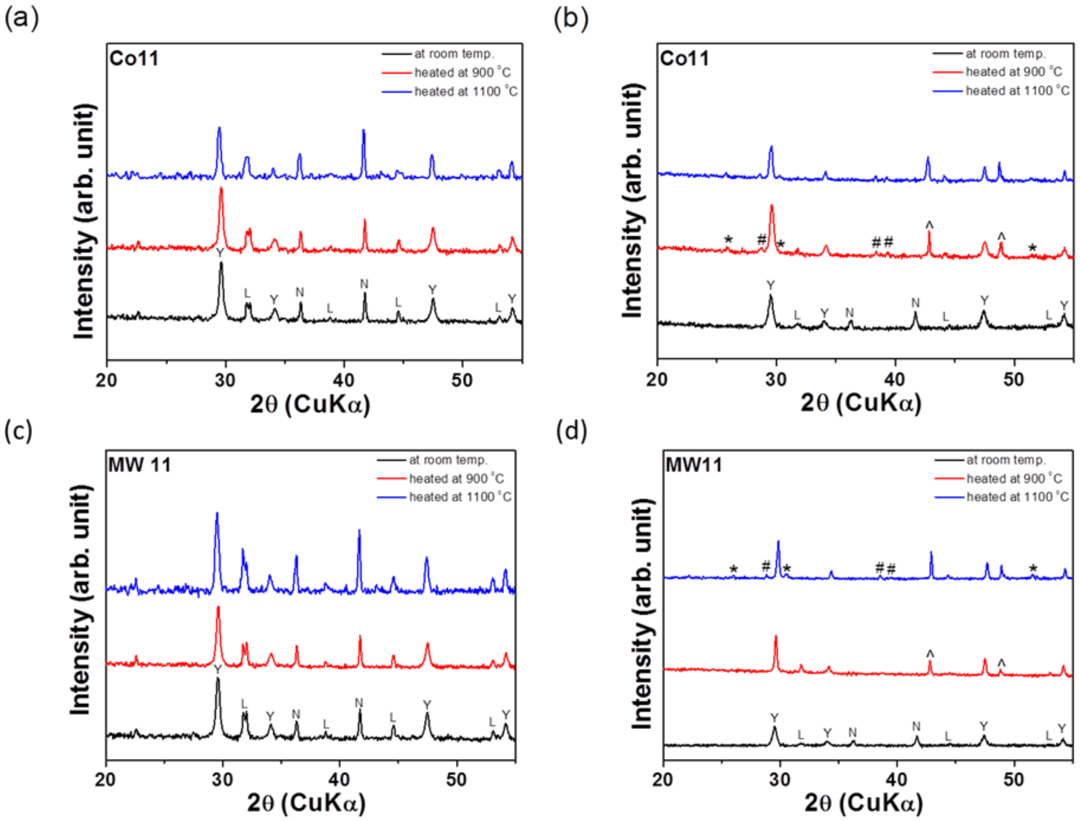

**Figure 2.10 XRD patterns of LSM/YSZ/NiO mixture after heat-treatment at 900 oC and 1100 oC under (a) air and (b) reducing ambience (Letters used in XRD data represent L: LSM, Y: YSZ, N: NiO, *: La2Zr2O7, #: MnO and ^: Ni).**

# 3.0 Sintering and Electric Conductivity of LSM:Ni Composite Using Different Size of Ni Particles

## 3.1 Background & Motivation

### 3.1.1 Motivation

Perovskite oxides in the formula of $ABO_3$ have been widely investigated because they exhibit a wide variety of chemical and physical properties. $La_{0.8}Sr_{0.2}MnO_3$ (LSM) are the current state-of-the-art p-type conductors at high temperature. The aliovalent substitution at A site influences the valence state of transition metal cation Mn at B site and produces a mixture of $Mn^{3+}/Mn^{4+}$ on $BO_6$ octahedra.

One of the most critical issue for the p-type oxides to date is their strong dependency on oxygen partial pressure, which usually results in the weakened electrical conductivity when oxygen vacancies are formed. [70,71]

Given the high ohmic loss of LSM in oxygen-deficient environment, a simple method to produce conductive composites is the additions of conductive fillers which holds good conductivity in reducing ambiance. Nano to micro scaled Ni addition provides not only the conductive phase in the ceramic matrix, it also possibly meets the percolation threshold at low loading. Theoretically, the loading of metallic nanoparticles exceeds 30%, the so-call ‘percolation threshold’, a dramatic increment of electrical conductivity can be observed. Compared to Ni film, which has larger thermal expansion coefficient (TEC), around $13.3 \times 10^{-6} K^{-1}$ [72,73] , nano to micro scaled Ni addition might be the good candidates to maintain high electrical conductivity in reducing ambiance. Nevertheless, it has been reported that Ni (1um) may serve as sintering inhibitor of LSM during sintering, which increases sintering temperature of ceramics and hinders the grain growth.[74] The size of Ni is taken into consideration carefully to be beneficial to the sintering as well. Fine Ni particles are supposed to introduce more surface area and enhance reaction activity.[75-76] Ni incorporate might affect the molar balance between A-sites and B-site in the pervoskite structure and eventually changes the sintering behaviors. Furthermore, the formation of second phases, with lower melting temperature, might effectuate liquid phase sintering, which can be benign to final densification to a great extent.

Detailed studied of the impact of Ni size on the electrical resistivity and sintering behavior are presented in this chapter. In particular, we report the temperature dependent electrical conductivity in oxidizing and reducing atmosphere. An illustration of LSM and NiO/Ni grains in the composite has been shown in Figure 3.1. p-type LSM matrix dominate the conductivity in oxidizing ambiance, meanwhile, Ni becomes the major conductive phase in reducing ambiance. Based on these conduction paths, overall good conductivity is promising to be achieved with less ambiance dependency.

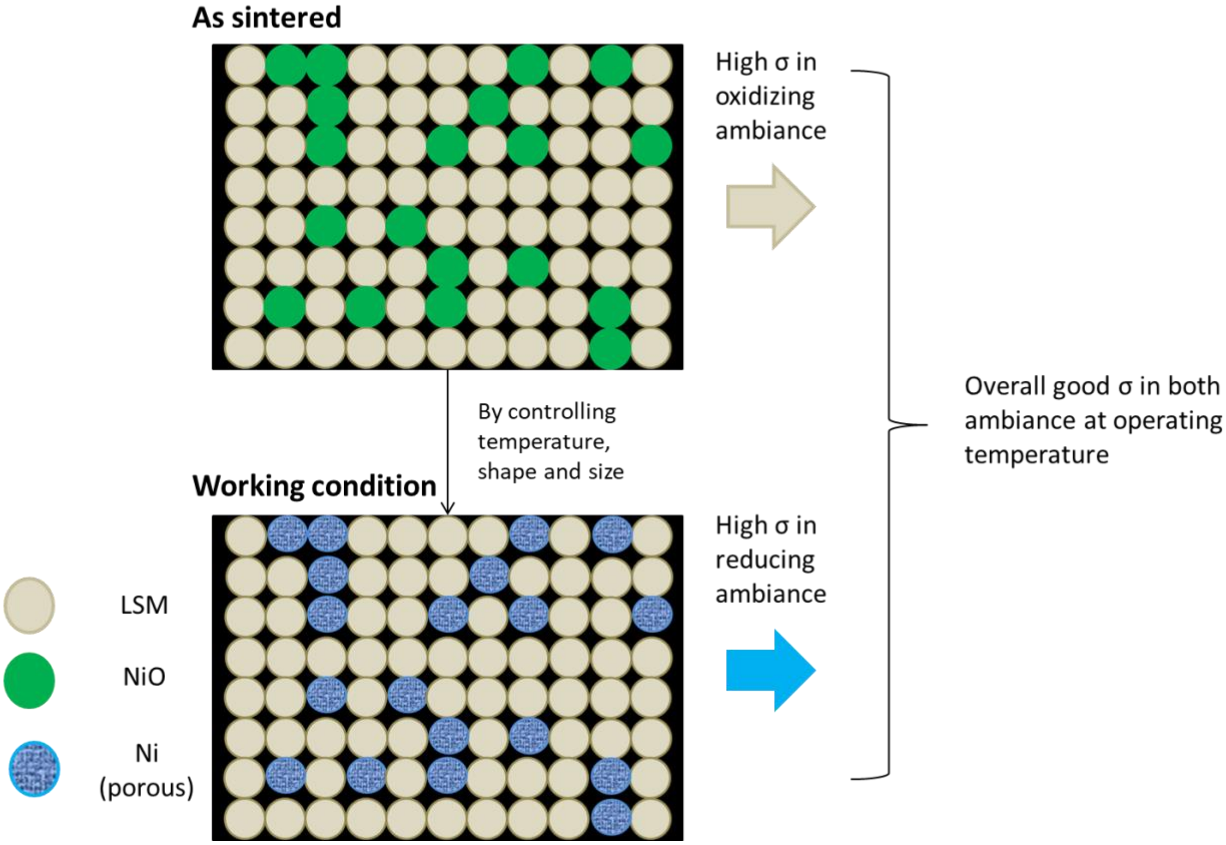

**Figure 3.1 Illustration of LSM:Ni composite as good electrode in both reducing and oxidizing ambiance**

### 3.1.2 Oxygen Deficient and Excess

The electrical conductivity of LSM is significantly affected by oxygen partial pressure. In the oxygen-deficient condition, oxygen vacancies are formed and serve as the predominant defects in the structure. The electronuetrality can then be expressed:

$$\frac{1}{2}O_2 + V_O^{\cdot\cdot} + 2Mn_{Mn}^{x} \Leftrightarrow 2Mn_{Mn}^{\cdot} + O_o^{x} \tag{3-1}$$

$$\frac{1}{2}O_2 + V_O^{\cdot\cdot} + 2Mn_{Mn}^{\prime} \Leftrightarrow 2Mn_{Mn}^{x} + O_o^{x} \tag{3-2}$$

The ratio of $Mn^{4+}/Mn^{3+}$ decreases when LSM is exposed into low oxygen partial pressure, which directly inhibits the electrical conductivity as well. Also, the reduction of Mn on the B-site results in the further expansion of lattice volume, due to the larger size of $Mn^{2+}$, which decrease the conductivity. Luo and el.[78], plotted the conductivity of LSM in both air and reducing environment, shown in Figure 3.2. The conductivity has dropped in a magnitude of two order when LSM is placed in oxygen-deficient ambiance.

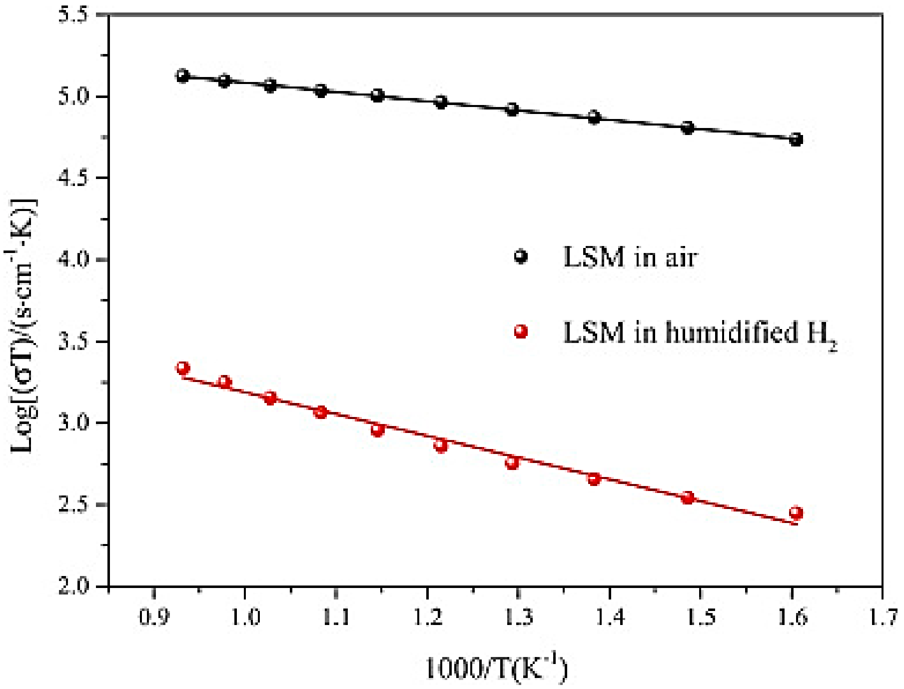

**Figure 3.2 Conductivity of LSM in Oxygen-excess and Oxygen-deficient regions.** 78

During sintering or operation in air ambiance, LSM is oxygen-excess. The excess $O^{2-}$ theoretically can be compensated by the interstitial ions or by the cation vacancies. In close-packed pervoskite structure, it is not easy to form oxygen interstitials. This is also confirmed by high-resolution transmission electron microscopy (HRTEM) 79-81. Then, the oxygen-excess can be only explained by the Schottky-type disorder. Both La and Mn vacancies are formed with more preferences to La vacancies. And the ratio of La/Mn vacancies maintains as a constant, which is closely related to the preparation process. 82-84 The neutralize equation can be expressed:

$$6Mn_{Mn}{}^{x} + \frac{3}{2}O_2 \Leftrightarrow 6Mn_{Mn}{}^{\circ} + 3O_O{}^{x} + V_{La}{}''' + V_{Mn}{}''' \tag{3-3}$$

Mizusaki et al.[80,85] further explained that electrical conductivity would not change by oxygen non-stoichiometry by a vacancy exclusion model. Say, each metal vacancy is surrounded by a thick shell excluding space to maintain the distance between vacancies. If this space is expanded into the whole area, no extra vacancy can be formed and the upper limit of oxygen excess is accessed. In fact, the change of electrical properties by oxygen excess is minor. $Sr^{2+}$ doping level takes the major responsibility.

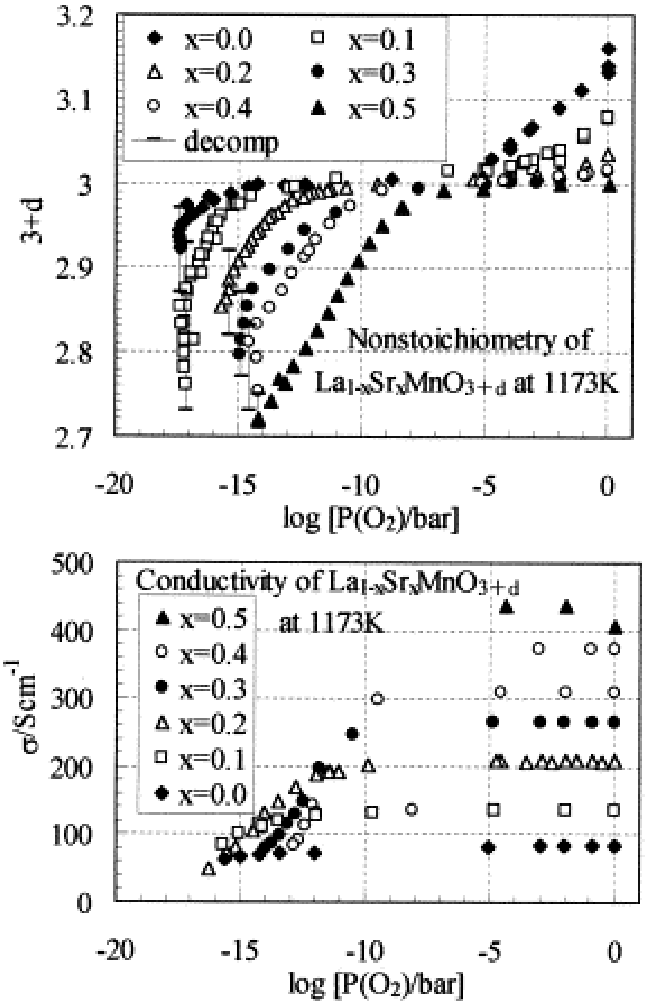

**Figure 3.3 Upper limit of oxygen excess and conductivity with different oxygen partial pressure**[86]

### 3.1.3 Binary Powder Packing Density

To accomplish the goal of achieving a high green body density, binary powders size distribution plays an important role in improving the packing density. So that fine particles fill the interstitial voids among coarsen particles. Figure 3.4 provides the packing density of binary powder mixture and demonstrates the importance of particle size distribution and mixing homogeneity to mixture packing density. The packing density of mixing powder is usually larger than either $f_s$ (packing density for only fine particles) or $f_L$ (packing density for only coarsen particles). And it reaches its maximum $f_*$ when certain composition of mixture is given.

However, even though the prediction of packing density for binary powder mixture is reliable by calculation, it is noticeable, the complex of sintering process increases the uncertainty of prediction on the sintered density. Despite the mixing of coarsen powders with fine powders increase the packing density, it may also inhibit densification or give little influence on the sintering at the end due to corresponding increased sintering stress.

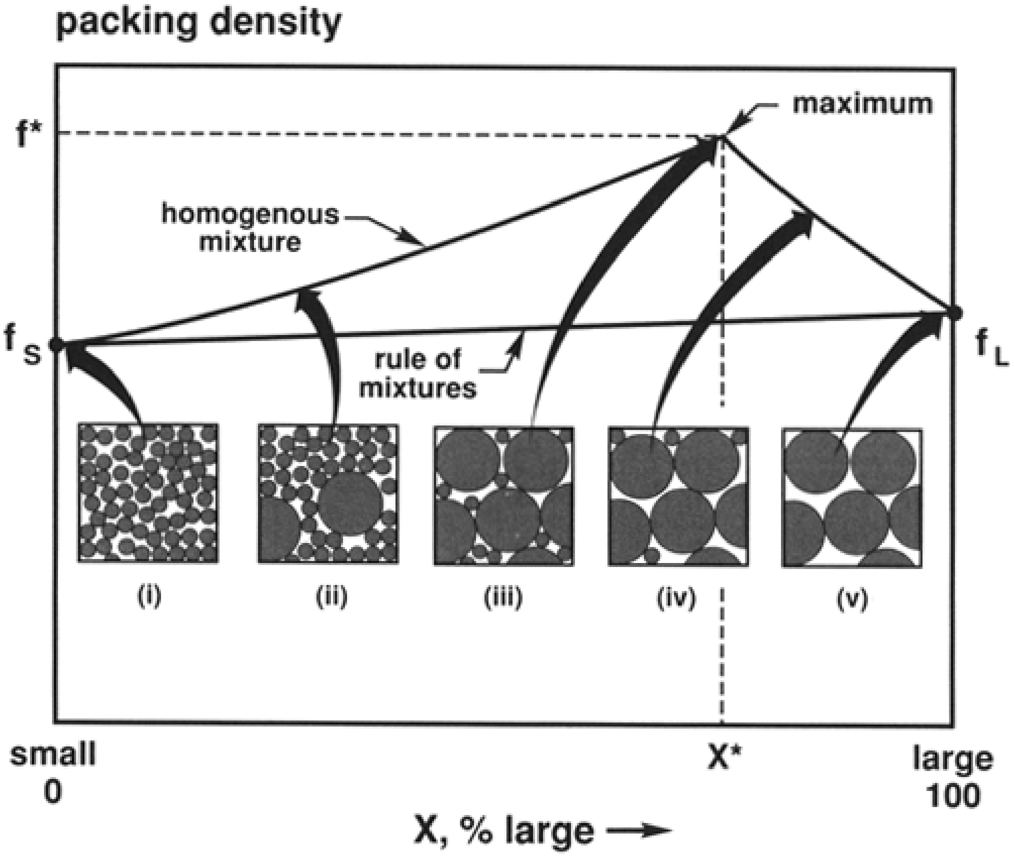

**Figure 3.4 Particle size distribution on binary powder packing density**[87]

### 3.1.4 Liquid Phase Sintering

Solid-state sintering can be improved by small portion of additives that segregates at grain boundaries and enhances the mass transport or even forms liquid phase. $Li_2O$ reduces the sintering temperature of Al nitride (AIN) from 1800°C to 1650°C.[21] Other compounds with low melting points, such as $Li_2CO_3$, $LiBiO_2$, $Ba(Cu_{0.5}W_{0.5})O_3$ are commonly used as additives to lower the sintering temperature.

When compacted specimen is sintered with a liquid phase, high densification rate and lower sintering temperature might take place. Liquid-phase sintering (LPS) process usually involves the addition or formation of second phase that have a liquidus temperature lower than sintering temperature.[88] Like solid-state sintering, the liquid-phase sintering is also thought to be a result of a reduction of the free energy of the system. Figure 3.5 depicts schematically the microstructural evolution of solid compact in the presence of a liquid phase in initial, intermediate and final stages. At the initial stage, particle rearrangement occurs with the formation of certain amount of liquid phase. The bonding of particles may form before reaching the liquidus temperature and isolated pores may leave in the compact. Capillary force then acts at solid-liquid interface to minimize the surface energy, leading to liquid phase penetration and shrinkage of the compact. The intermediate stage begins when solution-reprecipitation becomes dominant. For the annihilation of isolated pores, solution-reprecipitation is of critical. This process is characterized by size and shape change of particles and the development of solid-state skeleton. Atoms of solid particle dissolve into the liquid and diffuse to the neighbors where reprecipitation takes place. As mass transport, grain coarsening and pore filling by liquid phase result in better packing. Three mechanisms were proposed and shown in Figure 3,6: (a) liquid provides compressive force to pull two particles to contact together; (b) liquid phase accelerates the mass transport rate to dissolve the small particles; (c) solid state bonding is formed along the liquid wetted grain boundary. They may work together to improve densification during intermediate stages. Final densification then occurs with a much slower rate to annihilate the isolated pores due to existence of solid skeleton.

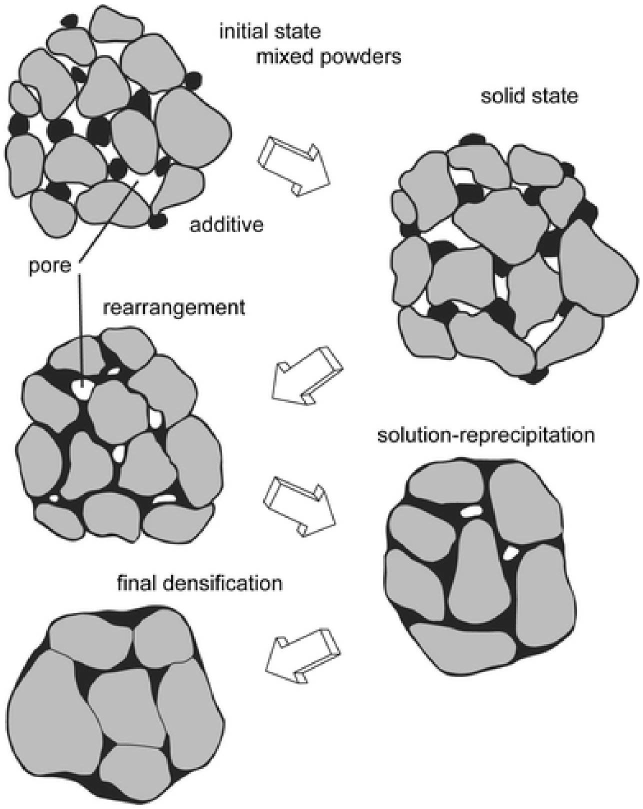

**Figure 3.5 Schematic showing the liquid-phase sintering process** 89

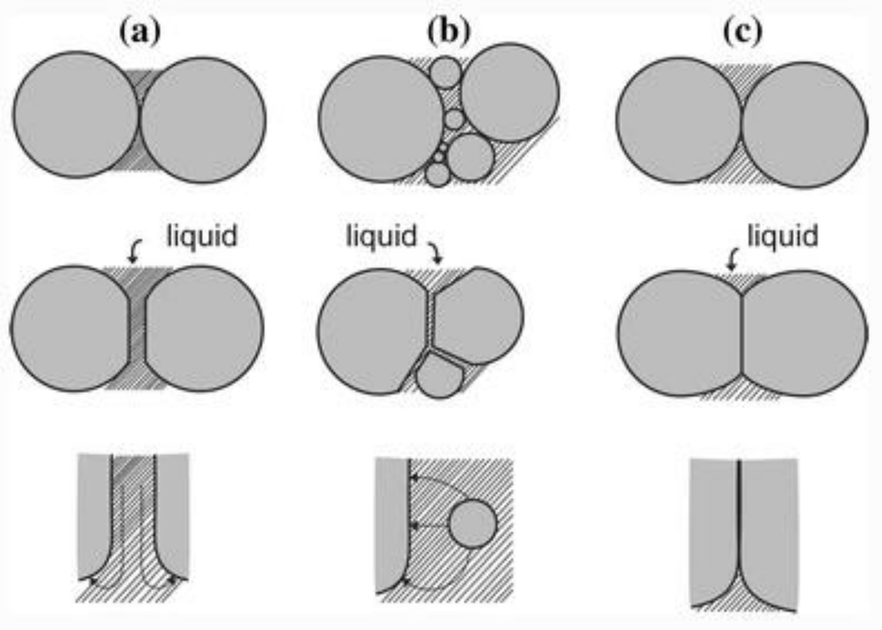

**Figure 3.6 Three mechanisms for densification during solution-reprecipitation process** 90

## 3.2 Effect of Ni Size on Microstructural and Electrical Properties of LSM:Ni Composites

### 3.2.1 Experimental Process

***Ni Powder Synthesis and Characterization:*** Three different size (1 µm, 100 nm and 10 nm) of Ni powder was used to prepare the LSM – Ni mixture. While Ni powder of 1 µm size was purchased from Sigma-Aldrich, Ni powder of 100 nm and 10 nm size was synthesized by a polyol method. The amount of surfactant capping agent was adjusted to control the size of Ni nanoparticles.Ni nanoparticles of 100 nm and 10 nm were synthesized using the polyol-hydrothermal method. In a typical synthesis, 1g (for 100nm) or 3.3g (for 10nm) polyvinylpyrrolidone (PVP; MW = 40,000) were dissolved in a flask of 30 ml of ethylene glycol (EG; 99.8%; Sigma-Aldrich) until completely homogeneous and clear. Then 0.46 g of nickel (II) formate dihydrate ( > 99.9%; Sigma-Aldrich) was dissolved under continuous magnetic stirring and heated to 140$_o$C. 0.1g of sodium borohydride ($NaBH_4$), serving as a reducing agent, was then added. The color of the solution immediately turned from green to black, accompanied by a gaseous hydrogen emission. The reduced Ni solution was held at temperature for 120 minutes before the solution was naturally cooled to room temperature and products were collected by centrifugation. Afterwards, the products were washed several times with acetone and dispersed in ethanol for further use. Dynamic Light scattering (DLS) measurements were carried out on a Horiba LB-550 Dynamic Light Scattering Nano-Analyzer to measure the size of Ni powder. Figure3.7 shows the size distribution and the mean particle size. Depending on the size, Ni powder was named as Ni-1000 (average particle size: 1050 nm), Ni-100 (average particle size: 94 nm) and Ni-10 (average particle size: 9 nm).

***Composite fabrication and characterization*:** $La_{0.8}Sr_{0.2}MnO_3$ ceramic powder was synthesized using a conventional solid-state method. Lanthanum(III) oxide ($La_2O_3$) (99.9% ,Sigma-Aldrich), Strontium carbonate ($SrCO_3$) (99.9% ,Sigma-Aldrich) and Manganese(II) carbonate ($Mn_2O_3$) (99.9% ,Sigma-Aldrich) were ball- mixed under a stoichiometric composition for 12hr, followed by a calcination process at $1100_oC$ for 4 hr. Calcined LSM power was mixed with Ni powder of 3 different size (1 µm, 100 nm and 10 nm) in ethanol . After 6 hour ball mixing using zirconia balls, the mixture of LSM and Ni powder was dried. For bulk ceramics testing, LSM:Ni mixed powder was pressed into pellets under a constant pressure of 8000 psi. Green body was sintered at $1400_oC$ in air for 6 hr. For thick film testing, LSM:Ni mixed powder was dispersed in a paste vehicle (Fuel Cell) and screen-printed on YSZ-NiO flat anode support. Dried film was then sintered at $1400_oC$ for dual atmosphere measurement. The phase after sintering was examined by X-ray diffraction (XRD; EMPYREAN; PANalytical diffractometer with Co Kα radiation) in a range of $2\theta = 20–80_o$ at a step size of $0.03_o$ (size of $0.005_o$ at slow scan size for details) and step rate of 0.4 s. The tube current was 40 mA, and a generator voltage of 45kV was applied. The morphology and element distribution were characterized by scanning electron microscopy (SEM; Apereo) and energy dispersive spectroscopy (EDS). X-ray photoelectron spectroscopy (XPS; Thermo Fisher ESCALAB 250 Xi) measurements were used for high resolution scans.

***Performance Test:*** LSM:Ni powders were mixed with a paste vehicle (FuelCellStore) and screen-printed on YSZ-NiO anode flat support, then sintered at $1400_oC$ for dual atmosphere measurement.[91] The resistance vs. temperature measurement was accomplished with a Keithley digital meter. Air and forming gas ($H_2/N_2$ = 5%) were applied as the oxidizing and reducing ambiances for the dual atmosphere measurement at an operation temperature of $700_oC$.

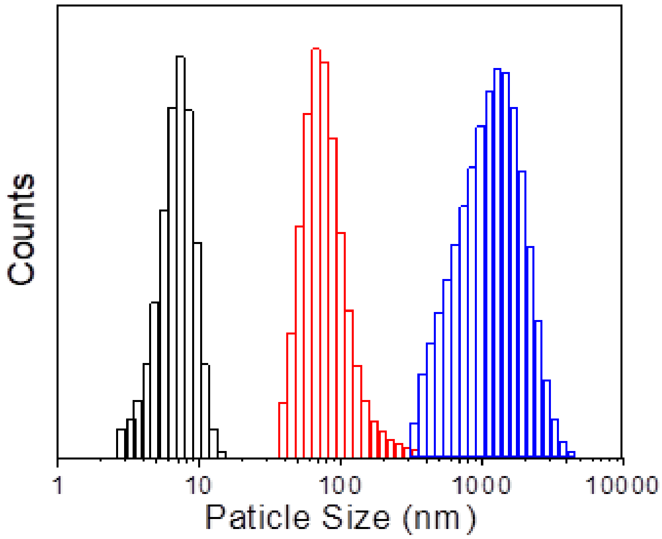

**Figure 3.7 Dynamic Light Scattering (DLS) nanoparticle size analysis for Ni particles with three different sizes**

**Table 3.1 Mean particles size calculated from the DLS data**

| | Mean particle size (nm) |
|---|---|
| Ni-1000 | 1050 |
| Ni-100 | 94 |
| Ni-10 | 9 |

### 3.2.2 Result and Discussion

Figure.3.8 shows the effect of the size and content of Ni particle on the microstructure of LSM-Ni composites which were sintered at 1400$_{o}$C in air. In LSM – 10 wt% Ni composites, a decrease in the Ni size 1 μm to 10 nm increases the grain size from 3 μm to 7 μm. In comparison to LSM – 10 wt% Ni composites, the grain size of LSM – 25 wt% Ni composite becomes smaller, but a decrease in the Ni particle size still increases the particle size. In LSM – Ni 1000 composites, the faceted second phase is clearly observed at the triple junction of the matrix grains and an increase in the Ni content increases the density of the faceted second phase. This indicates that the addition of large Ni particles leaves the second phase which pins the grain boundary movement and hinders the grain growth. LSM – Ni 100 composites do not show many second phase particles in both 10 wt% and 25 wt% added samples, suggesting that the role of Ni in the sintering depends on the Ni size. It is noted that the microstructure of 10 nm Ni added composites in Fig. 3.8(e) and (f) exhibit a ‘melted-like’ second phase. The trace of the melted phase is found along the grain boundary in Fig. 3.8(e) or grains are surrounded by the melted phase in Fig. 3.8(f). Given that polished samples were thermally etched at 900 $_{o}$C before SEM work, the microstructure of LSM – Ni 10 composites suggests that very fine Ni nanoparticles react LSM matrix and form the liquid phase near or lower than 1300$_{o}$C.

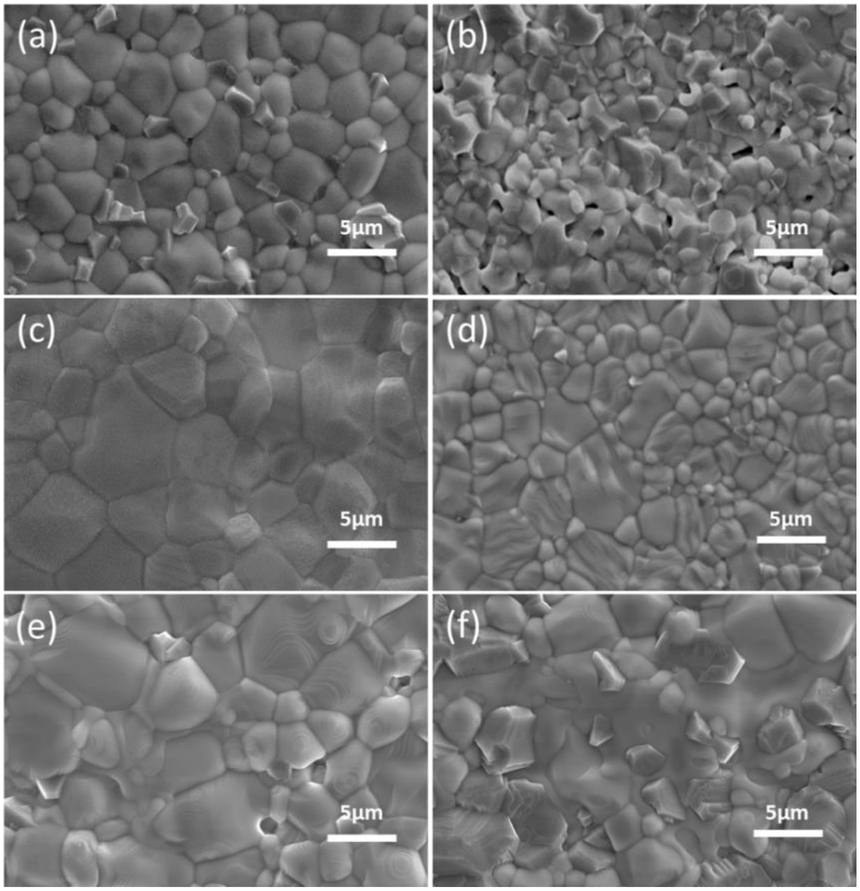

**Figure 3.8 Scanning electron microscopy micrographs of LSM-Ni composites: (a) LSM- Ni1000 (10 wt.%); (b) LSM- Ni1000 (25 wt.%); (c) LSM- Ni100 (10 wt.%); (d) LSM- Ni100 (25 wt.%); (e) LSM- Ni10 (10 wt.%); (f) LSM- Ni10 (25 wt.%);**

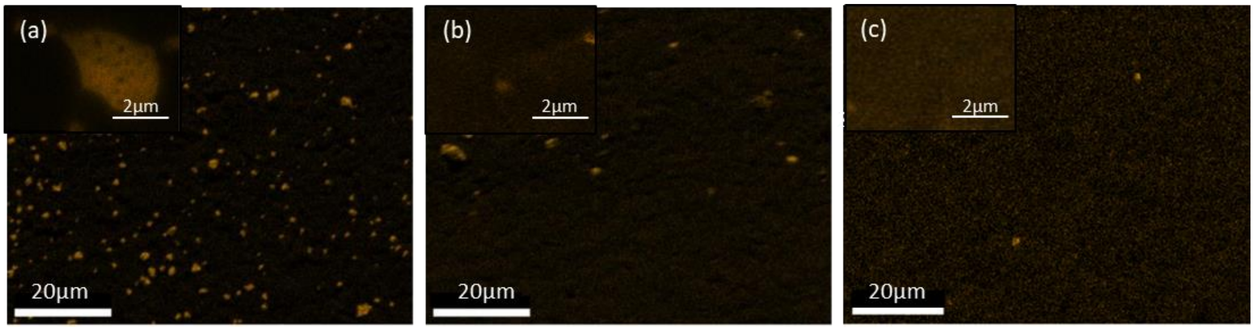

**Figure 3.9 Ni element distribution of LSM-Ni composites by energy-dispersive X-ray spectroscopy (characteristic X-ray intensity is collected as brightness of image, corresponding to the local relative of Ni concentration)**

In order to examine the distribution of Ni, EDS analysis was conducted. Figure 3 shows Ni element maps of 3 different LSM - 25 wt.% Ni composites. In Fig. 3.9 (a) of LSM - 25 wt.% Ni 1000 composites, the isolated bright areas with the size of 1 - 2 um are found. Given that the composites were sintered at 1400 $_{o}$C in air, the bright areas in Fig. 3.9(a) corresponds to NiO which were produced through the oxidation of Ni 1000 particles. This is consistent with the appearance of the second phase particles in SEM images of Fig. 3.8(a) and 3.8(b). In comparison to LSM – 1000 Ni, the size and density of the bright spots are decreased in the Ni element map of LSM – Ni 100. The isolated bright spots are rarely found in the Ni element map of LSM – Ni 10. Instead, the brightness of the matrix is uniformly increased, which suggests that the melted phase covering the surface of LSM – Ni 10 in Fig. 3.8(f) is comprised of Ni. The EDS map of 3 different LSM – 25wt% Ni composites show that the initial size of Ni particles controls the crystal structure and location of the second phase containing Ni.

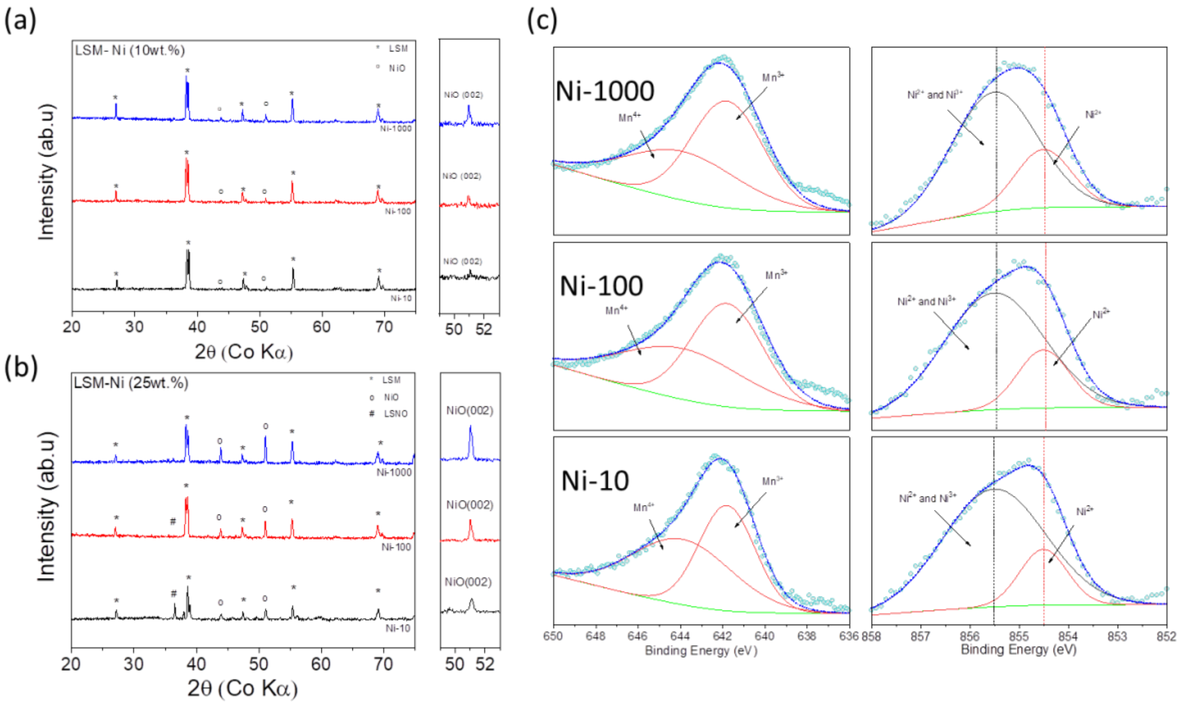

Figure 3.10 X-ray diffraction patterns of LSM-Ni composites: (a) Ni = 10wt.%; (b) Ni = 25wt.% and X-ray photoelectron spectroscopy of LSM-Ni composites.

Table 3.2 LSM main peak position for LSM-Ni (25 wt.%)

| No. | 2θ (110) ($_{o}$) | 2θ (104) ($_{o}$) |
|---|---|---|
| Ni-1000 | 37.67 | 37.99 |
| Ni-100 | 37.68 | 38.07 |
| Ni-10 | 37.82 | 38.17 |

The crystal structure of the Ni-related second phase in sintered LSM-Ni composites was investigated using XRD. Figures 3.10 (a) and 4(b) show XRD patterns of LSM – 10wt% and LSM – 25 wt% composites. Main peaks of LSM – 10wt% composites are attributed to a rhomohedral perovskite phase. In addition, peaks at 2θ = 43.89 and 51.02 $_{o}$ are due to NiO. Increase in Ni content increases the relative intensity of NiO peaks. Interestingly, a decrease in Ni particle size decreases the intensity of Ni (002) peak. Instead of NiO, tetragonal $La_{2-x}Sr_{x}NiO_{4}$ is found as the main second phase in the XRD pattern of LSM – 25 wt% Ni 10. The slow scan from 2θ = 49 $_{o}$ to 2θ = 51.02 $_{o}$ show that the replacement of Ni 1000 by Ni 10 decreases the intensity of NiO (002) peak of LSM – 25wt% Ni composites by 60 %. This suggests that a part of Ni in LSM – Ni 10 composites can react with LSM and form $La_{2-x}Sr_{x}NiO_{4}$ instead of being oxidized to NiO. A possible reaction between $La_{1-x}Mn_{x}O_{3}$ and Ni is given in equation:

$$3(La^{3+}_{1-x}Sr^{2+}_{x})(Mn^{3+}_{1-x}Mn^{4+}_{x})O_3 + Ni \rightarrow \left(La^{3+}_{1-y}Sr^{2+}_{y}\right)\left(Mn^{3+}_{1-y}Mn^{4+}_{y}\right)O_3 + (La^{3+}_{2-z}Sr^{2+}_{z})(Ni^{2+}_{1-z}Ni^{3+}_{z})O_4(3\mathrm{x} = \mathrm{y} + \mathrm{z}) \tag{3-4}$$

A new second phase in equation is $La_{2-z}Sr_{z}NiO_{4}$ which consists of an alternating layer of perovskite and LaO rock-salt along the c-axis. The formation of $La_{2-z}Sr_{z}NiO_{4}$ requires that more $Mn_{4+}$ (0.53 Å) replaces larger $Mn_{3+}$ (0.645 Å) to maintain charge balance. To characterize the content of $Mn_{4+}$, the position of LSM (110) and LSM (104) planes of LSM-Ni composites is summarized in Table 3. Decrease in Ni particle size decreases the lattice parameter of LSM, which supports that $La_{2-z}Sr_{z}NiO_{4}$ is formed in LSM – Ni 10 composites. To further examine the ratios of $Mn_{3+}/Mn_{4+}$ and $Ni_{2+}/Ni_{3+}$, the binding energy of Mn and Ni was characterized. Mn 2p3/2 peak in Figure 3.10(c) is deconvoluted into two peaks. A peak at 641.9 eV is assigned to $Mn_{3+}$ and the other peak at 644.9 eV is assigned to $Mn_{4+}$.[95,96,97] Figure 3.10(c) shows that the decrease in Ni particle size facilitates the appearance of $Mn_{4+}$. Ni 2p3/2 peak in Figure 3.10(d) is also deconvoluted into 854.5 eV and 855.5 eV. Each peak is assigned to the different oxidation status of Ni or the satellite peak of Ni. The peak at 854.5 eV shows the relative content of $Ni_{2+}$ which is in both $La_{2-z}Sr_zNiO_4$ and NiO. A peak at 855.5 eV is attributed to $Ni_{3+}$ of $La_{2-z}Sr_zNiO_4$. The decrease in Ni particle size also increases the relative content of $Ni_{3+}$, suggesting that more Ni is converted to $La_{2-z}Sr_zNiO_4$ instead of being oxidized to NiO. This attests that a change in the Ni particle size controls the ratio of $La_{2-z}Sr_zNiO_4$ and NiO in sintered LSM – Ni composites.

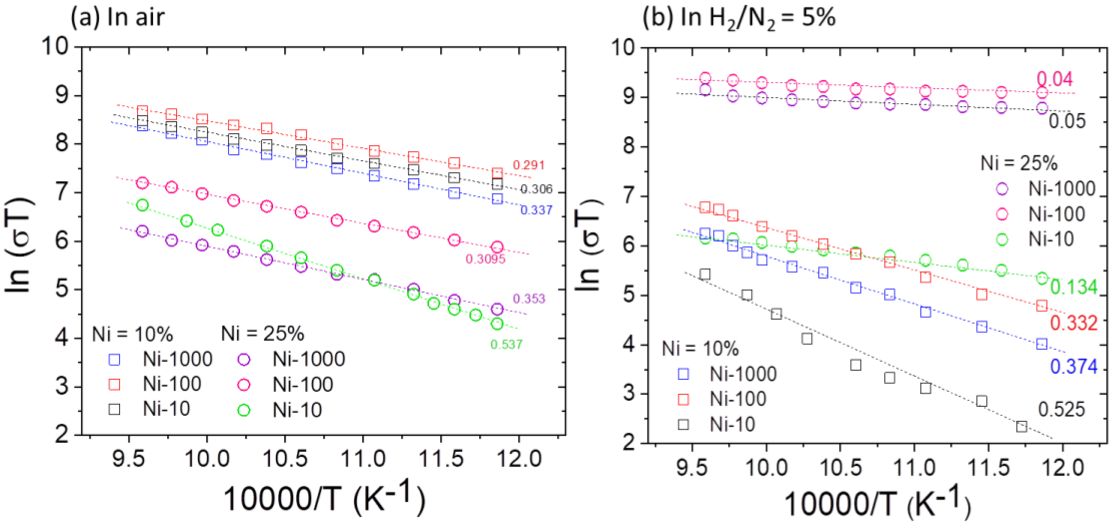

**Figure 3.11 Arrhenius plot of the temperature dependence of electrical conductivity for LSM-Ni composite with different Ni size and content: (a) in oxidizing atmosphere; (b) in reducing atmosphere (H2/N2= 5%)**

The electric conductivity of LSM – Ni composites in air and reducing atmospheres is shown in Figure 3.11. The measurement was carried out in the temperature range from $560_oC$ to $780_oC$. In air atmosphere, the electrical conductivity rises with increasing the temperature. Given that LSM is conductive in the air atmosphere and all of Ni is oxidized at this temperature range, the electric conduction occurs along the LSM matrix of LSM – Ni composites via a typical small polaron hopping (SPH) mechanism.[98,99] The value of conductivity σT as a function of temperature follows an Arrhenius relation:

$$\ln (\delta T) = \ln A - \frac{W_H}{2K_B}\frac{1}{T} \tag{3-5}$$

where $W_H$ is the activation energy of polaron hopping. A = , where n is the polaron density, a is the hopping distance and $v_0$ is the frequency of phonons. In Fig. 3.11(a), LSM – 10 wt% Ni-1000, LSM – 10 wt% Ni-100 and LSM – 10 wt% Ni-10 have the similar electric conductivity and their slope, proportional to the activation energy is close to 0.3 (0.33, 0.29 and 0.31). The increase in the Ni content of LSM – Ni composites decreases the conductivity, since the content of less conductive NiO in the composites is increased. LSM – 25 wt% Ni-1000 and LSM – 25 wt% Ni-100 have the activation energy of 0.31 and 0.35, which is close to that of other LSM – Ni composites in the air atmosphere. A very different slope (0.54) is found LSM – 25 wt% Ni-10 that has a large amount of $La_{2-z}Sr_zNiO_4$. This higher dependence of LSM – 25 wt% Ni-10 on temperature is due to the high temperature conductivity of $La_{2-z}Sr_zNiO_4$. When placed in a reducing atmosphere, LSM – Ni composites exhibit different ln (σT) vs. 10,000/T curves. Two major changes in the reducing atmosphere are the formation of oxygen vacancies in LSM matrix and the reduction of Ni in the NiO second phase. The former decreases the electric conductivity, while the latter increases it. In the reducing atmosphere, all of LSM – 10 wt% Ni-1000, LSM – 25 wt% Ni-100 and LSM – 10 wt% Ni-10 possess lower electric conductivity. This suggests that the formation of oxygen vacancies in LSM matrix play a crucial role in the electric conductivity of

LSM – 10 wt% Ni samples. However, in LSM – 25wt% Ni composites, the change from the air atmosphere to the reducing atmosphere dramatically increases the electric conductivity. In addition, the increase in temperature decreases the electric conductivity of LSM – 25wt% Ni composites, which is the intrinsic property of metals. As the Ni content becomes larger than the percolation threshold (~0.3) charge carriers can transport along a metallic percolation path and through the LSM matrix as polarons. Temperature dependence of the conductivity in Figure 3.11 reveals that the reduced Ni phase produces a percolation path and determines the electric conductivity.

From the microstructure, crystal structure and electric conductivity of LSM – Ni composites, it is concluded that Ni particles in LSM can be converted to NiO or $La_{2-z}Sr_zNiO_4$. As the Ni particle size decreases, more $La_{2-z}Sr_zNiO_4$ is formed. LSM – 25wt% Ni 100 composites have an optimum ratio of $La_{2-z}Sr_zNiO_4$ and NiO which helps the sintering in air atmosphere and the formation of the metallic percolation path in reducing atmosphere.

# 4.0 LSM/LSM:Ni Double Layer Interconnects for SOFCs and SOECs

## 4.1 Background & Motivation

### 4.1.1 Motivation

The increment of the demand for clean energy as well as the depletion of fossil fuel stimulates the researches on SOFCs/SOECs. Currently, the major bottlenecks are the metal ion release from the metallic interconnect and large thermal expansion coefficient (TEC) of metallic interconnects that make it almost impossible for the metallic interconnects to be commercially available in this field. Ceramic coating layers are highly required to protect the metallic interconnect. But unfortunately, the oxygen partial pressure significantly affects the electrical conductivity of ceramics. In the case of a p-type LSM materials, the electrical conductivity in air is several orders of magnitude larger than the one in reducing ambiance.

Indeed, the ceramic coated metallic interconnect is an effective approach to fabricate the interconnect that meets all the requirements as an interconnect of SOFs/SOECs. However, the complex on structure and the cost boosted dramatically at the same time.

The study in this chapter focuses on the design a dual-layer interconnect as an alternative to the current interconnect. LSM:Ni composites forms a highly conductive and dense layer to anode side with reasonable thermal expansion coefficient (TEC).[100] LSM serves as the p-type layer to cathode side. The double layer interconnect is coated layer-by-layer on a YSZ-NiO anode support. The porous YSZ-NiO anode provides reasonable strength to support everything on the top with negligible resistivity. The feasibility of LSM/LSM:Ni dual-layer interconnect on YSZ-Ni anode support is examined with simulated environment, with dual atmosphere at high operation temperature.

### 4.1.2 Interconnect Materials Development

In the decades, significant progress has been observed in the researches on SOFCs/SOECs, making them closer to the goal of commercialization. As introduced in Chapter 01, in order to accumulate the voltage output for applications, such as power plants, single cell with only ~1eV is far than enough, instead, multi-stacked cells are utilized via connection by electrodes layer, named interconnect. Two major purposes of interconnects are: 1) electrically connect one anode to the cathode of the neighboring cell; 2) physically block the gas flow to avoid or at least retard the reduction of cathode layer or the oxidation of the anode layer. Besides, the design should take mechanical strength into consideration. 100-101

There are several stringent requirements that is essential for the design of interconnects:101

1) Interconnect should exhibit excellent electrical conductivity but limited ionic conductivity under the operation temperature and atmospheres (oxidizing from cathode side, reducing from anode side). Ideally, the power density of single cell with and without interconnects should be comparable without obvious difference.

2) Interconnect should maintain high stability in regards to chemical reaction, microstructure, diffusion and so on, under the specific operation conditions. Considering that interconnect is exposed to oxidizing ambiance on one side, and reducing ambiance on the other side at operation temperature around 800$_o$C, any chemical reaction at interfaces between cathode/interconnect, anode/interconnect, interconnect/air, interconnect/forming gas, would result in potential degradation of the cells.

3) Interconnect should have adequate density to prevent direct combination of oxygen and fuel under operation condition. Ideally, interconnect is capable to block all the gas flow to eliminate the formation of water.

4) Interconnect should hold matching thermal expansion coefficient (TEC) with other components of the cells. Since the SOFCs/SOECs are consisted of hundreds of cells. Small mismatch might introduce significant thermal stress and lead to severe warping or cracking.

5) Interconnect should be fabricated with simple process for large-scale manufacturing application. The cost of the fabrication and raw materials are desired to be as low as possible for commercialization.(Currently, Pt is pricy for interconnect of SOFCs/SOECs)

Traditionally, interconnects can be classified into ceramic interconnects and metallic interconnects. Based on the rigorous requirements of interconnect, the selection of ceramic materials is limited to complex oxides. For perovskite oxides, the electrical conductivity is closely related to the oxygen partial pressure. They are either p-type or n-type by dopant. Even for $LaCrO_3$, one of the most promising ceramic interconnect candidates, the electrical conductivity in reducing ambiance is order of magnitude lower than the one in oxidization ambiance.[3] Considering the wide spectrum of oxygen partial pressures that interconnect should endure under operation condition, the implications for the dependence of the polaron hopping mechanism on the oxygen partial pressure is of great importance. Metallic interconnect thereby attracted more attentions due to their negligible small omhic losses and their independence of oxygen partial pressure. However, the formation of oxides due to the interfacial reaction is usually inevitable.[103-104] The oxide scale might cause severe ohmic losses and chemical instability. Also, the thermal expansion coefficient (TEC) mismatch between metallic interconnect and other components of the cells might be larger. Furthermore, Chromium usually makes alloys corrosion resistant. However, when the metallic interconnect is placed at high temperature in oxidizing or high humidity environment, Chromium vaporization and oxide scale growth are inevitable. These species significantly affect the performance of the cells and probably result in severe degradation of the cells. Currently, no alloys are commercially available to meet the stringent requirements as interconnect.[105-106] Protection ceramic layers are coated on the surface of metallic interconnect as an effective solution. However, the cost and complex of interconnect is thereby increased.

### 4.1.3 General Consideration on Fabrication

Ceramics can be fabricated by a wide variety of techniques, which can be divided into two groups:[107-109] a) with the preparation of slurry, like tape-casting, slip-casting, dip-coating, screen printing and etc. b) via projection to a target, like plasma spraying. Other technologies, involving a gaseous phase, such as physical vapor deposition (PVD) and chemical vapor deposition (CVD), are relatively expensive and hard to scale-up. Significant efforts have been devoted to ceramic interconnect fabrication with high density, In the flow chart shown in Figure 4.1, the fabricate route of ceramics from powders via slip casting method. Each procedure has the potential for introducing undesirable microstructural flaws that fail to satisfy very demanding property requirements.

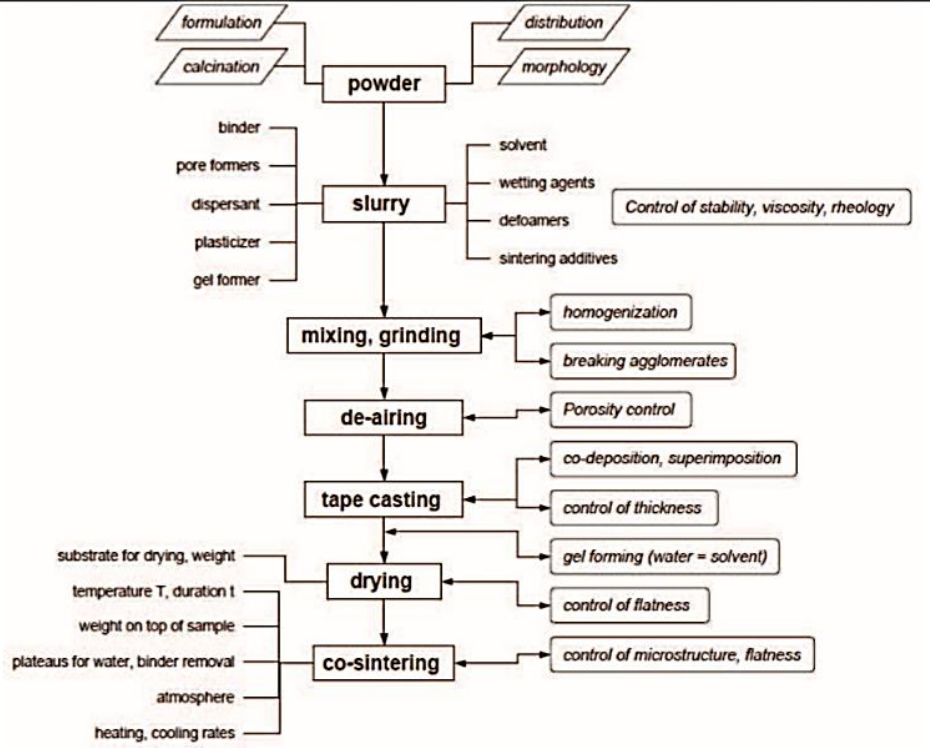

**Figure 4.1 The fabricate processing of mulit-layer tape casting and co-sintering** [110]

Tape-casting[111] is one of the cheapest processes to fabricate thick layer, basically in the range of 10 – 300 um. It also allows variety of morphologies from microstructure with high porosity to highly dense microstructure. These features make it the best choice for our dense interconnect coating. Slip-casting,[112] on the other hand, is a good choice for shaping the anode support with porosity. Figure 4.2 is the processing diagram of the fabrication process. As discussed in previous chapter, sintering, or namely firing, has been well studied. Close attention must be paid to the processing steps, slurry preparation and casting that are prior to firing. As it known to all, any uniformity of the packing or mixing in the green body would be exaggerated in the sintering process. Ceramic additives,[113-115] such as binder, dispersant and plascticizer are of importance for slurry preparation, leading to homogeneous packing in consolidated materials. Usually the slurry may undergo a long-time milling process to make sure that the large agglomeration has been destructed. The effect of key slurry preparation parameters, such as the ratio of ceramic powder/dispersant or the ratio of dispersant/binder are taken in consideration to adequately control the microstructure of the fabricated layer.

The powders are dispersed in the solvent and stabilized using dispersant to prevent the agglomerates or flocculation. Widely used dispersants can be classified into three groups: short-chain polymers or surfactants, low to medium molecular weight polymers and simple ions and molecules. In this study, the low to medium molecular weight polymers are used as dispersants. Polyethylene glycol (PEG), Poly vinyl pyrrolidine (PVP), Poly vinyl alcohol(PVA) are common non-ionic polymers with low to medium MW. [113-115] This type of dispersant holds the features that it can be dissolved in water, connect with particles via Van der Waal's force or coordination. Also, it can be used as binders as well. Binder helps to strength the green body before sintering. So, it is critical for our research. Usually, the viscosity of solutions would increase with binder concentration and molecular weight. For some cases, binder works on the plasticity, flocculation, thickening and rheological control and liquid retention. Meanwhile plasticizers work opposite to binder, which on the other hand, leads to bad packing and reduced the Van der Waal's force to soften the paste and to increase the flexibility.

One of the more troublesome problems is the effect of minor variations in the chemical composition. Organic components remain in the coating after drying process should be carefully removed by heat treatment to maintain the purity of products. Unless porosity is a requirement, the pores left by organic components can be left. In most cases, high density and uniform microstructure is expected. Pores must be eliminated during sintering process, but the formulation of slurry, which related to the final microstructure has to be considered carefully.

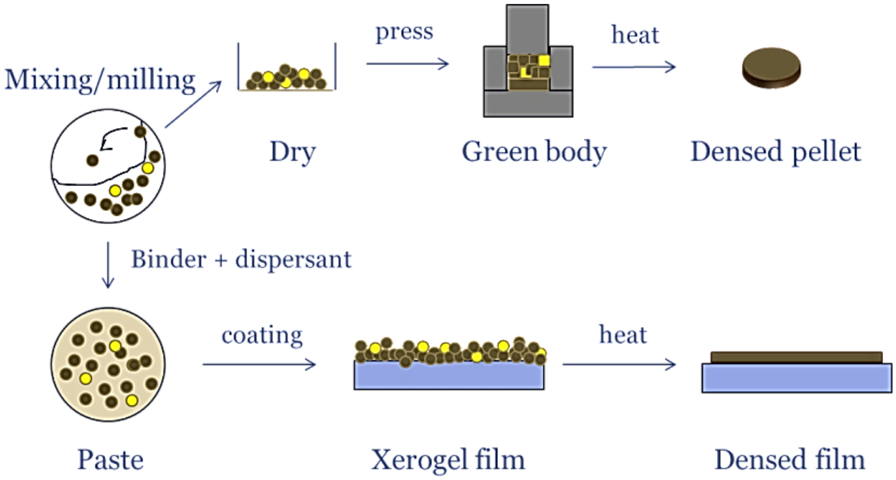

**Figure 4.2 Process difference for pellet preparation and paste preparation**

### 4.1.4 Co-sintering of Multi-Layer Stacks

A common difficulty in the multi-layer stack is the shrinkage mismatch may take place during co-sintering process, with the result as severe mechanical failures, such as warping, cracking and bending.

During sintering process, each layer in the stacks undergoes same heat temperature, duration and atmosphere, such as air or forming gas. Reaction, diffusion and precipitation are possible to occur at the interfaces. The temperature and duration selection should be really precise to avoid the chemical instability but can sinter certain layer to obtain high density.

Besides composition changes at the interfaces for each layer, deformation is another problem during co-sintering. As shown in the Figure 4.3, ideally, the shrinkage rate between each layer is competitive with each other, leading to a flat and dense final product. However, if the shrinkage mismatch is large among multi-layer, the final product would concave upwards or downwards or simply become not flat.[116] The consequences are 1) hard to seal; 2) large contact resistance. In some reports, it is preferred to do co-sintering for odd-number layers. For double layers, it is almost impossible to eliminate the shrinkage mismatch during the densification. But for three-layered structure, the mismatch from top layer can be compensated with the mismatch from bottom layer. Other deformations such as elastic deformation, thermal deformation and visco-plastic deformation might also cause the severe problems like cracks.

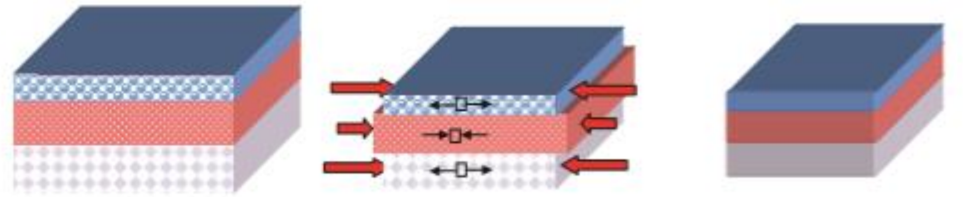

**Figure 4.3 Schematics of the double-layer interconnect coating on anode support** [116]

### 4.1.5 A/B Atomic Ratio of $(La,Sr)MnO_3$

Anther common difficulty in the multi-layer stack is the interfacial reaction, that might change the original composition of the coating layer. In contrast to the compacts, dense film is fabricated on YSZ-NiO anode support followed by the co-sintering. Chemical stability at the interfaces can be regarded as essential to achieve the good performance after so-sintering . Notably, crystal structure characteristics, such as lattice parameters and volume changes caused by the A/B atomic ratio are minor compared to A-site substitution. But a compositional change on the A/B ratio may result in the formation of undesired resistive second phase due to the interfacial reaction between interconnect LSM materials and anode YSZ/NiO materials.

Many efforts have been taken to address the problem of the interfacial reaction between LSM and YSZ system. A ternary phase diagram of $(Zr,Y)O_2 – La_2O_3 – Mn_3O_4$ at 1400$_o$C is presented in Figure 4.4. Fluorite cubic Zr phase instead of 3YSZ has equilibrium with LSM pervoskite at high temperature. When (La,Sr)/Mn >1, La is excess that introduces the second phase $La_2O_3$. $La_2O_3$ reacts with YSZ at interface to form the resistive $La_2Zr_2O_7$ or soak the water in the environment to form $La(OH)_3$, which is unstable and easily decomposed again in two steps, following the equations: [118]

$$La(OH)_3 \rightarrow LaOOH + H_2O \tag{4-1}$$

$$2LaOOH \rightarrow La_2O_3 + H_2O \tag{4-2}$$

This decomposition would eventually result in severe cracks or even defoliation. If our dual-layer interconnect is co-sintered with YSZ-NiO anode support, the interfacial reaction between $La_2O_3$ should be eliminated. The formation of $La_2Zr_2O_7$ is detrimental significantly to the conductivity. Conversely, when (La,Sr)/Mn < 1, excess Mn exists in the form as $Mn_3O_4$. At elevated temperature, it has been reported that slightly B site excess leads to the retardation of the formation of $La_2Zr_2O_7$ because that $Mn_3O_4$ is hard to reach equilibrium with $La_2Zr_2O_7$ at high temperature.

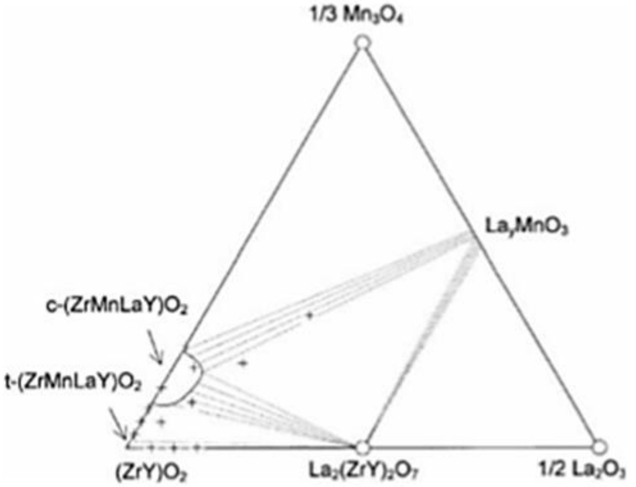

**Figure 4.4 Ternary phase diagram of $(Zr,Y)O_2$ – $La_2O_3$ – $Mn_3O_4$ system at 1400°C in air. (3mol.% $Y_2O_3$-$ZrO_2$)** [117]

Moreover, J.A.M.van Roosmalen et al.[119] studied the A/B ratio effect on sintering behavior of $(La,Sr)MnO_3$ system. The ratio of A/B equals to 0.91, 1.00 and 1.03, respectively. As shown in the Figure 4.5, when x = 0.91, La vacancies are formed to maintain the charge neutralization. The total mobility is high due to the increment of vacancies on A sites and the sintering temperature is thereby pushed to lower temperature. The sintering process is improved. When x= 1.03, Mn vacancies are formed with limited La vacancies. The total mobility is low and the grain growth is retarded. D.LaurenceMeixner et al.[120] also reported that Mn excess improves the sintering behavior, while La excess would introduce secondary phase and inhibit the sintering process. However, it is noticeable that the diffusivity of Mn towards YSZ-NiO anode support is high. Too much Mn excess might cause the precipitation of Mn from perovskite crystals and severe diffusion of Mn. Whereas the benefits of slightly B-site excess have been demonstrated, the interfacial reaction problems during co-sintering of interconnect coated YSZ-NiO anode support can be suppressed effectively without deduction on sintering behavior.

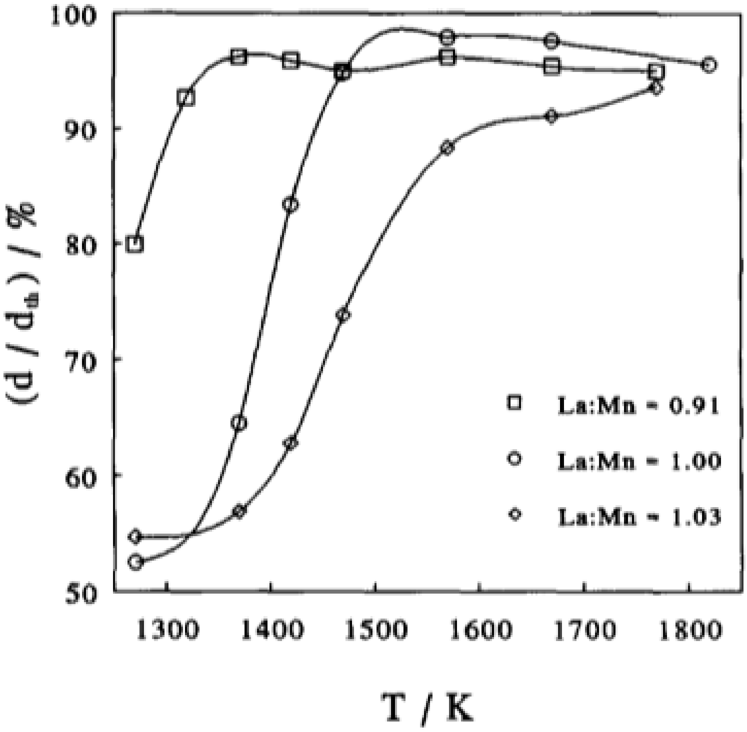

**Figure 4.5 Densification as fraction of sinter temperature for La/Mn ratio** [120]

## 4.2 Design of LSM/LSM:Ni Dual Layer Interconnect on Anode Support

One of the challenging in developing the interconnect of SOFCs/SOECs is in simplifying the design of interconnect that offers high conductivity and density with less ambiance-dependency under high temperature and dual atmosphere operating conditions. Recently, the design of double layer ceramic interconnect has been studied and discussed by several groups.[121-122] The strategy is to fabricate the n-type ceramics/ p-type ceramics double layered interconnect. N-type ceramics, such as $Sr_{1-x}La_xTiO_3$ (SLT), only show high electrical conductivity on anode sides, meanwhile p-type ceramics, like $La_{1-x}Sr_xFeO_3$ (LSF) only exhibit good electrical properties on cathode sides. Since the conductive ceramics are sensitive to oxygen partial pressure, severe degradation of performance would occur for slight gas leaking or exceed oxygen diffusion. Also, the interfacial reaction between n-type/p-type ceramics is inevitable. In our design, a double layered ceramic-based interconnect with high electrical conductivity and stability in both oxidizing and reducing ambiance at high temperature as well as with impermeability to gases, has been proposed and discussed. Nanostructured Ni, forming metallic percolation, compensates the electrical conductivity loss by LSM in reducing ambiance.

Anode supported cells have the features of having thin electrolyte, which effectively reduces the ohmic loss causing by the thickness and potentially lower the operation temperature of the cells.[24] In this study, the dual layer interconnect will be coated on the YSZ-NiO porous anode support. The major key for this chapter is to optimize the fabrication process by adjustment the composition of each layer to eliminate: 1) shrinkage mismatch between LSM and LSM:Ni dual layer coatings; 2) chemical reaction at the interface of anode support and interconnect coating. Taking the advantage of the shrinkage of anode support, the dual-layered interconnect holds high densification after co-sintering with good ASR stability in dual atmosphere (one side in air, the other side in reducing ambiance) at high temperature.

### 4.2.1 Sample Preparation

Slip casting is a conventional method to prepare bulks with moderate porosity. Steps involved in the slip casting process when fabricating our YSZ-NiO anode support are slurry preparation, casting and drying. Figure 4.6 presents the schematics of slip casting process and the scalability of anode support size. The water in the slurry was capillary sucked by the porous brick and coagulates of the power were left near the mold surface. The slurries were prepared by 2.4wt.% Darvan 811 as dispersant, and 1wt.% PEG as binder. pH value was adjusted to 7.5 by each step to maintain an reasonable storage life. Three different sizes are slip casted, 10mm, 20mm and 32mm in diameter with YSZ/NiO weigh ratio = 5:5, 6:4 and 4:6. With the diameter of specimen increment, the strength required is higher so that the specimen would not break in the middle.

LSM-based double layer interconnect were coated using tape casting method. By adjusting the powder/vehicle ratio was maintained to 1:1. Ethanol was used as solvent to assist the coated layer thin and uniform. The interconnect layer were then co-sintering with anode support at 1400$_o$C for densification.

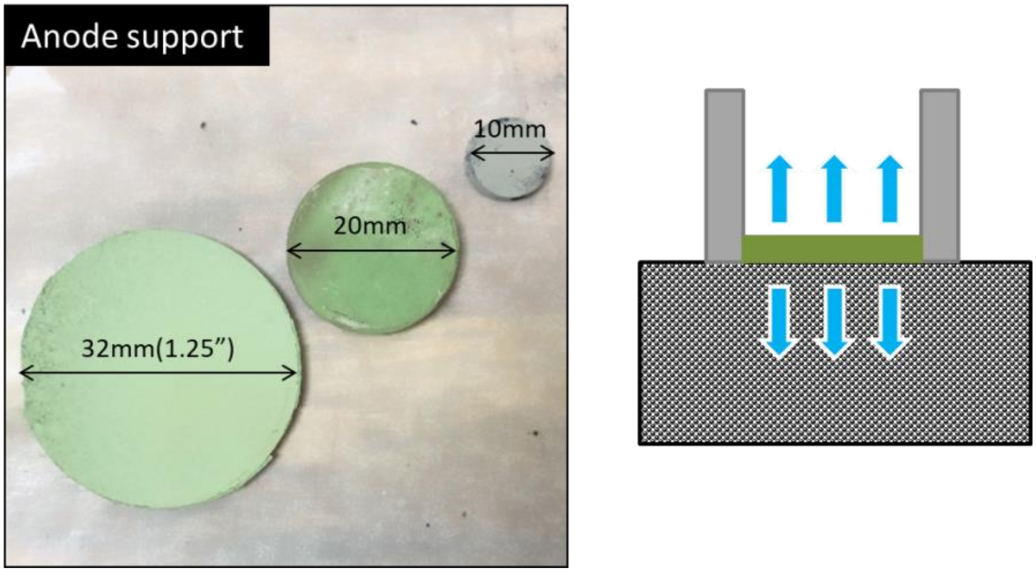

**Figure 4.6 YSZ-NiO anode support with different sizes**

### 4.2.2 Shrinkage Mismatch Between Dual Layer Coatings

To overcome the shrinkage mismatches for double layers interconnect, the shrinkage adjustment is carried out by either changing the $Sr^{2+}$ doping level on LSM layer or adding Ni with different size to the LSM:Ni layer. If the shrinkage rate between two interconnect layer is different, after co-sintering, residual stress between LSM layer and LSM:Ni layer may result in problems including the formation of cracks and separation of coatings. In this case, shrinkage adjustments are feasible and effective approaches to eliminate the residual stress between dual layers. In this chapter, the shrinkage rate of $La_{1-x}Sr_xMnO_3$ layer is adjustable by Sr dopant, with x = 0.1, 0.2 and 0.3. Meanwhile, the shrinkage rate of LSM:Ni layer can be effectively tuned by the Ni particle size, as discussed in Chapter 03. The additional phase Ni has turned out not to produce undesired reactants that might result in the deterioration of properties.

The Sr dopant content significantly influences the properties of LSM, such as morphologies and electrical properties. The substitution of $La^{3+}$ with larger ion $Sr^{2+}$, leads to the increment of Mn-O-Mn angle and the reduction of Mn-O length in the lattice. Furthermore, the electrical conductivity is a function of Sr dopant level x. As the status of transition metal with mixed valences $Mn^{4+}/Mn^{3+}$ changes, there is an increasing or decreasing on polaron density correspondingly.

Figure 4.7 shows the phase diagram and surface morphologies of $La_{1-x}Sr_xMnO_3$ with x=0.1, 0.2 and 0.3. The lattice parameters display a decreasing trend with $Sr^{2+}$ content. In general, $Mn^{4+}$ with higher valence, usually has a smaller ionic radius (0.53Å) compared to the ionic radius of $Mn^{3+}$ (0.645Å). [22] In this regard, a contraction of lattice take places with a result of higher internal stress in the lattice. Figure 4.7(a) shows the XRD patterns of single-phase $La_{1-x}Sr_xMnO_3$ (x=0.1, 0.2, 0.3). A slight shift towards larger 2theta has been observed with x, indicating an increment on internal stress. In addition, when more $Sr^{2+}$ substation is added, the microstructure of LSM changes as well as seen in Figure 4.7 (b). The mean grain size drops from 4.3um to 2um with x increasing from 0.1 to 0.3. The mean grain size and grain size distribution are shown in Figure 4.8.

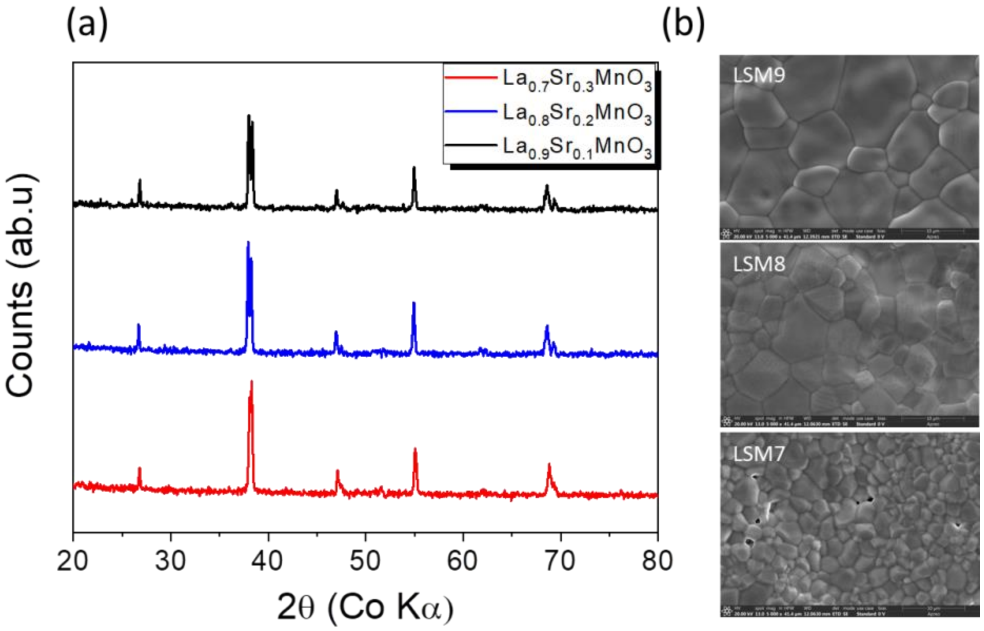

**Figure 4.7 (a) XRD phase diagram and (b) SEM image for La1-xSrxMnO3 with x=0.1, 0.2 and 0.3**

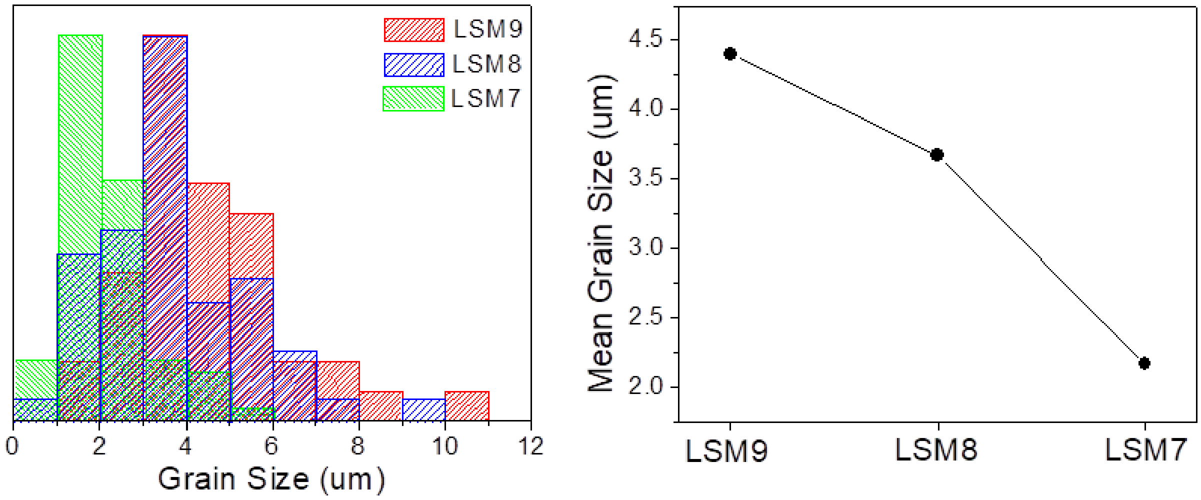

**Figure 4.8 Morphologies, Grain size distribution and mean grain size comparison**

Figure 4.9 illustrates the shrinkage rate, density and resistivity of $La_{1-x}Sr_xMnO_3$ (x=0.1, 0.2, 0.3), marked as LSM9, LSM8 and LSM7. Due to the retardation of grain growth with more $Sr^{2+}$ content, the density and shrinkage rate after sintering also drops, shown in Figure 4.9(a). However, the electrical performance is expected to be better with more $Sr^{2+}$ content, by introducing more polarons and reducing the hopping distance. The change in resistivity is in magnitude order, shown in Figure 4.9(b). Careful compromise between resistivity and shrinkage rate become the serious consideration.

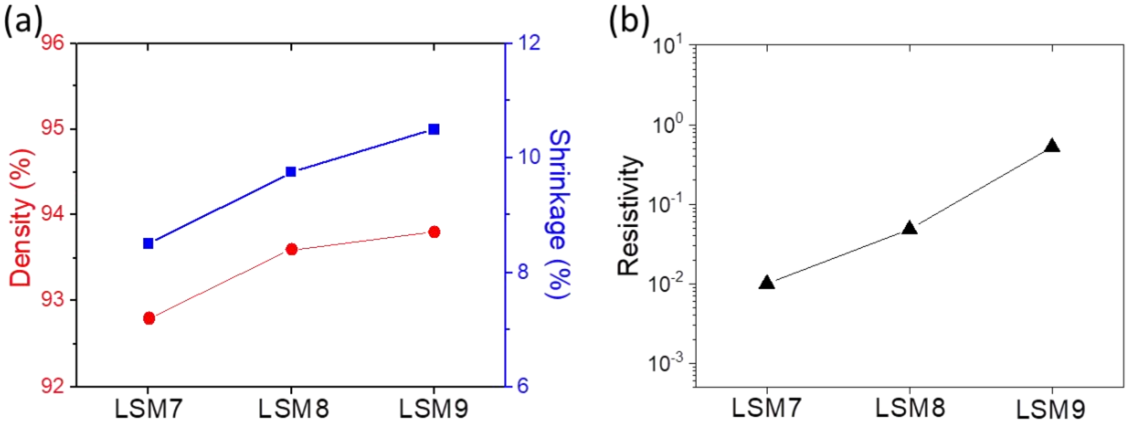

**Figure 4.9 (a) Shrinkage and density; (b) Hall Effect measured resistivity for La1-xSrxMnO3 with x=0.1, 0.2 and 0.3**

As discussed in Chapter 03, by mixing LSM with Ni particles with different size, the morphologies of LSM:Ni composite is promising to be improved by formation of second phase. In Figure 4.10, Ni-100 shows an extremely high density > 99%. The tangential shrinkage rate is close to the tangential shrinkage rate of LSM8. Therefore, it is reasonable to say LSM8 and LSM:Ni-100 have limited shrinkage mismatch.

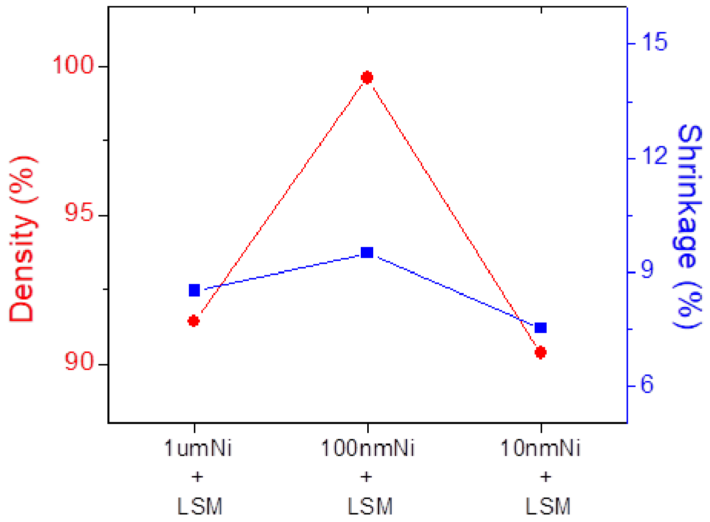

**Figure 4.10 Shrinkage rate and density for LSM:Ni with different Ni particle size**

### 4.2.3 Shaping and Shrinkage of YSZ-NiO Anode Support

Besides the shrinkage mismatch between dual interconnect coating, the shrinkage for YSZ-NiO anode support is also critical and might be the key factor for fully densification of topping interconnect coatings. Homogeneity of the slip casted YSZ-NiO anode support can be improved by tuning the ratio of binder, dispersant and water loading of the slurry. Good YSZ-NiO anode support has no Ni gradient throughout the thickness, which avoids warping of samples during sintering. Say, if Ni precipitates during slip-casting at the bottom, the shrinkage mismatch between Ni-rich bottom layer and Ni-deficient top layer would be magnificent, which leads to concaving or cracks. As shown in Figure 4.11, distribution of Y, Zr and Ni elements are uniform when Dispersant is 2.4wt.% and binder is 3wt.%. Ni did not precipitate due to heavier weight.

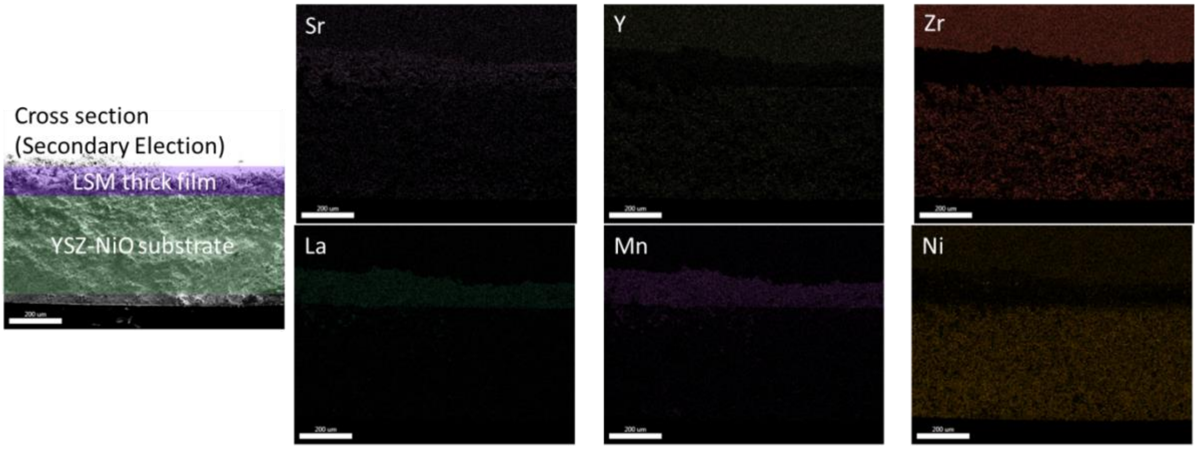

**Figure 4.11 EDS mapping of distributions of elements throughout the samples after sintering**

The shrinkage of YSZ-NiO anode support can be effectively controlled by the ratio of YSZ-NiO. NiO serves as sintering inhibitor, restricting the shrinkage dramatically. So that NiO is usually mixed with YSZ to obtain porous structure. In Table 4.1, the shrinkage rate drops from 22% to 6% when YSZ/NiO ratio changes from 10:0 to 4:6. The YSZ/NiO ratio also has influence on the resistance. As anode support, the layer should has negligibly small resistance by reducing NiO into Ni. In Figure 4.15, it is presented that reduced thickness and lower YSZ/NiO ratio cause the reduction of resistance.

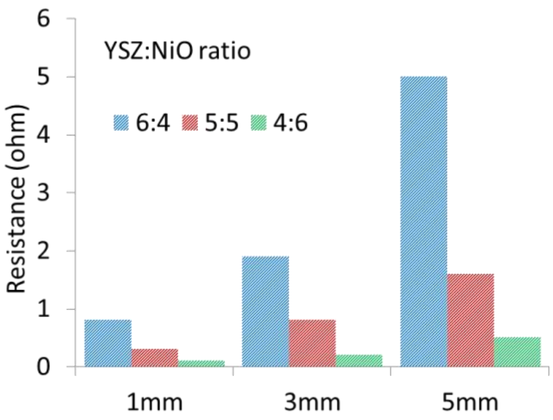

**Figure 4.12 Shrinkage ratio of YSZ:NiO anode support with different thickness and composition**

**Table 4.1 The relationship between shrinkage ratio (%) and NiO content**

| YSZ:NiO | Shrinkage(%) | Error bar (%) |
|---|---|---|
| 10:0 | 22 | 0 |
| 6:4 | 15 | 2 |
| 5:5 | 10 | 2 |
| 4:6 | 6 | 3 |

Furthermore, take the trade-off between shrinkage and electrical conductivity, the composition of YSZ-NiO anode is selected as 5:5. The shrinkage rate from the anode support is as high as 10%, which meets our expectation to be higher than the shrinkage of interconnect coating. In Fig4.13, the surface morphologies are totally different when coated on anode support with no shrinkage and with 10% shrinkage. Larger shrinkage rate from the anode support actually improves the sintering of coated layer by providing the forces towards the center. Both pure LSM and LSM:Ni coatings are of higher density on anode with 10% shrinkage.

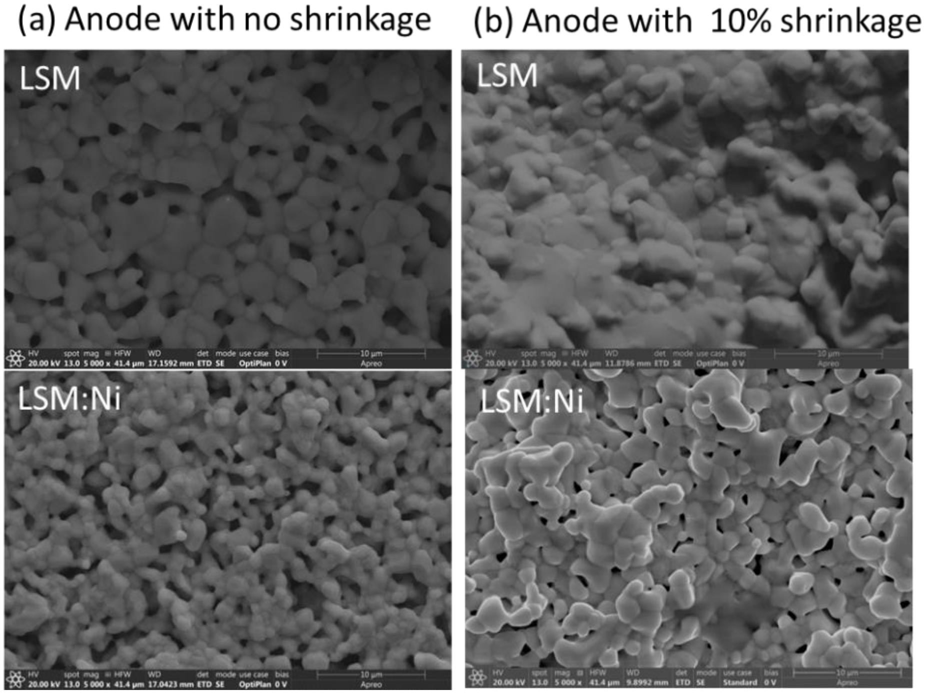

**Figure 4.13 The effect of MW-LSM and ss-LSM on the shrinkage and performance**

### 4.2.4 Chemical Stability by A/B Ratio Modification

During co-sintering process, second phase was found at the interface of interconnect and YSZ-NiO support. $La_2Zr_2O_7$ is quite resistive with an electrical conductivity around 2×10-4 S/cm,[23] which would lead to a severe degradation of the cells. A-site deficient LSM is reported to be less active with YSZ to form second phase than stoichiometric LSM. However, at the same time, A-site deficient might accelerate the diffusion of Mn toward anode side and lower the polaron concentration in LSM. Therefore, in this chapter, the molar ratio of (La,Sr)/Mn is fine-tuned to eliminate the second phase. In Fig.4.15, the XRD of single phase LSM with Mn excess is shown. Both the peak position and relatively intensity of (110) and (104) have changed. With B-site excess, the lattice parameter shortens from 5.509Å to (5.47±0.01)Å and the volume for single cell contracts. With (La,Sr)/Mn = 0.95, it is effectively tuned the A/B ratio of perovskite to be 1 after co-sintering in regards to the diffusion of Ni into YSZ-NiO and the possible reaction with Ni nanoparticles.

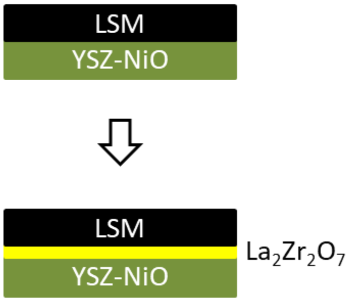

**Figure 4.14 Illustration of second phase formation during co-sintering**

Moreover, the stoichiometry can be examined by temperature-dependent resistivity measurement and grain growth shown in Figure 4.18. When A/B>1, the charge neutralization is balanced mainly by formation of $La^{3+}$ vacancies. However, at the same time, the oxygen vacancies might be formed as well, which trapped the polarons and increases the resistivity. When A/B<1, the precipitation or diffusion of Mn would have detrimental effect on electrical conductivity. Therefore, ideally, the resistivity is lowest when A/B is closest to 1. The surface morphologies and grain growth of LSM under different A/B ratio are presented in Fig4.18(b). It has been reported that slightly Mn excess introduces more La vacancies on the A-site in the pervoskite structure to neutralize the charge, which gives rise to the contraction of lattice as well as increases the $La^{3+}$ diffusion coefficient. The diffusion of $La^{3+}$ is the determining parameter for LSM grain growth. More A-site vacancies lower the barrier for $La^{3+}$ diffusing to the nearest sites and consequently, accelerate the grain growth. Similarly, too much Mn excess cause the Mn diffusion in YSZ-NiO anode, which leaves less Mn on B-sites in the perovskite crystals. The grain size meets a peak at A/B close to 1 and then declines.

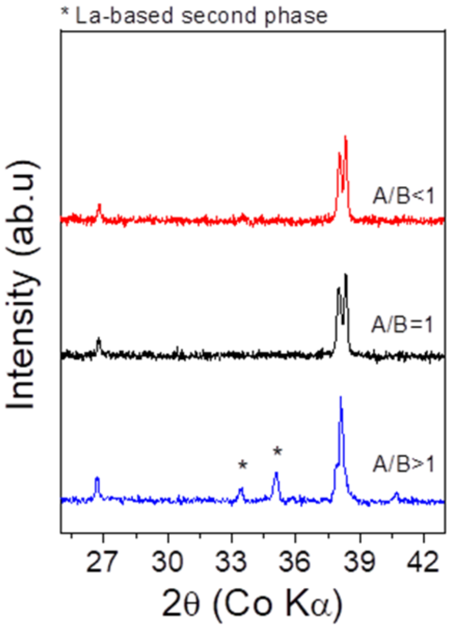

**Figure 4.15 Phase of (La,Sr)/MnO3 thick film on YSZ-NiO after co-sintering for: A/B>1, A/B=1 and A/B<1**

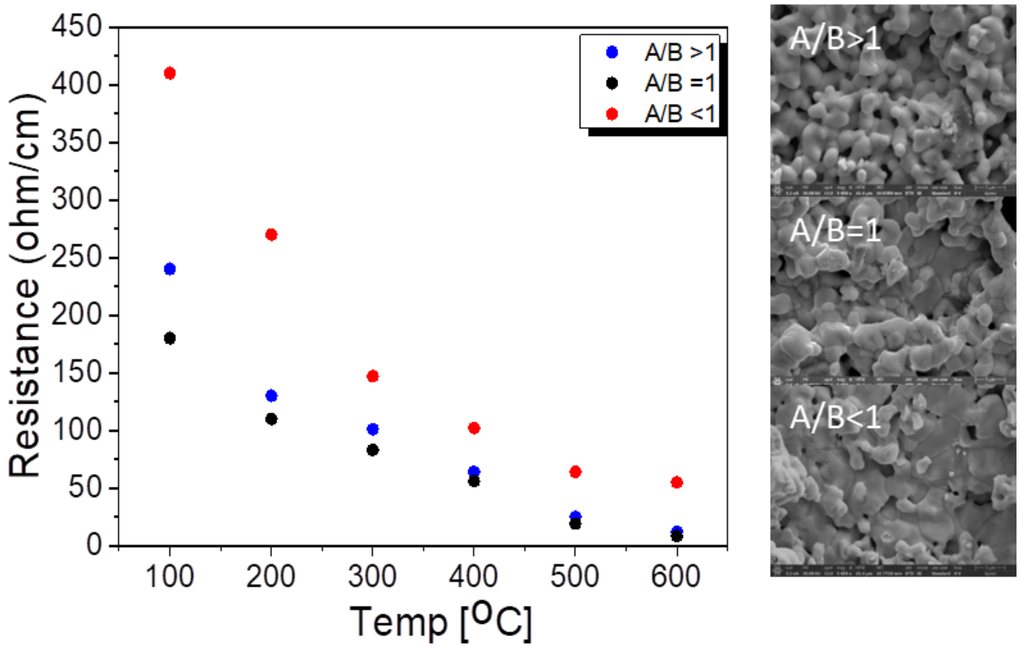

**Figure 4.16 Temperature-dependent resistivity and morphologies for different A/B**

EDS mapping was applied to examine the distribution of La and Mn element throughout the cross-section. In Fig.4.17 (a), the distribution of both La and Mn is not uniform. In regards to Mn diffusion into anode, residual La might have reaction with the water in environment and become La(OH)$_3$. The pervoskite structure is thereby decomposed. When Mn is excessed, this phenomenon has been suppressed. It's clear to tell the interface between LSM coating and anode support. However, too much Mn arise the new problem like significant Mn diffusion. As shown in Fig.4.17(c), the Mn diffuses to the depth larger than 100um. The intense diffusion of Mn might lead B-site vacancies so that part of Ni incorporates into pervoskite lattice, leaving less amount of Ni for percolation.

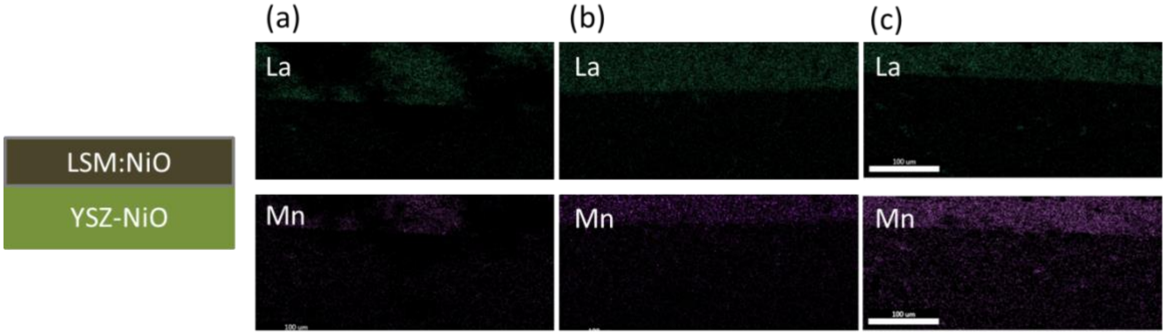

**Figure 4.17 Cross-section EDS mapping on La and Mn element for (a) (La,Mn)/Mn >1 ; (b) (La,Sr)/Mn =1; (c) (La,Sr)/Mn <1**

### 4.2.5 ASR Stability Measurement for Anode Support SOFCs

After fine-tuning on the composite of dual-layer interconnect and anode support to eliminate the interfacial reaction and thermal stress due to shrinkage mismatch. The LSM/LSM:Ni interconnect on anode support are fabricated and co-sintered at 1400$_{o}$C. As shown in Fig4.22, the thickness ratio is successfully controlled to be 1:2 or 2: 1 by tape casting. LSM:Ni layer, as discussed in previous chapter, hold better sinterability and more rapid grain growth rate. However, the design of dual-layer interconnect requests the LSM top layer to be dense too. As a result, thick top LSM layer is preferred to have higher coverage ratio and therefore has better sinterability. It is also noticed that LSM:Ni layer effectively block the diffusion of Mn in LSM top layer and therefore reserve the good conductivity and grain growth of LSM top layer in air.

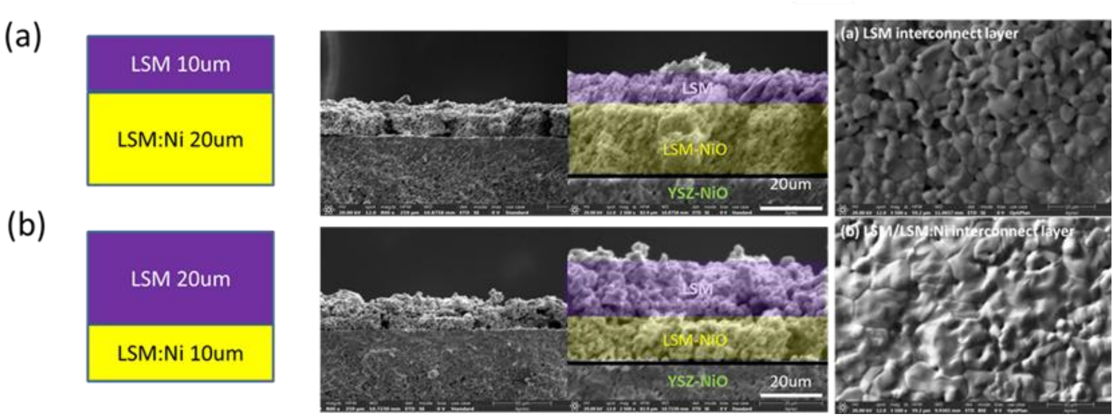

**Figure 4.18 Cross section and top view SEM images under different dual layer thickness for (a) LSM/LSM:Ni =1:2 and (b) LSM/LSM:Ni =2:1.**

The electrical properties were examined via coating Pt electrodes on the tio and bottom, shown in Fig4.23(a). To confirm the feasibility of LSM:Ni composite as interconnect for SOFCs, the long-term ASR measurement is set as shown in Figure.4.19(c). The LSM interconnect or LSM:LSM:Ni interconnect (Ni-100, 25%) is coated on YSZ-Ni anode support followed by co-sintering at 1400oC. Anode support after fully reducing would have a much lower resistance compared to the interconnect coating. Thereby, the contribution of anode to the ASR measurement is negligible. The overall LSM/LSM:Ni interconnect (thickness ratio = 2:1) ASR is lower in resistance than LSM with no obvious performance decay after new equilibrium. LSM:Ni layer turns to meet the percolation threshold and show metallic behavior in reducing ambiance. The resistance for LSM:Ni layer at operation temperature is negligible small. However, the high density of LSM:Ni layer block the gas flow and retard the formation of oxygen vacancies for LSM in air side. Moreover, it is possible that LSM:Ni dense layer eliminate the migration of Mn species from LSM top layer to the YSZ anode support. Thereby, the LSM electrical conductivity in air side maintains better.

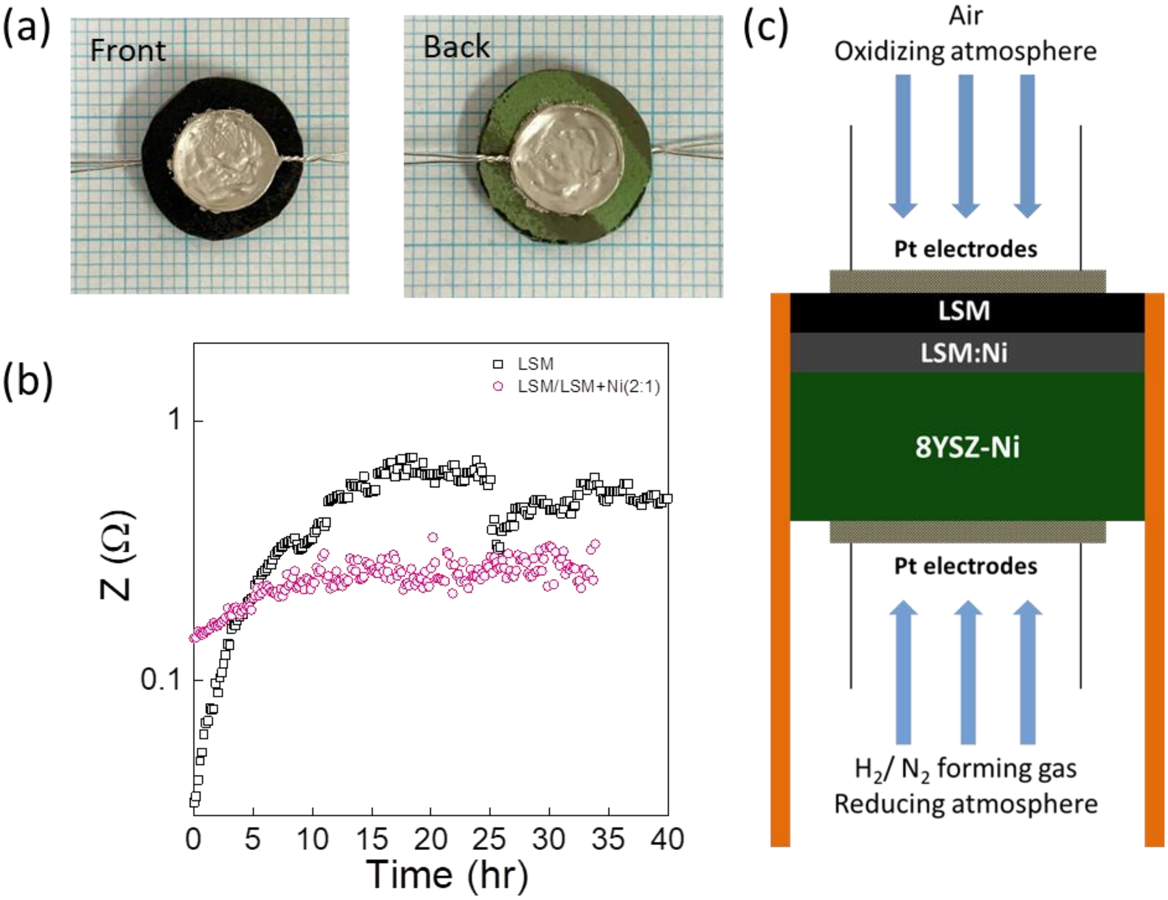

**Figure 4.19 (a) stability ASR measurement of LSM interconnect VS. LSM/LSM:Ni-100(25%) interconnect exposing to dual atmosphere at operation temperature 700$_o$C (b) Schematic of dual ambiance measurement setting.**

# 5.0 The Effect of Aspect Ratio of Ni Particles on LSM:Ni Composite

## 5.1 Background & Motivation

### 5.1.1 Motivation

It is well established that a significant enhancement of electrical properties occurs upon the addition on highly conductive filler materials to more resistive matrix materials. For instance, LSM:Ni composite, as discussed in previous chapter, is promising conductor in both oxidizing and reducing ambiance at high temperature. Percolation through the high conductive addition in oxide matrix, that is metallic particle, is given as the main mechanism of conduction in reducing ambiance. Free electrons transfer throughout the sample only if there is a continuous connection of metal addition from one end of the sample to the other. Metallic nanostructures presenting higher/lower aspect ratios may promote conduction at lower loading than spherical shaped additions. This chapter aims to lower the metallic percolation threshold by modification on the aspect ratio of metal, or in other words, the shape of metal.

The percolation of spherical particles has been widely investigated. Theoretically, the percolation threshold for spheres is around 0.34.[123] This value can be reduced effectively by either enlarging the aspect ratio of particle to 10, or decreasing it to 1/10. In this chapter, Ni percolation networks formed in LSM matrix by various shapes: nanoparticles (isotropic), nanoplates (2-D smashing) and nanowires (1-D elongation) are compared and discussed, aiming to reduce the Ni loading in the composites.

### 5.1.2 Percolation Threshold

Percolation threshold describes the transition in which isolated filler materials, such as metallic nanoparticles or carbon black, in matrix materials, turn in some sense to from connected channels. These channels play important roles on dramatic improvement on electrical properties or mechanical properties. For example, conductive carbon black particles are mixed with electrically insulating polymer.[124] The conductivity of the sample increases around 16 orders of magnitude after filler concentration exceeding percolation threshold, as shown in Figure 5.1. There are three regimes this conductivity transition. In the first regime, the conductivity is dominated by the matrix. In the second regime, when the concentration of metallic particles is adequate to form current flow network, a sharp increment in the conductivity is observed. In the third regime, multiple metallic channels are formed. Specimen shows more metallic behavior.

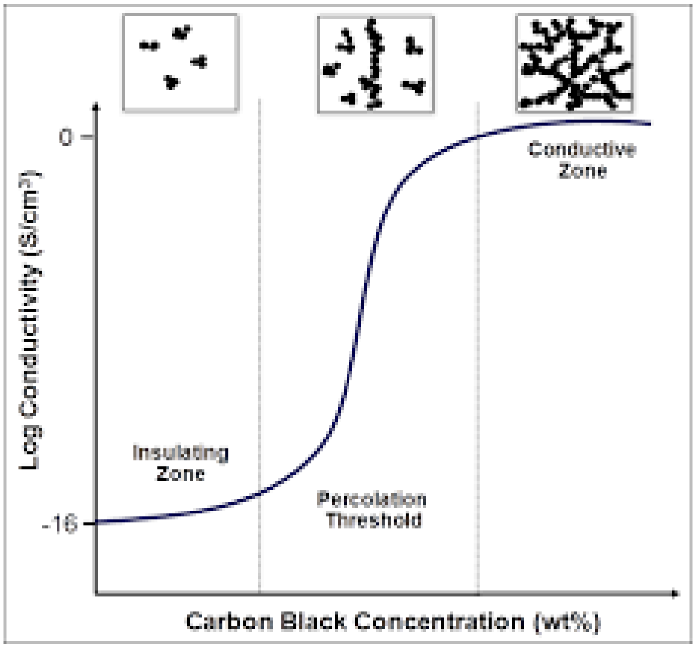

**Figure 5.1 S-shape curve of percolation threshold dependent conductivity** [124]

The percolation threshold strongly depends on the shape or say, the aspect ratio of additions. Mutiso et al.[125] and Balberg et al.[126] have reported the conductivity behavior as the function of both percolation threshold and the aspect ratio of additions, such as spheres, oblate spheroids or prolate spheroids using Monte Carlo model and random sequential addition (RSA). Although various model applied, the calculation results would be slightly different. But with increased anisotropy, the threshold is effectively reduced. Ambrosetti et all.[127] listed the relations of tunneling conductivity for randomly distributed additions with different shapes:

$$\text{Prolate spheroid: } \sigma \sim \sigma_0 \exp\left[-\frac{2D}{\varepsilon}\frac{\gamma(b/a)^2}{\varphi}\right] \tag{5-1}$$

$$\text{Oblate spheroid: } \sigma \sim \sigma_0 \exp\left\{-\frac{2D}{\varepsilon}\left[\frac{0.15(a/b)}{\varphi}\right]^{4/3}\right\} \tag{5-2}$$

$$\text{Sphere: } \sigma \sim \sigma_0 \exp\left[-\frac{2D}{\varepsilon}\frac{1.65(1-\varphi)^3}{12\varphi(2-\varphi)}\right] \tag{5-3}$$

Figure5.2. and Table5.1 show the calculation results based on the equation for sphere, oblate spheroids and prolate spheroids with different aspect ratio a/b = 1, ½, 2, 1/10, 10.  The aspect ratio should be 1/10 or 10 to make distinct reduction on percolation threshold.

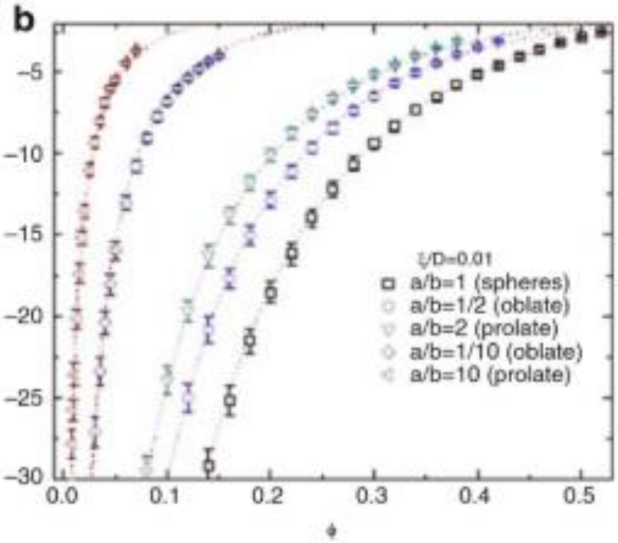

**Figure 5.2 Tunneling conductivity in a system of hard spheroids of different aspect ratios (Ambrosetti et al. [127])**

**Table 5.1Percolation threshold estimation for additions with different aspect ratio**

| | Sphere | Oblate spheroid | | Prolate spheroid | |
|---|---|---|---|---|---|
| | a = b =1 | a = 1/2b | a = 1/10b | a/b = 2 | a/b = 10 |
| Percolation threshold | 0.33 | 0.30 | 0.11 | 0.31 | 0.179 |

### 5.1.3 1-D Elongation via Polyol Method

The mechanism of metal nanowire growth along one direction has been widely owing to the unique electrical, optical and chemical properties of metal nanowire networks. [128-129] Among the synthesis method, polyol method is one of the most effective and economical ways to control the geometry of the metal nanostructures. In the synthesis process, metal salt is dissolved in a polyol solvent at certain temperature to form the precursors. Typically, ethylene glycol (EG) is selected as the solvent as well as reduction agent for the synthesis of Ag NWs. Poly(vinyl pyrrolidone) (PVP) works as the surfactant, also termed as capping agent to control the growth rate from different directions.[130] The Ag nucleates in the form of multiply twinned nanoparticles(MTP), holding a decahedron configuration coved with {111} facets to minimize the surface energy. The capping agent PVP has a carbonyl group and is proposed to stick on the {100} facets of Ag to block the radial growth. Hexadecylamine (HDA) and glucose are used as capping agent and reduction agent in water when synthesize Cu NWs.[9] The growth mechanism is similar to the one of Ag NWs.

For Ni nanowire synthesis, as published in the reports,[132] Nickel chloride is dissolved in ethylene glycol (EG) with certain amount of hydrazine hydrate, which can work as bridging ligand and reducing agent as well. Several complexes, such as $Ni(N_2H_4)_2Cl_2$, $Ni(N_2H_4)_4Cl_2$, $Ni(N_2H_4)_6Cl_2$ can be presented in the solution as precursors. After heating, excess hydrazine reduced nickel complexes into Ni nanoparticles holding chain-like structure due to homogeneous nucleation, following the reaction:

$$4[\mathrm{Ni(N_2H_4)_m}]^{2+} + 4\mathrm{nN_2H_4} \rightarrow 4\mathrm{Ni} + 4(\mathrm{m+n})\mathrm{NH_3} + 2(\mathrm{m+n})\mathrm{N_2} + (\mathrm{m+n})\mathrm{H_2} + 2(\mathrm{m+n})\mathrm{H^+}$$

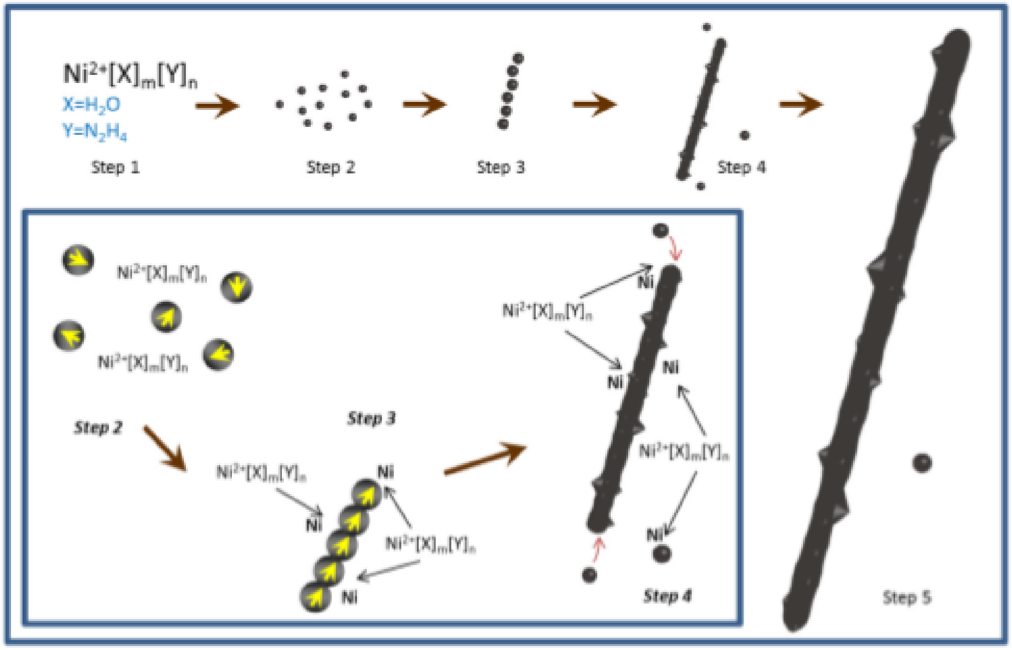

**Figure 5.3 Ni Nanowire growth mechanism** [132]

### 5.1.4 2-D Smashing via Ball Milling

Ball milling can provide high energy for the deformation of ductile materials and therefore a simply and cheap processing to change the shape of metallic addition in this study. Niraj et al. [133] has reported the evolution of morphology during high energy ball milling of Ni and Cu-Ni mixture. The morphologies of Ni particles changes from spheres to plate-like flakes after 10 hr milling. For longer milling time, the flakes undergo fragmentation and break into finer particles. Fig indicates that in plate-like flakes, {002} planes parallel to the surface and cause the intensity change between $I_{200}/I_{111}$.

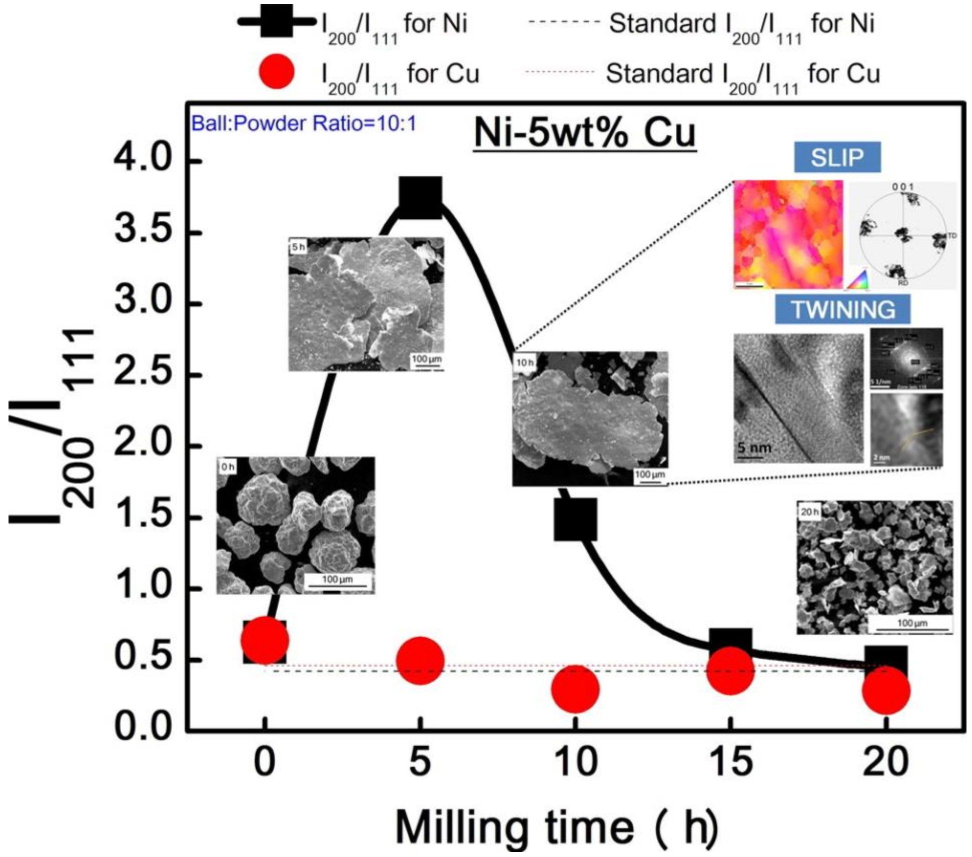

**Figure 5.4 The variation of I200/I111 ratio for pure Ni with milling time and the corresponding morphology of pure Ni powder with BPR = 4:1 at different milling time.** [133]

### 5.1.5 Oxidation and Reduction Kinetics of Ni/NiO

Transformation between Ni and NiO always undergoes the change in volume. In order to minimize the volume change of Ni-ceramic during oxidation/reduction process, it is essential to understand the oxidation and reduction kinetics of Ni, respectively.

*Oxidation mechanism*

During the oxidation process, usually, Ni has to diffusion outwards or $O_2$ inwards, comprising transport of holes and electrons. The oxidation kinetics can be described by several models depending on the rate-determining step under different conditions, like temperature or oxygen partial pressure.[12,18] It has also reported that it also affected by the defect concentration, size of the grains, preparation method and crystal orientation. [135,137,141]

Typically, almost all the kinetic models provide a prediction between oxidation rate, dx/dt as a function of thickness x. When the rate-determining step is surface reaction, the oxidation rate dx/dt is a constant. The thickness of oxidation layer is proportional to time t. On the other hand, when the rate-determining step is diffusion, the oxidation rate is inversely proportional to x, and $x^2$ is proportional to t.

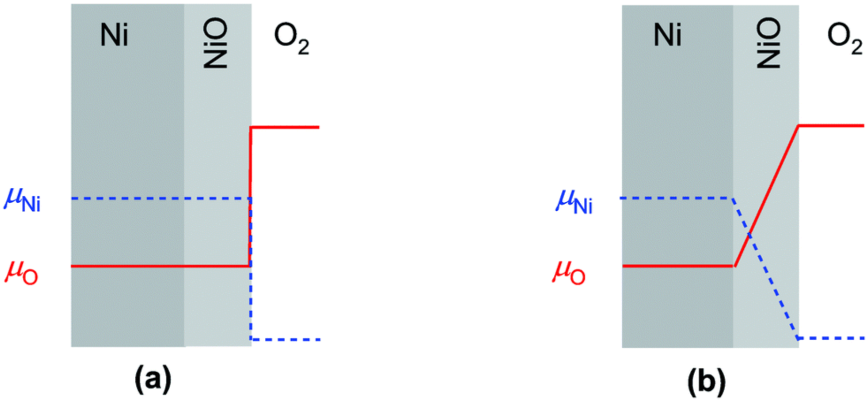

**Figure 5.5 The profile of the chemical potentials for (a) surface reaction-controlled oxidation and (b) chemical gradient-controlled oxidation.** [136]

As reported, NiO size is one of the critical parameters that affects the reduction process. Small NiO nanoparticle (< 30nm) has single reduction site. So that the reduced Ni particle is solid. But large nanoparticle ( ~100nm) has multiple reduction sites when being reduced in $H_2$ at 350°C, multiple reduction sites are found. Porous or hollow Ni with less volume change can be obtained.

In addition, reducing temperature is another factor of importance. The generally proposed mechanisms for NiO reduction kinetics can be categorized into two models, the Avrami-Erofeev model and the D1 model. [137,138,147]

At low temperature (T < $500^{o}$C), the reduction is predominant by the nth order Avrami-Erofeev (AEn) model: [137]

$$\alpha_{NiO} = 1 - \exp\left(-k_0 \exp\left(-\frac{E_a}{RT}\right) t^n\right) \qquad (5\text{-}4)$$

where kinetics is corresponding the growth dimension and the exponent n can be 0.5~4. However, if the kinetics is limited to diffusion, then the exponent n equals to 1 and the equation goes into the D1 model: [138]

$$\alpha_{NiO} = \left(k_0 \exp\left(-\frac{E_a}{RT}\right) t\right)^{0.5} \qquad (5\text{-}5)$$

High temperature (>$500^{o}$C) reduction reaction is usually associated both AE model and D1 model.

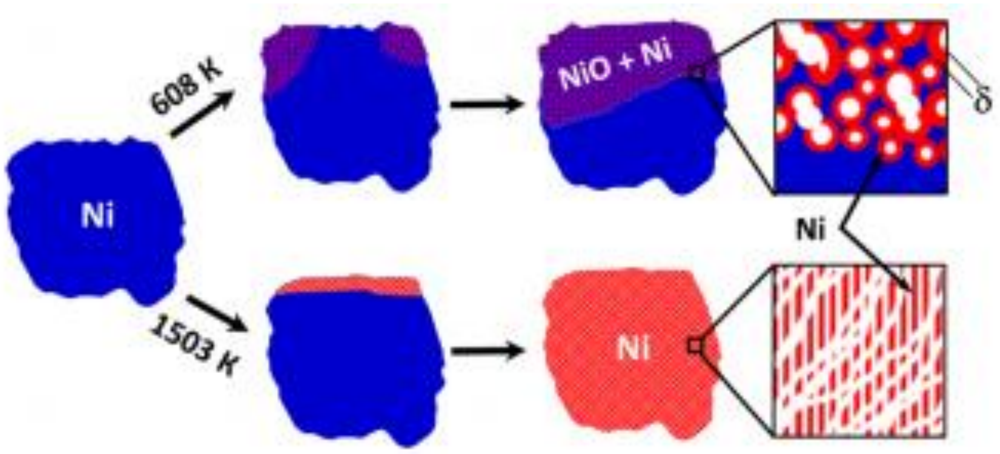

**Figure 5.6 Schematic illustration of NiO → Ni followed by different model under high/low temperature** 139

The schematic illustration of NiO reduction under 608K, when growth mechanism is dominant, and under 1503K, when both diffusion and growth mechanisms are rate controlling step, is showed in Figure 5.6. Accordingly, the microstructures after reducing in these two temperatures are very different. This indicates that high temperature is needed to take both diffusion and growth of Ni into consideration to avoid the formation of large pores.

## 5.2 Ni Shape Effect on LSM:Ni Composite

### 5.2.1 Sample preparation

**Ni Nanostructure:** Ni nanoparticle was purchased from Sigma-Aldrich. Ni nanoplate was physically deformed from Ni nanoparticle via directly ball milling with Zirconia balls in ethanol for 48hr and 72hr until the shape of Ni squeezed into Ni plates with an average diameter 1.5um and 3um, respectively. Ni nanowire was synthesized followed a wet chemical reduction method [13]. Ni Chloride ($NiCl_2$) solution was added into 15mL Ethylene Glycol (EG) to form a solution with concentration 5mM. The precursor was then heated to $90_oC$ to get a transparent green solution. 0.5mL $N_2H_4.H_2O$ was generally added in the hot precursor, dropwise. The color of solution turned into dark gray and Ni nanowires were eventually floated on the surface. The product was then collected by a magnet and washed by DI water and anhydrate ethanol for several times.

**$La_{0.8}Sr_{0.2}MnO_3$ Ceramic:** LSM powder was synthesized by the traditional solid-state method. The starting metallic salts used were Lanthanum(III) oxide (>99.9%, Sigma Aldrich), Strontium carbonates (>99.9%, Sigma Aldrich) and Manganese oxides oxidized from Manganese(II) carbonates (>99.9%, Sigma Aldrich). Materials under proper stoichiometric ratio were carefully weighed and ball milled in ethanol till complete homogeneity. The obtained powder was then treated in air at $1100_oC$ for 20hr to get a single phase LSM powder. The LSM powder (or LSM:Ni mixture) was pressed into a green body with 10mm in diameter under pressure around 4tons/inch, followed by a sintering at $1400_oC$ for further characterizations.

### 5.2.2 Characterization and Measurement

**Characterization:** The crystal structure and phase stability were examined by X-ray diffraction (XRD, Co Kα) in a range of $2\theta = 20\text{-}80_o$ at a step size of $0.03_o$ and step rate of 0.4s.The morphology and element distribution were characterized by scanning electron microscopy (SEM, Apereo) equipped with an energy dispersive spectroscopy (EDS). The resistance vs. temperature measurement was accomplished by Keithley digital meter. Air and forming gas ($H_2/N_2$=5%) were applied as the oxidizing and reducing ambiance.

*Scanning Electron Microscopy/Energy Dispersive X-ray Spectroscopy (SEM/EDS)*

Energy dispersive x-ray spectroscopy (EDS), also referred as EDX or EDAX, is a powerful method to get quantitative elemental information on specific areas. The mechanism can be explained as: the incident beams stimulate an electron in inner shell of an element, ejecting it from the shell. Meanwhile, the electron from outer shell would elapse and fill the hole left in inner shell. The energy difference is then released from the specimen in the form of x-ray and can be detected to identify the element. In this study, EDS mapping is widely used to locate the position of Ni and to monitor the diffusion of elements, such as La, Sr, Mn and O.

### 5.2.3 Result and Discussion

The aspect ratio of Ni addition is effectively changed via either 2-D squashing or 1-D elongation. As discussed previously, when aspect ratio =1, the shape of addition is spherical, percolation threshold reaches its maximum value over 0.33. According to the computational calculation, it can be stated that the percolation threshold won't decrease effectively when the aspect ratio change sfrom 1 to 3. However, if the aspect ratio is more than10 or less than 1/10, the theoretical percolation threshold can drop to 1/3 of its original value. As shown in the Figure 5.7, mechanical deformation is a feasible approach to decrease the aspect ratio. Longer milling time, the lower the aspect ratio. On the contrary, in order to increase the aspect ratio, nanowires are synthesized using polyol method. The nucleation rate and reaction temperature has been proven remarkably effective to increase the aspect ratio.

**Table *5.2* Aspect ratio of nano plates after ball milling**

| | **Diameter (2a, 2c)** | **Height(2b)** | **Aspect ratio (b/a)** |
|---|---|---|---|
| (a) | 800 | 800 | 1 |
| (b) | 1000 | 300 | 3.33 |
| (c) | 3000 | 200 | 15 |

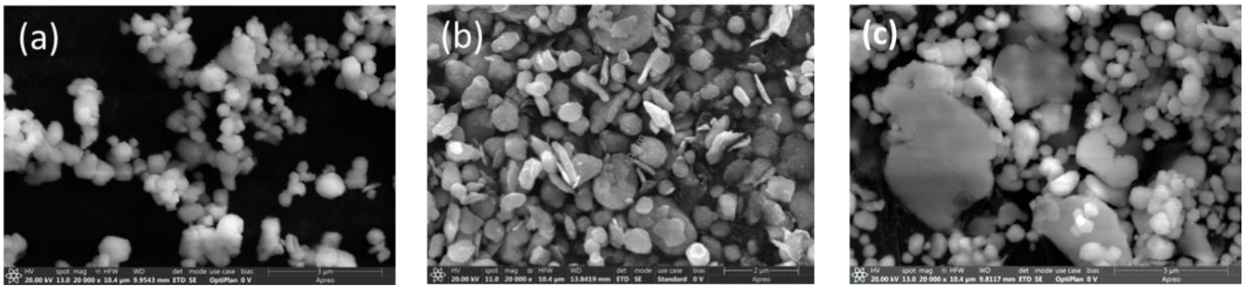

**Figure 5.7 Morphology change under ball milling time**

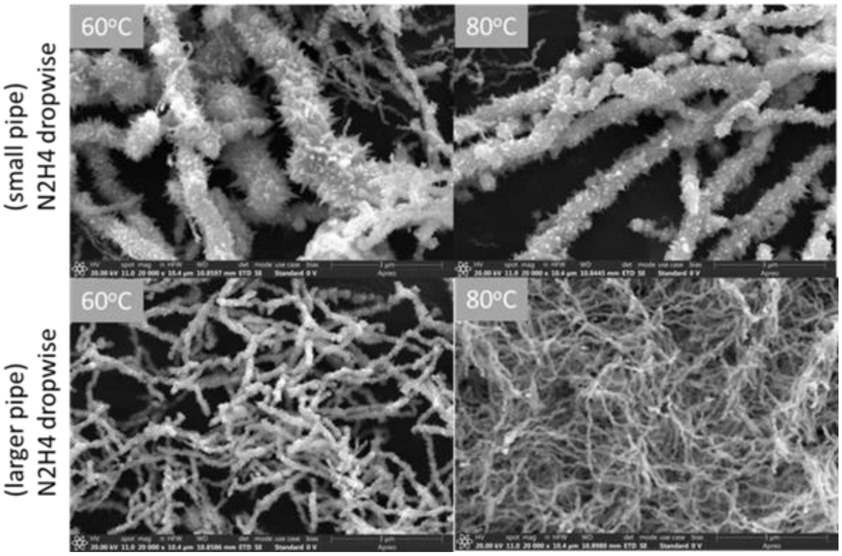

**Figure 5.8 Controlling of aspect ratio of Ni plates and Ni wires**

In order to get high electrical conductivity with low Ni loading, 1-D elongation into wire with high aspect ratio > 10 or by 2-D squashing into oblate spheroid with low aspect ratio < 1/10 are applied to meet the requirements. Morphology of as-synthesized Ni spheres (a/b = 1), Ni plates (a/b = 1/10) and Ni wires (a/b = 10) before calcination characterized by SEM and XRD, shown in Figure 5.9. Ni spherical particles (a/b =1) have an average size of approximately 500 ± 400 nm. Ni plates (a/b = 1/10) prepared via mechanical ball milling are as thin as 300 nm and reach ~3um of micrometers in diameter, shown in Figure 5.9(b). Ni wires (a/b = 10) synthesized using polyol method, are uniform in size as shown in Figure 5.9(c). They have diameter of D = 300nm, and length of L = 3000nm.  Figure 5.9(d) presents the XRD phase identification on Ni(111) and Ni(200) planes. The peak intensity ratio $I_{200}/I_{111}$ and $I_{111}/I_{200}$ have been calculated and listed. For Ni plates, $I_{200}/I_{111}$ increases from 0.46 to 0.567. As Niraj et al.[11] reported, plate-like flakes can be prepared via high energy mechanical milling via deformation on (002) planes parallel to the surface, which causes the intensity changes between $I_{200}/I_{111}$. For Ni wires, as reported by Tang et al.[10], the intensity increment of $I_{111}$ might be explained that the Ni seeds link head to tail by magnetic dipole attraction with the presence of abundant surfactant PVP. In sum, by adjusting the aspect ratio of Ni additions, anisotropy, surface area and the growth on Ni(111) and Ni(200) have been changed.

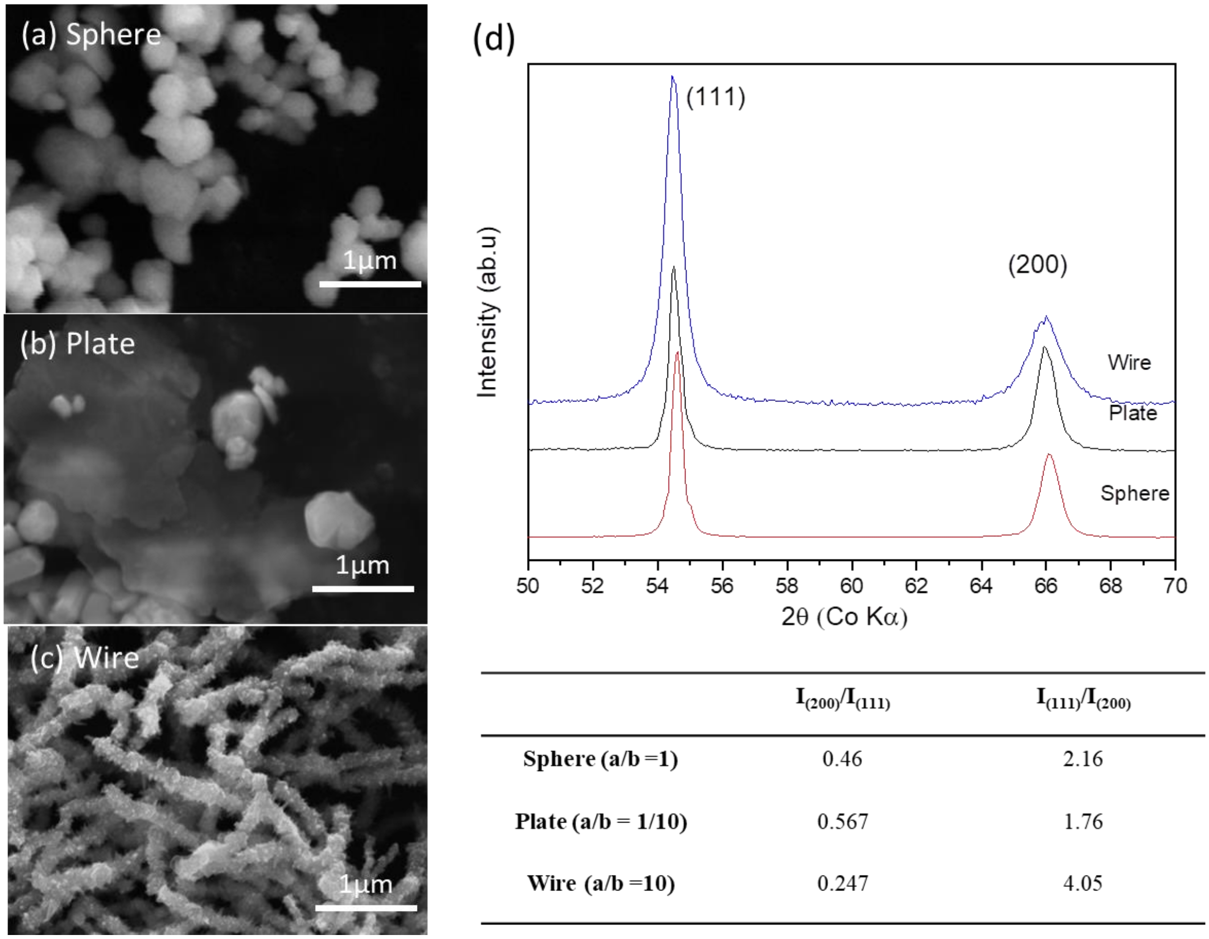

| | $I_{(200)}/I_{(111)}$ | $I_{(111)}/I_{(200)}$ |
|---|---|---|
| **Sphere (a/b =1)** | 0.46 | 2.16 |
| **Plate (a/b = 1/10)** | 0.567 | 1.76 |
| **Wire (a/b =10)** | 0.247 | 4.05 |

**Figure 5.9 nanostructure morphologies for: (a) sphere; (b) plate; (c) wire; (d) XRD phase identification on Ni(111) and Ni(200) planes and corresponding intensity ratio I200/I111 and I111/I200 calculation.**

The oxidation analysis of LSM:Ni composite green body was performed through a combination of morphology and phase changes under three temperature, room temperature, $450_{o}$C and $800_{o}$C using SEM and XRD, respectively. Before heat treatment, Ni(111) and Ni(002) could be indexed as single-phase Ni for all the samples, spheres (a/b=1), plates (a/b=1/10) and wires (a/b=10). It was observed that with increasing oxidation temperature there were an associated increased NiO peaks and decreased Ni peaks, indicating that the Ni had gradually fully oxidized into NiO. Eventually, at 800$_o$C, only NiO peaks can be found with undetectable Ni peaks from the XRD patterns for all the samples. Thereby, the oxidation rate difference caused by aspect ratio is negligible during sintering process, when the sintering temperature is 1400$_o$C.

At low temperature, 450$_o$C, it has been demonstrated that Ni oxidation presents a sub-parabolic behavior. This phenomenon indicates that the rate-determining step is a combination of surface reaction and chemical gradient, when the oxygen dissolution rate is competitive to NiO formation rate. Ni plates and spheres have slow oxidation at this temperature. The XRD patterns show a mixture of Ni and NiO. Furthermore, the presence of some oxides, namely reactive elements, including $La_2O_3$ ,[20] $Y_2O_3$,[21] $CeO_2$ , [144] has been investigated to affect the oxidation of Ni as well. Say, these reactive elements may segregate to the grain boundaries of Ni in the form of either oxide nanoparticles or ions, to decline the outward diffusion. Consequently, the overall oxidation rate may decrease dramatically, with a change in one or two orders of magnitude. The resultant sample maintains lower stresses that are easily released via the plastic deformation with fine NiO grains. Cohension between the oxides may be improved, which hinders the generation of inter-granular cracks.[145] Ni plates and spheres, with better mixing and packing, contact better with LSM grains. In this regard, the oxidation rate is much slower than the one of Ni wires. Both dimensional disadvantage (d = 300nm) and poor mixing and packing might attribute to the rapid oxidation od Ni wires.

Slow oxidation rate is also beneficial to the morphology of the composite. In Figure 5.10 (b), The morphologies evolution of LSM:Ni mixture at 25$_o$C, 450$_o$C and 800$_o$C, with different Ni aspect ratio are presented and compared. Ni additions were almost reserved in shape among the LSM particles for all spheres, plates and wires up to 800$_o$C. High anisotropy of Ni wire reduced the homogeneity of mixing and packing. It is challenging for LSM particles to fill the gaps among Ni wires.

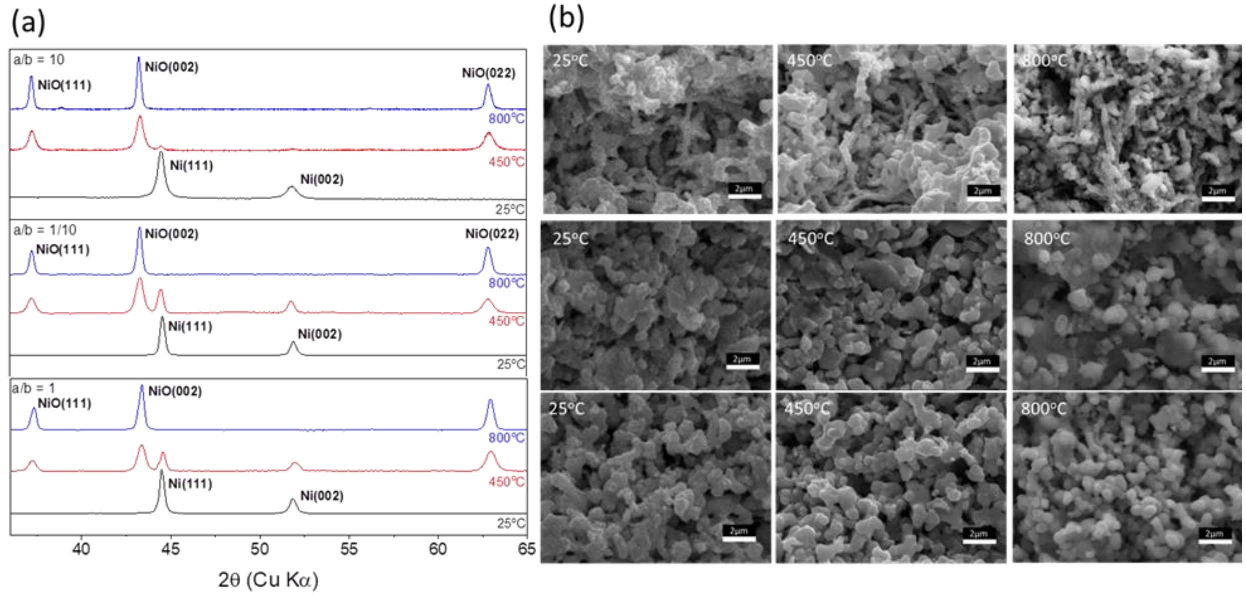

**Figure 5.10 (a) Ni oxidation phase changes and (b) LSM:Ni green body morphology evolution after heat treatment at 25$_o$C, 450$_o$C and 800$_o$C for Ni with different aspect ratio**

Figure.5.11 presents XRD patterns of LSM:Ni composites with different Ni shapes after sintering at 1400$_o$C with Ni= 10, 20 and 30wt.%. All the diffraction peaks can be well indexed as Face-center cubic nickel oxide (JCPDS 98-004-9032) and (La,Sr)$MnO_3$ (JCPDS 98-010-7562). There was no second phase found in all the composites, which indicates that all the NiO was maintained without reaction with LSM after high temperature sintering. Furthermore, all the samples showed typical NiO peaks at $2\theta = 43.5_o$, $50.7_o$ and $74.5_o$ (Co Kα), corresponding (111), (200) and (220) crystalline planes of an FCC crystal structure, respectively.

Figure 5.12 shows the EDAX Ni distribution throughout the LSM:Ni composite. The distribution of Ni element was more straight-forwarding and more insightful for Ni path percolation. Clearly, the distributions of Ni are various with different Ni shapes. The plates have preference on orientation after pressing according to Figure 5.12. The aligned Ni plates boost the linkage. Thereby, the percolation is expected to smaller. It can be observed that Ni wire connected and formed a network. The localization of Ni wires is noticeable. The coverage of Ni wires is low in regards to their limited diameter. Actually, both Ni plates and Ni wires might not be lightened in the EDAX due to their thin thickness and small diameter around 300nm

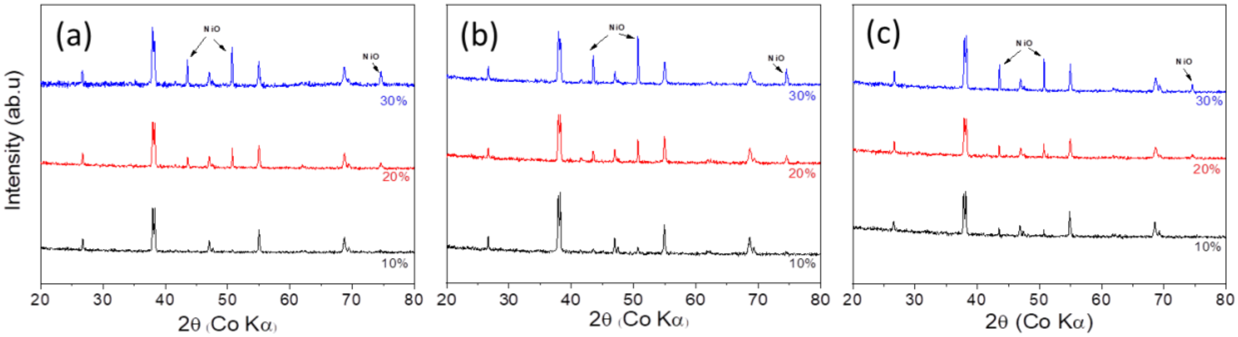

**Figure 5.11 XRD phase pattern of sintered pellets prepared with different shape of Ni inclusions: a) Ni Spheres; b) Ni Plates; c) Ni Wires**

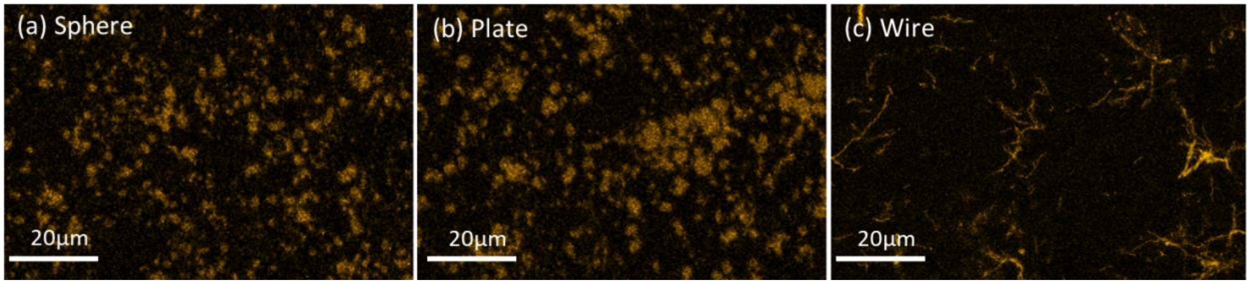

**Figure 5.12 EDAX Ni distribution in LSM:Ni composite after heat treatment at 800$_o$C**

Figure5.13 is the SEM micrograph of the LSM:Ni composite prepared under different Ni aspect ratio as well as Ni content. It can be seen from Fig.4a, b or c that the grain size decreases with Ni content no matter what aspect ratio of Ni nanostructures were used. Ni serves as sintering inhibitor, which increase the sintering temperature and retard the sintering process. Actually, increased Ni surface area would block the growth of LSM and result in the decrease of grain size. Therefore, we were seeking to reduce the amount of Ni in the LSM:Ni composites by changing the shape of Ni. However, Ni and LSM grains enable to form a continuous network due to their similar sinterability. This explains that when Ni =10wt.%, Ni spheres with high isotropy, from Figure 5.13a, arrange well in the LSM matrix with limit pores. In Figure5.14 the shrinkage rate and average grain size for the LSM:Ni composite prepared under different Ni aspect ratio as well as Ni content are plotted and compared. Higher anisotropy of Ni microstructure leads to smaller grains in size after sintering. Moreover, the orientation-dependent oxidation rate of Ni and the sinterability of NiO itself would change the sintering behavior as well. With increment of $I_{111}$, the oxidation rate of Ni drops. As shown in Fig.2b, the rapid oxidation along (200) planes and the Ni plate alignment leads to the linkage and necking of Ni plates at 800$_o$C. Relatively rapid oxidation rate might explain the higher shrinkage rate and higher density for Ni plates composite. The grain size change with Ni amount for Ni wires samples is minimal. The densification for Ni wire samples is localized due to the low oxidation ratio for (111) planes and worse mixing between LSM powders and Ni wires, leaving the traces of wires as cracks and fractures after sintering at high temperature.

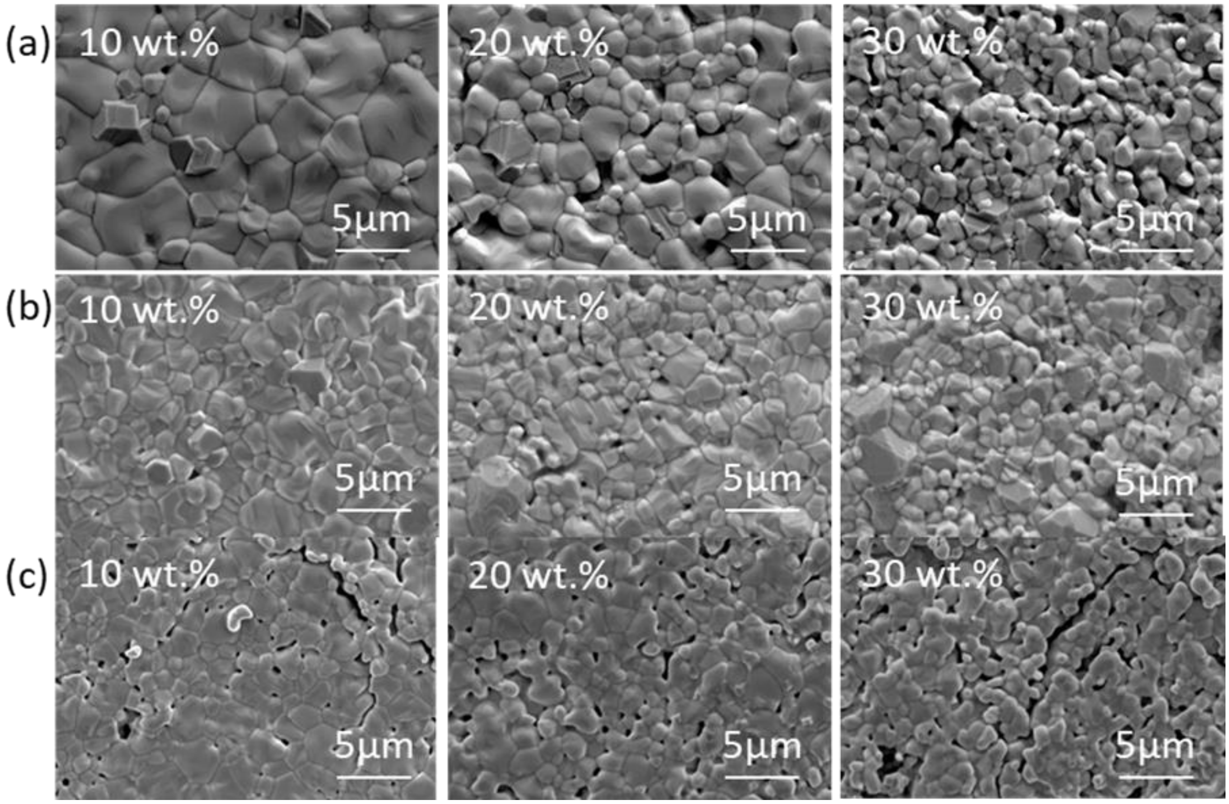

**Figure 5.13 SEM images of sintered LSM:Ni composite prepared with Ni = 10, 20, 30wt.% for: (a) Spheres; (b)Plates; (c) Wires**

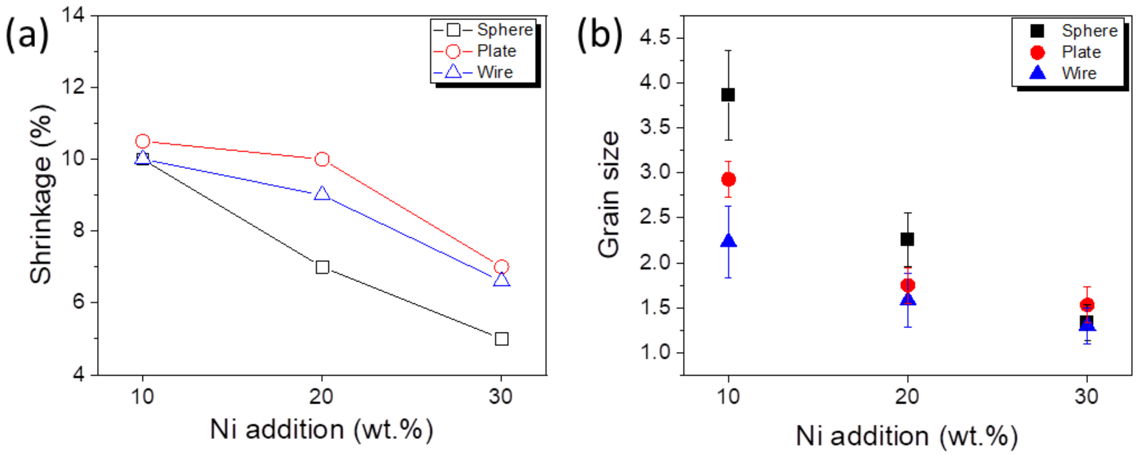

**Figure 5.14 Shrinkage (%) and Average grain size(um) after sintering at 1400oC**

In this study, the LSM:Ni composites followed two different conducting mechanisms in air and in reducing ambiance, the metallic free electrons mechanism and the small polaron hopping mechanism. The relationship between Resistance and temperature were presented in Figure5.15. In Figure5.15a, the solid dotted lines represented the resistance in air. At high temperature, the conduction was mainly dominated by LSM polaron hopping mechanism, meanwhile most Ni was maintained in the oxidized status. According to small polaron hopping theory, the Resistance changes linearly versus the reciprocal absolute temperature: 146

$$\ln(\rho/T)=\ln A+(W_H/2k_BT) \tag{5-6}$$

where A is a pre-exponential constant; T the absolute temperature; $W_H$ the activation energy; and $k_B$ the Boltzmann's constant. For all the samples, the slope value drops with Ni amount, which also meets our observation in the sintering behavior. High density suppresses the formation of pores and guarantees the hopping of small polarons. In the reducing atmosphere, $H_2/N_2$=5%, oxygen vacancies were formed on the grain boundaries of LSM and trapped the polarons. The activation energy becomes higher, which leads to the increment of slope if LSM maintain as the major conduction materials for composite. On the other hand, in reducing atmosphere, Ni percolating paths hold much lower resistivity and thereby become predominant conducting materials. The resistivity after meeting percolation threshold no longer followed the small polaron hopping mechanism. So, ln(ρ/T) and 1/T does not obey the linear relation anymore. The hollow dotted lines showed in Fig.6a represented the resistance measured in $H_2/N_2$%=5% after total reduction of NiO into Ni. The slope for LSM:Ni with Ni as dominating conductive materials decreases in forming gas than the one in air.

According to the assumption in this study, pellets would behave more like metals than semiconductors, the relationship between log (R/T) VS. 1/T is no longer linear. Therefore, log(R) VS. T was plotted in Figure5.15b. Electrons were freely moved throughout the pellet, which boosted the electrical conductivity significantly. From Figure5.15b, Ni spheres did not meet percolation threshold until 30wt.%. Ni plates and Ni Wires had the percolation threshold around 10% to 20%. Also, when the Ni percolation threshold was reached, the slope drops dramatically to close to zero. This abnormal change in the slope indicates the sudden change in the resistance of composite.

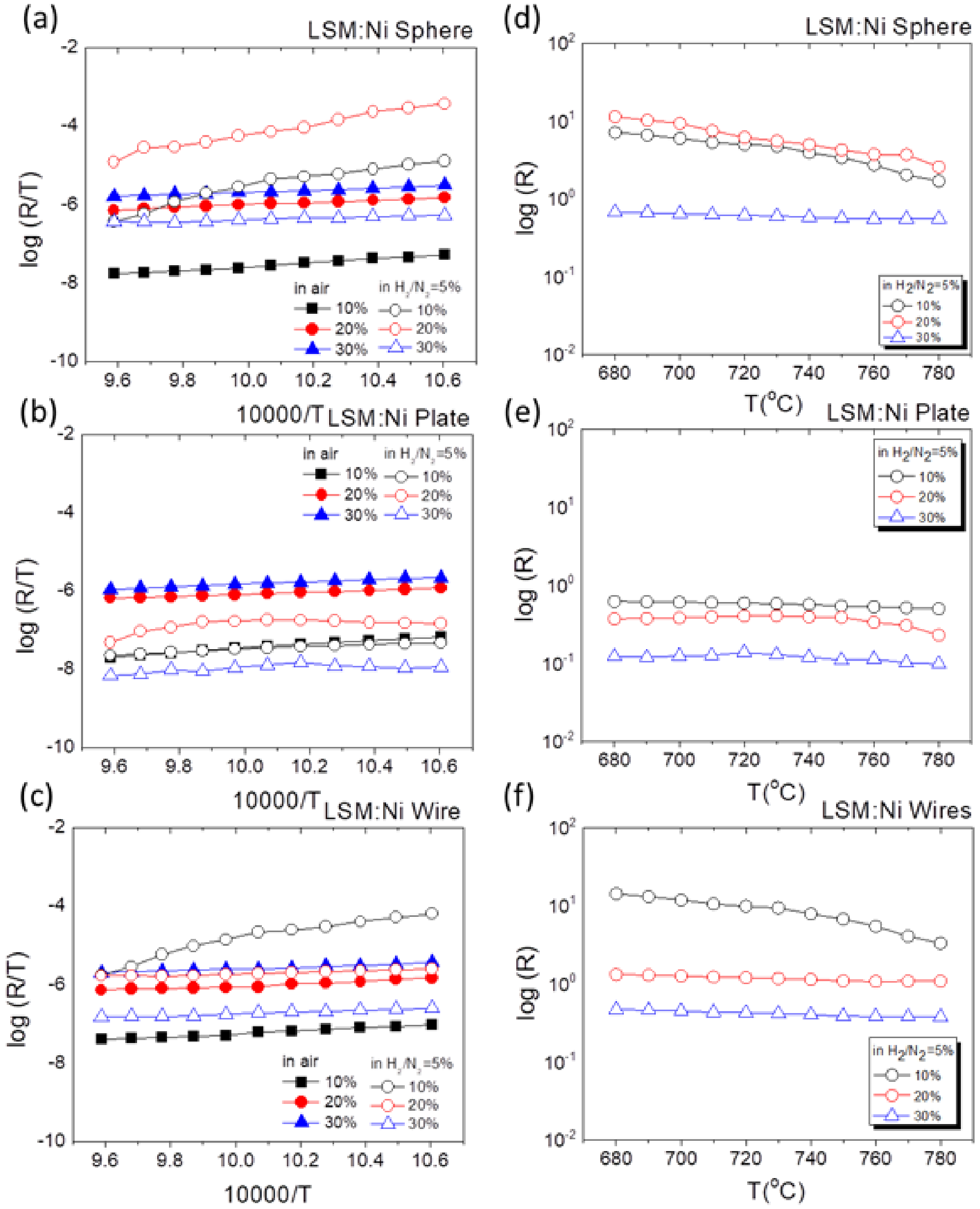

**Figure 5.15 log(R/T) VS. 1/T in air and in (H2/N2 = 5%) for (a) Ni sphere; (b) Ni plates; (c) Ni wire; Log(R) VS. T in in (H2/N2 = 5%) for (d) Ni sphere; (e) Ni plates; (f) Ni wires**

# 6.0 The Effect of Aspect Ratio of Silver Nanowires on ZnO/Ag Composite

## 6.1 Motivation & Background

When aspect ratio keeps increasing to 100 -~1000, the metallic addition provides not only a conductive phase to be introduced in the oxide matrix, it also promotes the conduction at very low loading than spheres or other shaped addition with low aspect ratio. Furthermore, metallic addition with high aspect ratio is also beneficial to the optical transparency. Despite the existence of numerous publications in regard to metal nanowires/ oxide composite materials as transparent and conductive films (TCs), reports aiming to explain the mechanisms that how resistance at junctions of wire can be changed by the oxides are scarce. It's well established that the high conductivity in the metal nanowire/oxide composite TCs is related to both the percolation of wires and the tunneling effect that allows for the electrons to transfer from one wire to the neighboring one via semiconducting oxide. It has been reported that films fabricated from Ag NWs synthesized by polyol method are non-conductive without treatment due to highly resistive junctions covered by insulting polymers. Different processing technologies, such as thermal annealing, [148-149] plasmonic welding,[150] and mechanical processing [151] have been discussed to modify the resistance of junctions. Hu et al. reported that the resistance of junction ($R_j$) can be as high as ~$1\times10^4\Omega$.[152] Other groups tried to fit the calculated $R_j$ with experiments, and got $R_j$ is close to ~$2\times10^3\Omega$. [153] Nian et al. obtained $R_j \sim 450\Omega$ measured by four point probes. [154]

Detailed studies based on experiments and computational calculation of the impact of aspect ratio of Ag NWs and ZnO on the junction resisttance of silver nanowires (Ag NWs) in the AgNWs/ZnO composite and the potential of our composite as TCs in environments with high temperature or humidity are presented in this chapter. In addition, the nanoparticle decoration method has been proposed to be an effective approach to reduce the Hazeness of TCs.

### 6.1.1 Transparent and Conductive Films (TCs)

TCs are of increasing interest in photo-electronic fields, such as solar cells, touch panels and organic light emitting devices (OLEDs), due to its potential to be both optically transparent and electrically conductive. [155-158]

Semiconductors with wide bandgap, such as ZnO, CdO, $SnO_2$ and $In_2O_3$, [159] are featured to have low absorption in the visible light range. Among a variety of semiconductors, indium oxide with tin doping (ITO) is most widely used as TCs with a low sheet resistance, 10 ohm/sq and a high transmittance above 80 % at 550 nm. The transparency and sheet resistance values also become the standard requirement for evaluation of TCs. However, pure semiconductors face several problems: (1) Even with dopant, the conductivity of semiconductor is still several orders of magnitude lower than the metals. (2) Furthermore, the consumption of rare metal indium is another problem. In the past decade, the world production of indium metal has risen from 300 to 700 tons/year.[160] (3) Also, the mechanical properties for pure semiconductors are too brittle. For modern application design, curved or flexible electrodes are expected.

Low-dimensional Ag NW networks are considered to possess high potential in replacing ITOs due to their favorable transparency and good stability. Basically, several characteristics, including coverage ratio, aspect ratio and junction resistance govern the physical properties of Ag NW-based composites. The role of coverage ratio is one of the most important parameters. As the Figure of Merit (FOM) of TCEs, a trade-off between optical transparency and sheet resistance should be compromised to optimize the performance. When coverage ratio exceeds the percolation threshold too much, silver networks tend to absorb light with selected wavelength; while a very low coverage ratio gives rise to loss of conductivity. Beyond the coverage ratio of Ag NWs, the dimension of nanowires also plays a vital role on the conduction. The longer a single Ag NWs is, the less junctions that needed to be passed to form electrical channel, which leads to a lower sheet resistance for networks with longer nanowires. Besides the number of junctions, the resistance of junctions between two Ag NWs also plays a crucial role.  Although Ag NW itself possesses excellent conductivity, the overall sheet resistance of Ag NWs might be lower in orders of magnitude due to large resistance between two Ag NWs. It has been reported that the junction resistance can reach as high as 1GΩ to couples of hundreds ohm when polymer dispersive agents, like poly(vinyl pyrrolidone) (PVP), are covered at the surface of Ag NWs. 161-163 To improve the performance efficiency of Ag NW networks, extensive techniques have been investigated. Tukono et al. used cold pressing method to weld the network under 25MPa. The resultant product showed a good sheet resistance 8.6Ω/sq. and very low surface roughness. But the transmittance is around 80%. Gannet et al. applied light-induced plasmonic welding technique to improve the joint of nanowires. The product exhibited a resistance around 10 Ω/sq at a transmittance around 80%. The junction resistance was claimed to be comparable to the Ag NW resistance. Lee et.al demonstrated that simply solvent washing was effective to remove the PVP and enhance the contact between nanowires. The Ag NW networks showed 18.9Ω/sq a transmittance higher than 90%.

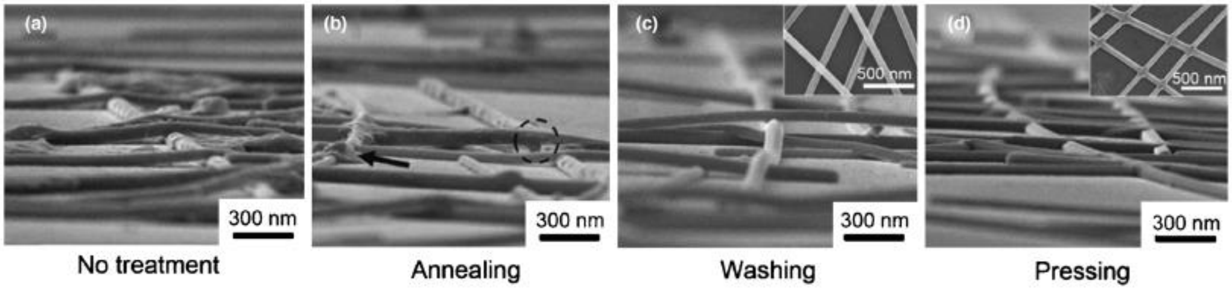

**Figure 6.1 Ag NW networks with different post processing to reduce the junction resistance: (a) no treatment; (b) annealing; (c) washing; (d) pressing.**[16]

These problems forced the researches to search for rare-metal-free, eco-friendly metal/oxide composite TCs that can combine both metallic and ceramic advantages.

### 6.1.2 Percolation Threshold of Nanowires

As discussed previously, there is a significant impact of the dimensions of the metallic addition on the electrical conductivity of composite. The aspect ratio of nanowires, representative of the ratio of length to diameter, is rational to not only the electrical properties but also to the optical properties. To understand the role of this dimensional change, two S-shaped percolation curves, comparing spheres to wires, are shown in the Figure 6.2. With great aspect ratio, the probability of connections between metal and metal is promoted with the result that the isolating-conductive transition is reached with much lower loading with one or two orders of magnitude.

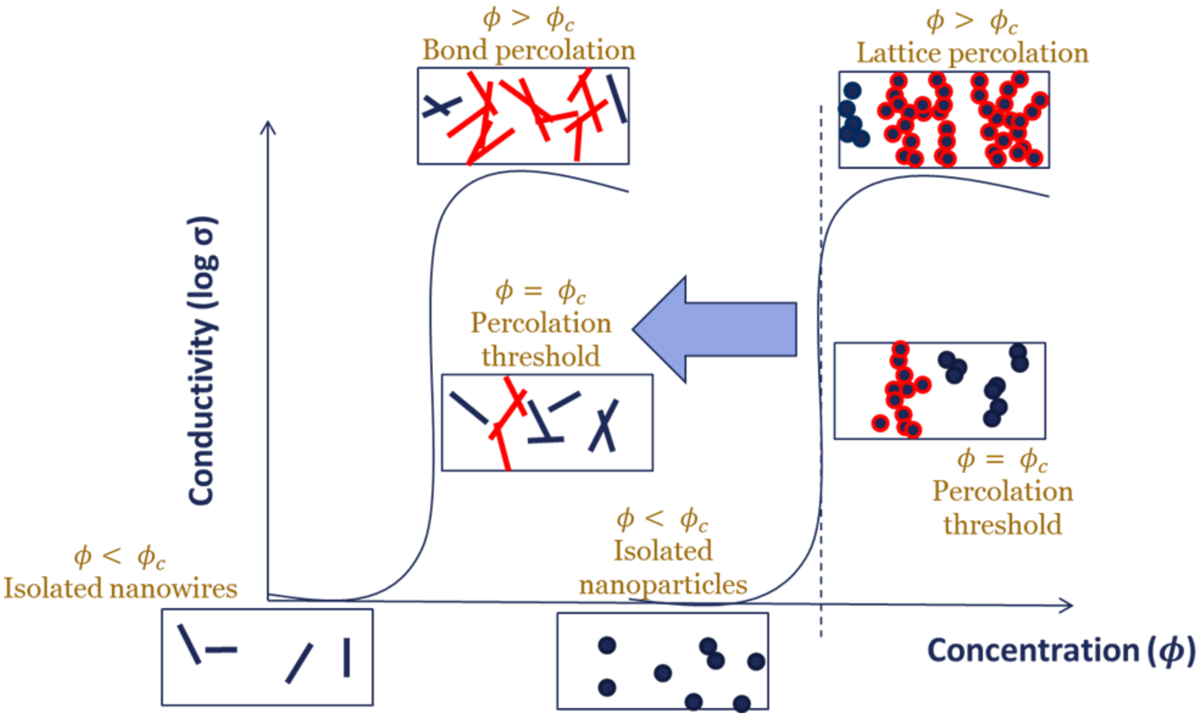

**Figure 6.2 Percolation threshold shifting by nanostructure shape modifying**

Based on the percolation model of soft-core cylinder, the sheet resistance (Rs) of Ag NWs network can be expressed as: 164

$$R_s \propto (N - N_c)^{-\alpha} \tag{6-1}$$

where N is the density of wires and Nc and α are the critical density and exponent for percolation threshold. The critical exponent ranges from 1.33 to 2 based on the dimension of samples. To sum, increasing the length and width ratio of metal nanowires is a promising strategy to improve both electrical and optical properties.

Herein, according to Fuch's size-dependence electrical resistivity theory, if the diameter of nanowire keeps decreasing, when it is small compared to the mean free path of an electron, the resistivity of nanowire increases.[165] Hence, it's not practical to decrease the width of nanowire under the limitation in order to keep it conductive. The major aspect for nanostructure optimization goes to controlling the length of nanowires.

### 6.1.3 Metal-Oxide Interface

The barrier forms at the interface of metal and oxide can be calculated and illustrated by the energy band diagram. With different band gap, metal and semiconductor can form either Ohmic contact or Schottky contact.

For n-type semiconductor, the barrier $\varphi_B$ defined as the potential difference between the metal Fermi energy and the band edge where carriers are accumulated. [19]

$$\varphi_B = \varphi_M - \chi \tag{6-2}$$

For p-type semiconductor, the barrier $\varphi_B$ defined as the potential difference between the metal Fermi energy and the valence band edge. [166]

$$\varphi_B = \frac{E_g}{q} - \varphi_M + \chi \tag{6-3}$$

ZnO is known as an n-type semiconductor with wide bandgap around 4.2 eV. The intrinsic ZnO has low resistance due to defects, such as oxygen vacancies and interstitials. By doping n-type element Al, it is promising to further reduce the resistance. The electrons excite from donor band to conduction band by thermal excitation. The donor energy level for Al/Zn is reported to be as low as 13meV. From previous research, the work function of Al:ZnO films ranges from 3.7 to 4.6 eV, and the work function of nanostructured Ag is 4.2 to 4.6 eV. 167

Therefore, Ag and Al:ZnO interfaces form the Schottky barrier, shown in Figure 6.3. The value of Schottky barrier is governed by the difference of metal work function ($\varphi_M$) and the affinity of oxide semiconductor ($\chi$).

$$\varphi_{SB} = \varphi_M - \chi \tag{6-4}$$

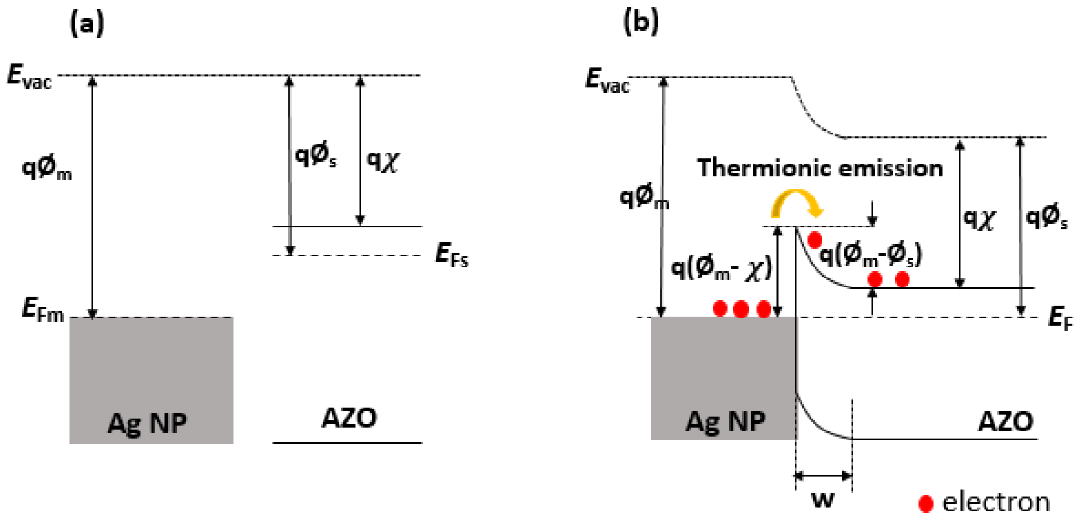

**Figure 6.3 Formation of Schottky barrier at Ag and Al:ZnO interface** [168]

Carriers can jump from nanostructured metals into semiconductor matrix by thermionic emission. The Schottky barrier attributes to the activation energy. Also, the nanostructured metal increases the metal-oxide interface areas to several orders of magnitude, which also accelerates the donation of carriers to the oxides in the near field of metals.

### 6.1.4 Scattering and Hazeness

It is worth noting that good transparency may not guarantee the optical performance of TCs. The difference in refractive index between the materials inevitably increases the scattering, which leads to blurriness of the TCs that fails to utilize in the industrial applications. To address the scattering problem, nanoparticle decoration method is proposed and discussed using simulation.

When an electromagnetic (EM) wave encounters a particle, the electron orbits around the particle will be perturbed periodically according to the frequency of the EM wave. This will lead to a displacement of the particle charge and generate a so-called induced dipole moment. [169]

The induced dipole moment in turn generates EM wave. Those new EM waves are mostly in the same frequency as the incident EM wave. This is called the Rayleigh scattering.

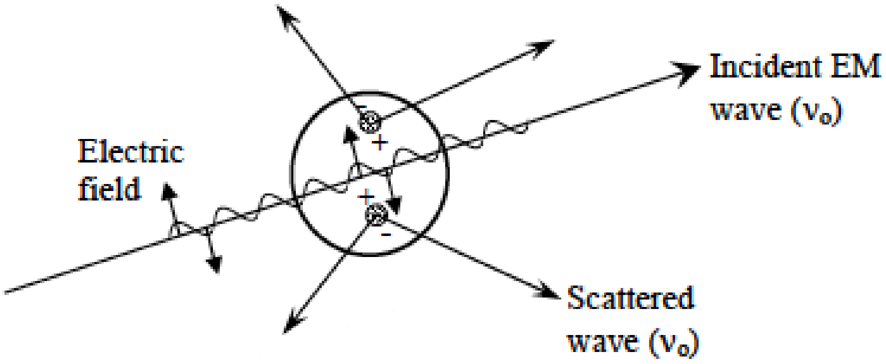

**Figure 6.4 Light scattering by an induced dipole moment due to an incident EM wave.** [170]

There are two dominating light scatter theory, i.e. Rayleigh scattering and Mie scattering. Rayleigh scattering generally applies to small dielectric spherical particles, where Mie scattering applies to more spherical particles without size restriction. However, Mie scattering theory is much more complicated so Rayleigh scattering theory is preferred when it is applicable.

Mie scattering,[172] also known as the Lorenz-Mie solution or the Lorenz-Mie-Debye solution, is usually used to simulate the scattering of an electromagnetic plane wave by a homogeneous sphere, and then also used to simulate the scattering of infinite cylinders or other structures. For scattering of tiny particles or molecules, which are smaller than 1/10 wavelength, is dominated by Rayleigh scattering, but for scattering of larger particles, whose size is larger than wavelength or comparable to wavelength, Mie scattering is dominated. Mie scattering leads to an antenna lobe. The larger the particles are, the shaper and more intense the lobe will be.

Two possible methods might be feasible to eliminate the scattering of Ag NWs: increasing the aspect ratio (enlarging the length or reducing the radius) or suppression the scattering by other nano-decors. First of all, during the research, the aspect ratio has been changes from 60 to 400. According to Fuch's size-dependence electrical resistivity theory, 173 if the diameter of Ag NW keeps decreasing, when it is small compared to the mean free path of an electron, the resistivity of Ag NW increases. Hence, our Ag NW diameters are around 40-50nm and the former method is not considered. Then, the possible solution goes to the later on, suppressing the scattering by nanodecors.

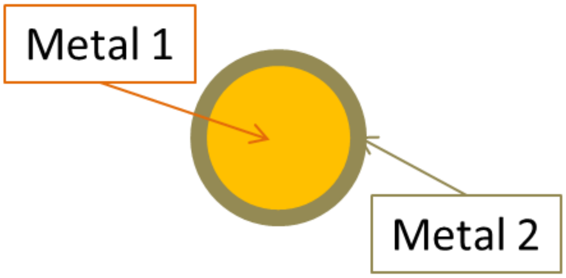

**Figure 6.5 Illustration of metal 1 decorated by metal 2 (nano-shell or nanoparticles)**

When a nanostructured metal (M1) is covered by a shell or nanoparticles (M2), if the extinction coefficient k(M1) < k(M2), which indicates that M2 would have relatively higher absorption, the scattering of M1 can be effectively suppressed via broaden and weaked the originally sharp extinction peak. Kim and el. [174] have reported Au coated Ag NWs with a reduction in hazeness from 28% ~ 43% with same transmittance and competitive resitance. Menamparambath [175] and el. has proposed a structure of Ag NW decorated with Ag NPs, which has a low resistance around 24.1 ohm/sq., transmittance around 96% and haze as low as 1.04%.

## 6.2 Influence of ZnO Capping on the Resistance of Ag NW Junctions

### 6.2.1 Synthesis, Fabrication and Characterization

Ag NWs with various aspect ratios are synthesized using the polyol method. By changing the molar ratios of poly(vinylpyrrolidone) (PVP) (Mw= 55,000gmol$^{-1}$) to 1-butyl-3-methylimidazolium chloride(BMIM-Cl), reaction temperature and time, both the lengths and widths of Ag NWs can be modified. PVP is firstly dissolved into propylene glycol (PG) and then heated to the reaction temperature. Then BMIM-Cl followed with silver nitrate ($AgNO_3$) is added to the solution generally. After the reaction, the solution is cooled down in a Teflon bottle and washed by ethyl acetate and acetone respectively. Al:ZnO sol-gel precursors are composed of zinc acetate zinc acetate dehydrate [$Zn(O_2CCH_3)_2 \cdot 2H_2O$, 99.99%] dissolved in 2-methoxyethanol [$CH_3O(CH_2)_2OH$, 99.8%] with monoethanolamine [MEA, NH2(CH2)2OH, 98%] serving as a sol stabilizer and aluminum nitrite. After aging for 24hr, the precursors are then mixed with Ag NWs solution. AgNWs/ ZnO solutions are spin-coated on the glass substrates followed by annealing under nitrogen atmosphere at 500$_{o}$C for 1hr, and under forming gas (5% hydrogen + 95% nitrogen) at 400℃ for other 1hr in order to prevent the unexpected oxidization. The illustrations are shown in Fig.1. By coated layer-by-layer, the contacts between AgNWs are holding the resistance Rc.

*Fabrication processing*

AgNW/ZnO precursor was spin coated on glass slide substrate at a spin rate 3000rpm, followed by baking on the hotplate for 10min for each layer to remove the organic parts. Then the samples were heat treated at 500$_{o}$C with the protection under N2 for better crystallinity. Ag NWs remained in shape after the fabrication processing.

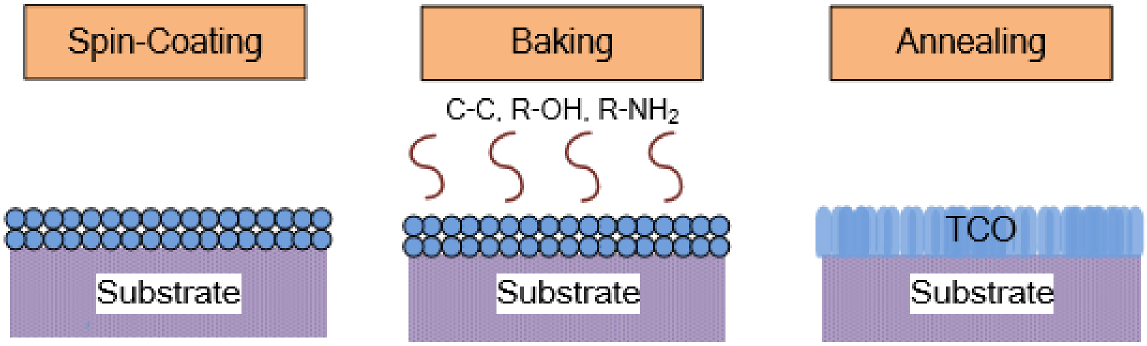

**Figure 6.6 The process of fabrication of Transparent and conductive electrode**

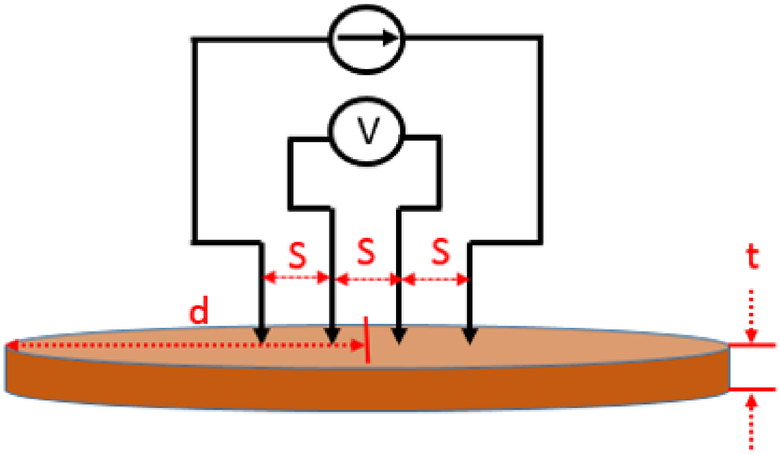

**Figure 6.7 The schematic diagram of four point probe 175**

Sheet resistance of thin film was measured using four point probe, shown in the Figure6.6. Current were applied in the two outer probes, while voltage value was monitored by the two inner probes. The resistivity followed the relationship:

$$\rho = \frac{V}{I} \cdot CF \tag{6-5}$$

where CF = 4.532 for thin film samples, due to thickness t << diameter d. The calculated value was independent to the size of the sample, facilitating the direct comparison between different samples from other groups.

### 6.2.2 Result and Discussion

A change in the dimension of Ag NWs was achieved by controlling the ratio of surfactant PVP and synthesis temperature. In this study, the junction density was supposed to change via the change in Ag NWs aspect ratio. Higher junction density exaggerates the influence of AZO on Ag NWs networks.

**Table 6.1 Reaction condition for Ag NW with different aspect ratio**

| No. | PVP/BMIM-Cl | Temp.(C) | Time(hr) | Length(um) | Width(nm) | L/D |
|---|---|---|---|---|---|---|
| #1 | 2/1 | 90 | 22 | 17 ± 6 | 45 | 450 |
| #2 | 2/2 | 125 | 2 | 5 ± 2 | 50 | 100 |
| #3 | 3/5 | 125 | 2 | 3± 1 | 44 | 67 |

Figure.6.7 shows the experimentally measured transmittance and resistance of Ag NW networks with and without AZO matrix. The effect of AZO on the sheet resistance of the composite is pronounced when Ag NW content is low and L/D ratio of Ag NW is small. If the content of Ag NWs is not large enough to form a NW percolation network, the role of AZO matrix to fill the space between NWs controls the electric conductivity of the composite. From the standpoint of electron transport, AZO matrix bridges Ag NWs to Ag NWs with Rc, instead of Rj, so that electrons are able to move between Ag NWs. As the L/D ratio increases, a same amount of Ag NWs has more intersections in AZO matrix. Therefore, the effect of AZO matrix on the sheet resistance becomes more obvious for Ag NWs of the higher L/D. From the standpoint of the

electric properties, Ag NW with high L/D has good performance as transparent and conductive thin films, however, for Ag NW network with lower L/D, the function of ZnO is more obvious when Ag.% is close to the percolation limit.

While Ag NWs improve the electric conductivity, they do not have a positive impact on the optical transmittance which is also an important requirement of the transparent conducting materials. After the percolation is reached, more Ag NWs are randomly stacked and the surface roughness of Ag NWs/ZnO film is increased. This leads to a decrease in the specular transmittance and an increase in the haziness. Although the optical properties for Ag NWs/ZnO thin films with higher Ag content have no advantages compared with pure Ag NWs networks, the sheet resistance for Ag NWs/ZnO can be improved with high Ag vol%.

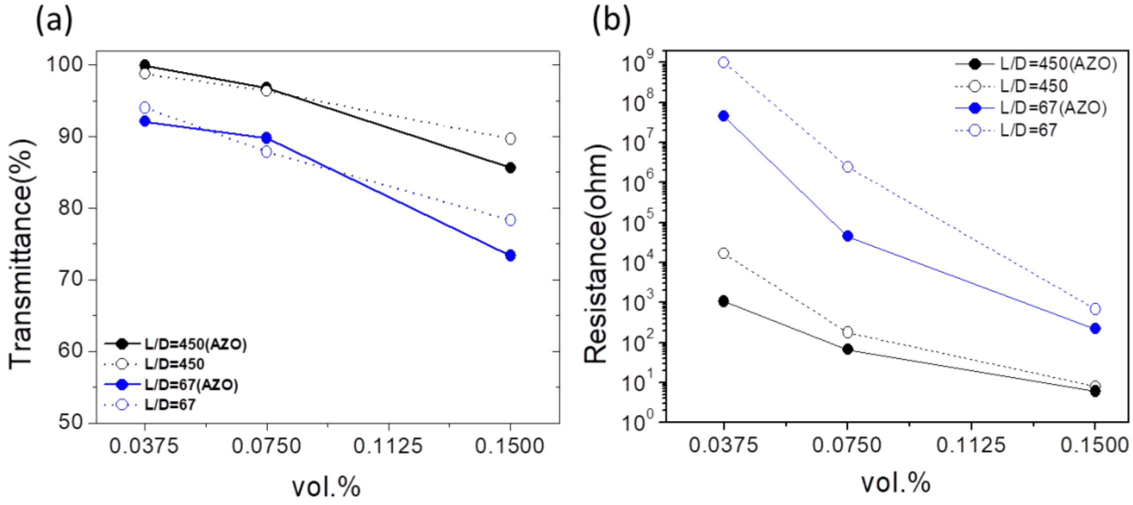

**Figure 6.8** **Experimentally measured electrical and optical properties**

For evaluation the electrodes, both conductivity and transmittance are critical properties. However, electrical and optical properties are mutually exclusive. Say, films with high Ag concentration would have high conductivity but the transmittance would be lower than 80%, which makes it a failure of TC films. Therefore, the equation of Figure of Merit (FOM) first introduced by Haacke [177], are applied to estimate the performance of TC electrodes in this paper.

Table.6.2 listed the value calculated by this equation for our samples and other widely used TC samples. Our AZO:Ag NW electrode has higher FOM than commercial ITO[179] and CNTs [178] and a competitive one compared to meshed Ag NWs [180]. The AZO matrix attributes to reduce the contact resistance and bring down the Ag NW percolation threshold. It's promising to get percolating Ag highly conductive path with less Ag content.

**Table 6.2 Transmittance at 550nm, sheet resistance and Figure of Merit**

| | **$T_{at\ 550nm}$(%)** | **Rsh (ohms/sq)** | **FOM** |
|---|---|---|---|
| **Our AgNW/AZO** | 85.63 | 6 | 371.2 |
| **CNTs [31]** | 83 | 25 | 77.2 |
| **ITO [32]** | 80 | 10 | 159.7 |
| **Ag NW meshes [33]** | 90 | 24 | 393.5 |

As shown in Figure.6.8, a trade-off relationship between transmittance and sheet resistance is observed. Similarly, the data points with excellent Rs and T are expected to come into existence at the left upper corner of the figure. FOM figure indicates that at low Ag content close to percolation limit, the AZO matrix is critical for decreasing the sheet resistance of films, especially for the films with small L/D. The reason for this phenomenon can be explained as AZO matrix bridges AgNWs to AgNWs with Rc, instead of Rj, so that electrons are able to transfer along the Ag NWs body. After percolation, AgNWs/AZO surface roughness is enlarged due to the stacking of NWs, which leads to the decrease of Transmittance dramatically. Although the optical properties for AgNWs/AZO thin films with high Ag content have no advantages compared with pure Ag NWs networks, the sheet resistance for AgNWs/AZO can be improved with high Ag content. Ag NWs network with high L/D supposes to have more intersections. As a result, the effect of AZO matrix becomes more obvious in thin films with high L/D then those with low L/D.

Figure.6.8 (b) shows the temperature-dependent resistivity of Ag NWs/AZO in the range from 303K to 178K. The electrical conductivity enhanced by orders of magnitude with addition from 0.0375 vol.% to 0.15 vol.%, indicating the percolating of Ag NWs in the composite. As resistivity increases with the temperature, the electrical conductivity is attributed to the metallic filler Ag NWs.

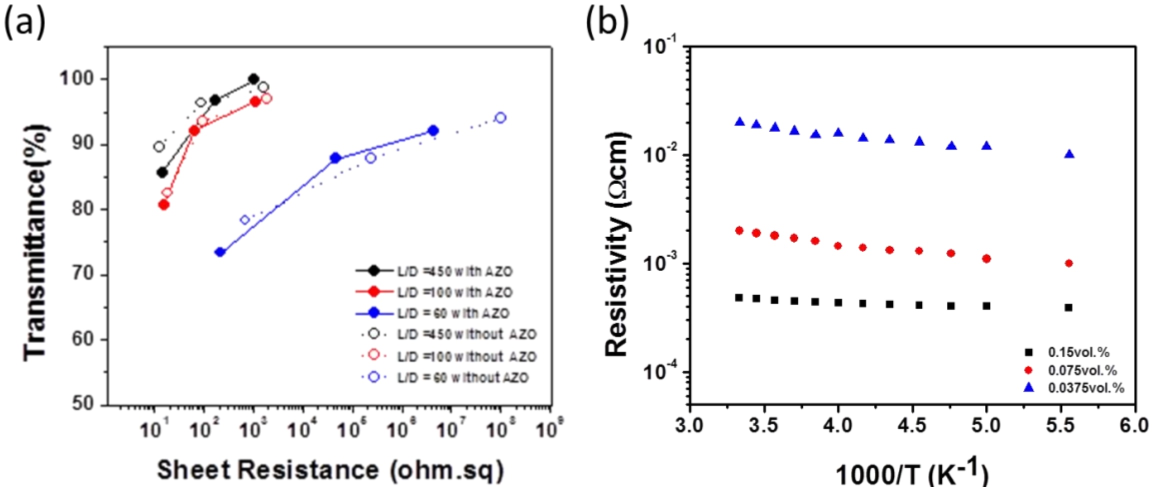

**Figure 6.9 (a) Transmittance(%) at 550nm versus. sheet resistance (b) temperature-dependent resistivity of AgNW/AZO composites**

Intensive efforts have been done on 2D Ag NW stick percolation models. Within the scope of our study, the impact of AZO on the junction resistance and percolation threshold are emphasized to be explored. In order to combine the simulations with experimental observations, a 3D model with layer-by-layer structure is implemented and compared with 2D stick models under different Ag NW aspect ratio. All the simulations in this study involves two parts: (a) formation of percolating networks and the detection of junctions utilizing JAVA and (b) operation of optical and electrical simulation in commercial software, FDTD Lumerical and Ansys Electronic. The system was defined as a 3D box with a fixed side length L and a height of proportional to the diameter of Ag NWs, indicating the number of layers of the composite. Two electrodes were placed at two ends of the box. Randomly distributed Ag NWs networks were then added to the 3D box with assigned coordination and angle generated in JAVA. It's noticeable that the conductive matrix effect on the junction resistance of Ag NW is the major consideration in this study. The layer-by-layer structure of Ag NWs/AZO composite that we applied for composition fabrication and simulation effectively prevent the tangling of Ag NWs. The intersection between two Ag NWs is assumed to be connected via AZO. Illustration of the 3D model is displayed and explained in Figure.6.9. In contrast to 2D model where all the intersections between Ag NWs are set to be the joint points (blue dots) with a resistivity Rj, in 3D model, two Ag NWs are connected with AZO contact, whose resistivity is $R_c$. Due to layer-to-layer structure, the intersections of Ag NWs can be viewed into two groups: contact points (red dots) when the plane of one Ag NW is close to the one of the other Ag NW and passing points (green dots) when two planes are separating far away from each other, whose resistivity has no difference with body resistivity, $R_{Ag}$ ($R_{Ag} <<$ Rc). So that electricity tends to go directly through nanowire instead of hopping to the neighboring Ag NWs through intersections.

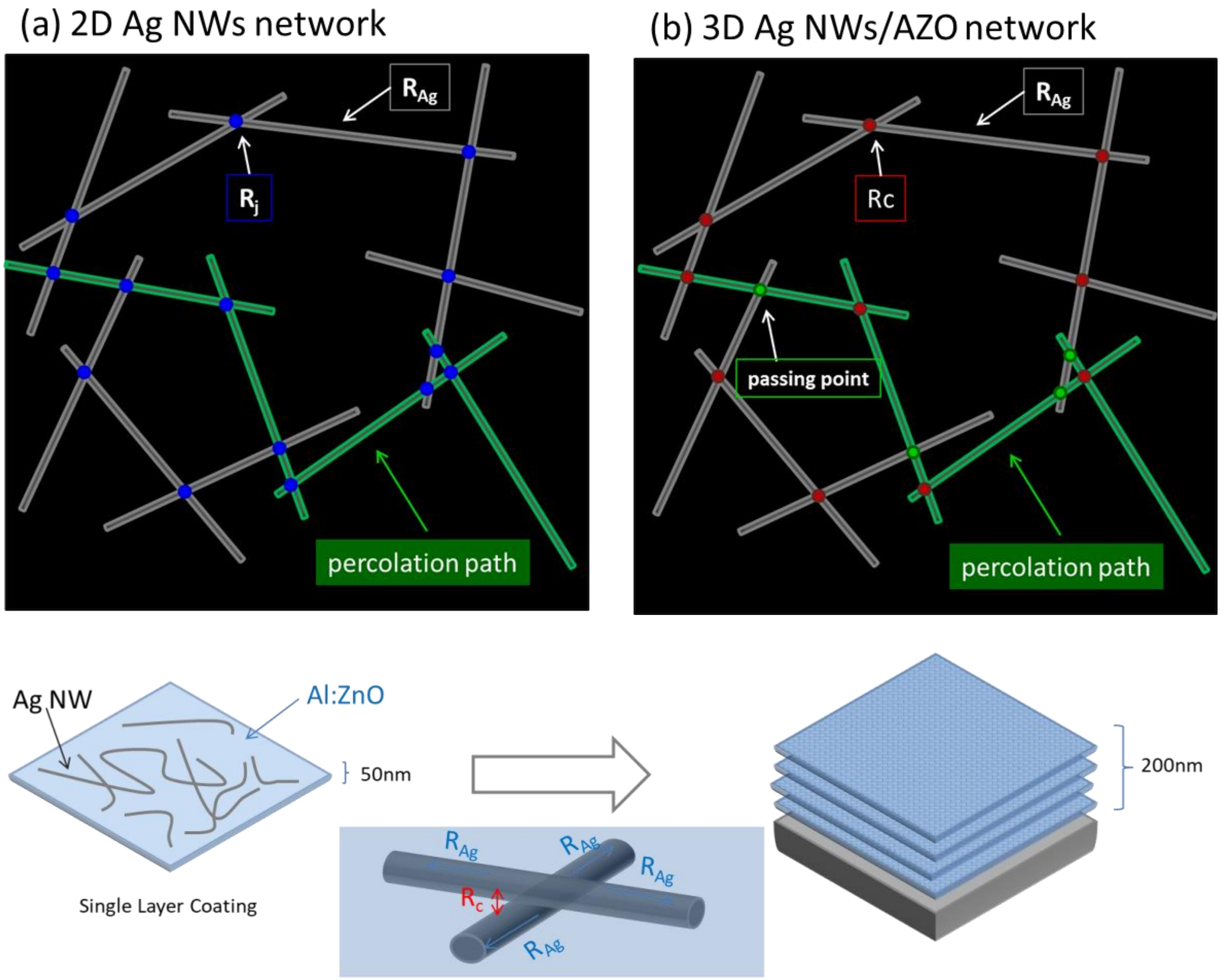

**Figure 6.10 Top view of percolation paths for (a) 2D Ag NWs network; (b) 3D Ag NWs/AZO network**

**(c) Conceptual illustration of Al:ZnO capped Ag NWs thin films fabrication**

The combination of simulation with experimental Figure of Merit is presented in Figure.6.10 to better understand the effect of AZO as conducting matrix to reduce the junction resistivity and the percolation threshold of Ag NWs. Both the Ag NWs and AgNWs/AZO samples exhibit indicative trade-off relationship between transmittance and sheet resistance. With higher junction density, the influence of AZO on the junction resistance of Ag NWs is more dominant due to a reduction of junction resistance as well as the extension of electron diffusion length. Electrons hop to the neighboring wires more easily which push the percolation threshold of the Ag NW networks.

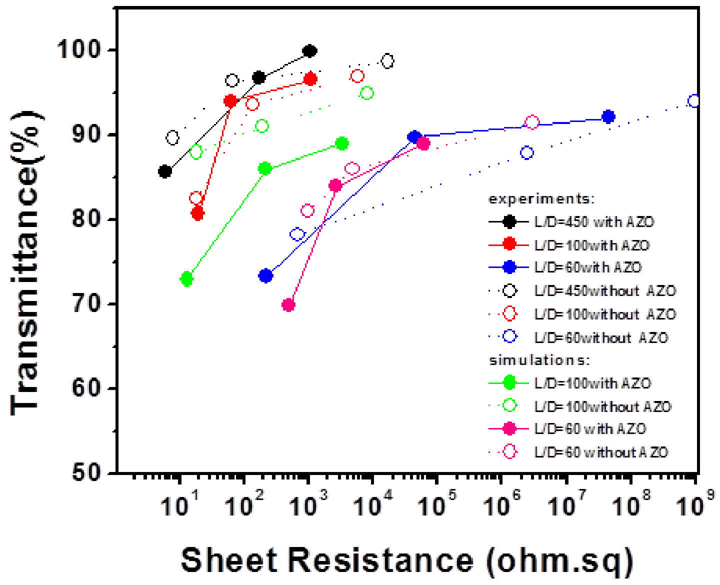

**Figure 6.11 Experiment and simulation on electrical properties with and without AZO matrix**

Furthermore, we aim to reduce the haze of TCs by suppressing the scattering via nano-decors, such as nanoparticles or nanoshells. In figure 6.11(a), optical properties: refractive index (n) and extinction coefficient (k) of four materials, Au, Ag, Cu and ZnO are plotted and compared.

If k(core) < k (shell), the scattering of Ag would be decreased. For an Ag nanoparticle with diameter around 40~50nm, the extinction (absorption) peak would sit at the wavelength around 400nm. In that range, Cu and Au can be the candidates that meet the requirement of large k.

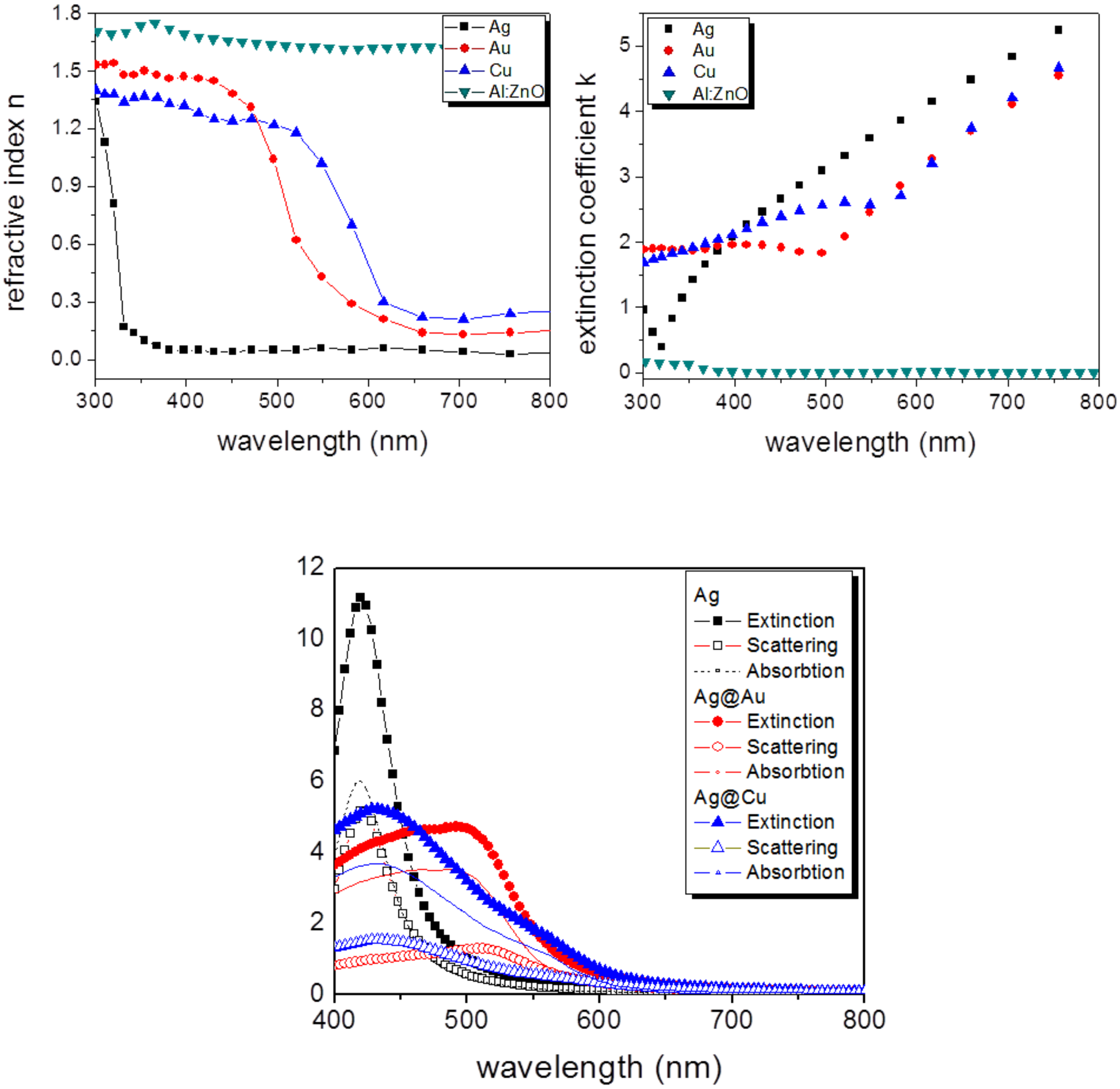

**Figure 6.12 optical properties of materials, Ag, Au, Cu and Al:ZnO and (b) the Extinction cross section of core-shell nanoparticles calculated using Mie scattering theory**

In Figure 6.11(b), the extinction, absorption and scattering for Ag NPs coated with Au and Cu shells are presented. The case would be different with our Ag NW case, but the phenomenon is still interesting to be discussed. From the figure, the blue and red dotted line is obviously lower than the black dotted line, which indicates our assumption that nano-decors can be a solution for suppression the scattering. In the future work, we would like to do both experimentally and computationally on this concept and try to study systematically on how nano-décor on the Ag NWs/ZnO can effectively reduce the Hazeness of the TC films.

For TC films, promising to be fabricated in photoelectrical applications, the heat resistance is another important parameter. The electrons mainly propagate along the Ag NW networks to form conductive paths and these paths are terminated when the Ag NWs are melted and broken due to the high temperature. By this rule, heat resistance test is designed as heating the Ag NWs/AZO films and pure Ag NWs films under different temperature ranging from 50℃ to 550℃, while electrical sheet resistances for each film are recorded. As shown in Figure.6.12(a), a clear "turning-point" can be observed for pure Ag NWs networks around 200℃, illustrating the Ag NWs start melting and being unable to transport electrons continuously. Conversely, the Ag NWs/AZO films are characterized as strong heat-resistant films, which have relatively flat curves for heat resistance test. This is caused the protection by AZO covering around the Ag NWs. Figure 6.12(b) serves as another evidence that Ag NWs protected by AZO matrix are not oxidized. The Ag 3d5/2 peak for Ag is 368.2eV and will shift to 367.9eV after oxidizing into $Ag_2O$ and 367.6eV after further oxidizing into AgO. The oxidization of Ag into $Ag^{2+}$ leads to the rising of resistance.

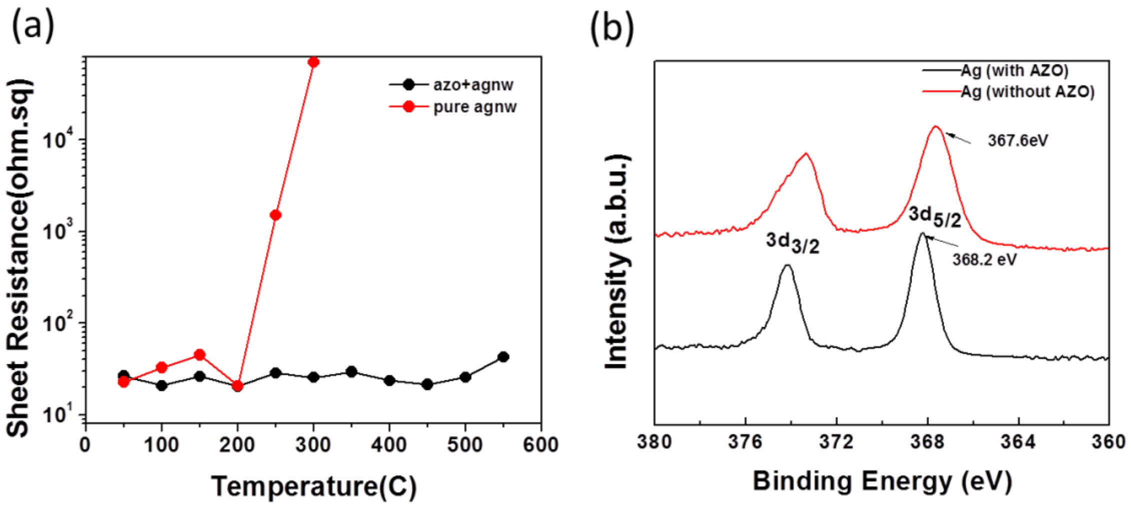

**Figure 6.13 (a) Heat resistance test; (b) Ag element XPS after heating resistance test**

Humidity resistance test is accomplished by exposure of Ag NWs/AZO films and pure Ag NWs films under a total humidity environment, shown in Figure6.13 After certain amount of exposure time, the increase of the sheet resistance for pure Ag NW film is quite remarkable due to the oxidization of Ag NWs, while the one for Ag NW/AZO film is stable even being immersed into the water. In this case, the evidence that Ag NWs are protected by AZO is also observable. As mentioned in heat resistance test, $Ag_+$ 3d5/2 locates at 367.9eV, while $Ag_{2+}$ 3d5/2 appears at 367.6eV. Ag $3d_{5/2}$ in salt can be shifted into more higher binding energy, such as 368.2eV, 369.2eV and 371.4eV.[181] The oxidization and chemical reaction of Ag NW in high humid environment is more complicate than the one in dry air. The Ag $3d_{5/2}$ indicates a mixing status of $Ag_2O$, AgO and $Ag_{+/2}$+ in salt.

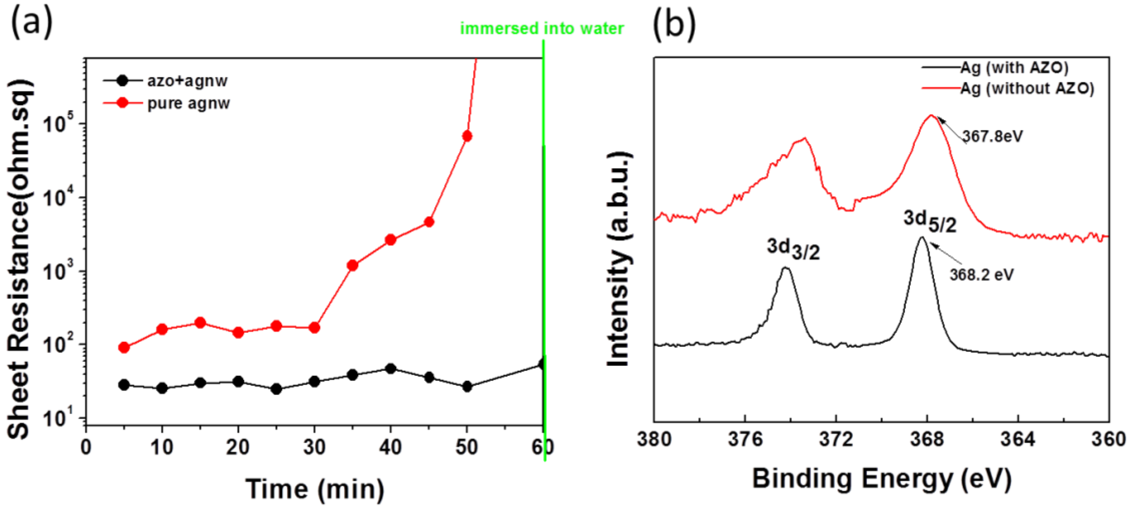

**Figure 6.14 (a) Humidity resistance test; (b) Ag element XPS after humidity test**

# 7.0 Conclusion and Future Work

## 7.1 Conclusion

### 7.1.1 Microwave-Assisted $La_{0.8}Sr_{0.2}MnO_3$

The effect of the microwave-irradiation on the microstructure, crystal structure, electrical conductivity and chemical stability of LSM ceramics was systematically investigated. The microwave radiation stimulates the dissolution of smaller nanoparticles and promotes Oswald ripening of precipitated nanoparticles in the aqueous solution. In addition to the nanoparticle size, the microwave-irradiation changes the crystallization path of as-synthesized nanoparticles and increases the grain size of LSM ceramics by preventing the formation of the second phase. Faster grain growth of LSM ceramics from the microwave irradiation, in turn, lowers the energy barrier for the small polaron hopping and increases the electrical conductivity. Moreover, the microwave irradiation also suppresses the chemical reaction of LSM ceramics with YSZ and NiO at high temperature in the reducing ambiance. Our study suggests that the microwave-assisted reaction is a promising method for the synthesis of perovskite LSM that meets the requirements for interconnect or symmetric electrode of SOECs.

### 7.1.2 LSM:Ni Composite as High Temperature Conductors

Our LSM-Ni composite (modified by Ni size) has high electrical conductivity in both air and in forming gas ($H_2/N_2$=5%) as well as high density close to 99%. This makes it promising to be applied as the interconnect part in SOFCS or SOECs. Ni addition in the LSM forms metallic percolation path in reducing ambiance while LSM shows excellent conductivity in oxidizing ambiance. The second phases, $La_2NiO_4$ (with Sr doped), induces the liquid phase sintering and thereby enhance the density.

### 7.1.3 Double-Layer Interconnect for SOFCs

Shrinkage mismatching between double layer coating can be eliminated by either Sr doping on LSM layer or Ni size on LSM:Ni layer. The shrinkage rate of anode support YSZ-NiO is of importance to the final densification of the interconnect coating. Furthermore, the interfacial reaction between anode support and interconnect layer can be suppressed effectively by compositional adjustment the A/B ratio. Finally, dense dual-layer LSM/LSM:Ni interconnect is successfully fabricated on the porous YSZ-NiO anode support after co-sintering. Area-specific Resistance (ASR) stability measurement in a simulated environment, dual atmosphere at high temperature (air in one side/ forming gas in the other side) confirms the feasibility of LSM/LSM:Ni structures as a promising interconnect for SOFCs/ SOECs with lower resistance and devcelerated gas penetration.

### 7.1.4 Percolation Properties of Ni in LSM:Ni Composites

It is demonstrated that LSM:Ni composites were promising to serve as the conductors at high temperature in both reducing and oxidizing environment. By adjusting the aspect ratio of Ni and introducing the anisotropy, from a/b =1 to a/b =1/10 or 10, the percolation threshold of Ni can be effectively limited. With less amount of Ni, the sintering behavior can be improved. The results of electrical conductivity measurements showed that LSM:Ni Sphere 30%, LSM:Ni Plate 10,20,30% and LSM:Ni wire 20,30%. Also, the packing and mixing of LSM with different Ni shapes cause more or less LSM-Ni contact. The Ni contact with La possibly undergoes much slower oxidation rate, which is beneficial to prevent inter-granular cracks during sintering.

### 7.1.5 Ag NW/ZnO as Transparent Conductive Electrodes

The optical and electrical properties of Ag NWs/Al:ZnO are studied computationally and experimentally by controlling the aspect ratio L/D of Ag NWs. With the coverage of Al:ZnO, contacts are formed easily between Ag NWs, so that the electrons are able to go directly along Ag NW or hopping into neighboring NW through contacts. Al:ZnO matrix plays an important role in increasing the figure of merit (FOM) and decreasing the percolation threshold of Ag NWs. Compared with pure Ag NWs thin films, AgNW/Al:ZnO composite electrode has competitive transmittance with lower resistance. The optimal AgNW/Al:ZnO thin film (L/D=450) has >85% in transmittance and <10 ohm/sq in sheet resistance. The scattering of Ag NWs can be attenuated by the metallic nanoparticle decoration. Additionally, our AgNWs/ Al:ZnO is thermally stable under 500$_o$C with good humidity resistance.

## 7.2 Future Work

### 7.2.1 $La_{1-x}Sr_xMn_{1-y}Cu_yO_3$ Double Perovskite

A-site or B-site substitution of $LaMnO_3$ perovskite structure by has been widely investigated to change the structural and electrical properties. Previously, we have discussed that low valenced $Sr^{2+}$replacement on A-site $La^{3+}$ would generate more $Mn^{4+}$ to maintain charge balance and thereby the electrical conductivity has been improved by A-site dopant by the increment on polarons concentration.

B-site doping on LSM is promising to promote the formation of oxygen vacancies and change the electric and magnetic properties as well. Materials with the mixed electronic and ionic conduction are promising cathodes for SOFCs, oxygen sensor or electro-catalyst members for their sensitivity on oxygen partial pressure. Many attempts have been done by other groups, such as Co, Ni, Cr and Fe. With Co doping, Conductivity decreases at 20%, then increase at 40% due to hole/electron charge compensation.[182] $La_{0.6}Sr_{0.4}Co_{0.8}Mn_{0.2}O_3$(LSCM) has high electrical conductivity of 1400 S/cm. [183] With Fe doping, conductivity decreases with Fe addition due to a reduction of available sites for hole hopping conduction.[184] With Cr doping, although the conductivity decreases, chemical stability in both reducing and oxidizing ambiance can be improved. [185]

Cu is also taken consideration as an aliovalent doping element, the most stable state of Cu is $Cu^{2+}$ but there is also a $Cu^{3+}$ state. The substitution of $Cu^{2+}$ into the B-site in LSMO can be compensated by the formation of $Mn^{4+}$. Increased $Mn^{4+}$ concentration can create more $Mn^{3+}/Mn^{4+}$ pairs, which act as hopping sites for hole conduction. [186] Furthermore, the Cuprates are reported as high temperature superconductor. $La_{2-x}Sr_xCuO_2$ (LSCO) was first discovered by Bednorz and

Muller.[187] as a typical hole doped high transition temperature (Tc) Cuprate materials (Tc = 35K-138K). It has high hardness with strong bonds. The single crystal is expected to grow as big as 1cm. LSCO represents metallic behavior when x = 0.15, 0.3 [188] and are characterized as good cathode materials for SOFCs.[189] Also, the LSCO, x=0.2, has been reported to have an excellent conductivity ~210 S/cm at 750°C.

Besides on the hole/electron charge compensation, dimensional mismatch between A-site and B-site cations is also a major point that affects the electrical properties and crystallinity and stability. In table7.1, the ionic radius with different valence has been listed.

The idea of tolerance factor, introduced by V.M Goldschmidt can be discussed here:[190]

$$\text{Goldschmidt tolerance factor } t = (r_A + r_O)/[2^{\frac{1}{2}}(r_B + r_O)] \qquad (7\text{-}1)$$

where $r_A$ is the average radius on A-sites, $r_B$ is the average radius on B sites. The value can be used to predict the suitability of the dopants in pervoskite structure.

**Table 7.1 Ions radius with different valence**

| Element | 2+ | 3+ | 4+ |
|---|---|---|---|
| Mn |  | 0.645 | 0.53 |
| Ni | 0.69 | 0.6 |  |
| Cu | 0.73 | 0.54 |  |

In the future work, we want to come after the idea in Chapter 03, by changing in Cu nanoparticle size, Cu doped LSM can be obtained during sintering process, which attributes great conduction in air at intermediate temperature. The conductivity of Cu doped LSM is supposed to be better than LSM. In addition, the microstructure of LSCMO/Cu composite is easily adjusted via Cu nanoparticle size and content. Fine grains and reasonable porosity are preferred for cathode materials, while dense layer is expected for electrode materials. It's also possible that fine Cu nanoparticles might incorporated completely into LSM lattice to form the single phased LSCMO. More efforts should be taken to study on Cu incorporation LSCMO/Cu system and its potential to be used as cathode or electrode materials for intermediate SOFCs.

*Experimental and discussion*

Cu NPs has been synthesized using polyol method, with average particle size ~1um. 1g PVP(MW=55,000) was added into 30mL EG. Then the Cu(II) formate hydrate was added and stirred until the solution is clearly light blue color. Ascorbic Acid was then added in as the reducing agent here instead of Sodium Brohydride. The solution was holding at 160$_{o}$C for 1hr, until it turns into red. (indicating Cu had not been oxidized) The whole synthesis process was protected with Nitrigon gas.

**Figure 7.1 Cu NPs as synthesized. Cu NPs solution without oxidation should stay in red color**

SEM shows the morphology of LSM:Cu (1um) mixture after sintering at $1400_{\mathrm{o}}$C. Since the tolerance factor is close to 1, Cu incorporated into LSM perovskite lattice, so that the crystal structure turned back from rhombohedral to cubic structure. In addition, the temperature-dependent resistivity shows that Cu incorporation decreases the resistivity in one or two orders of magnitude.

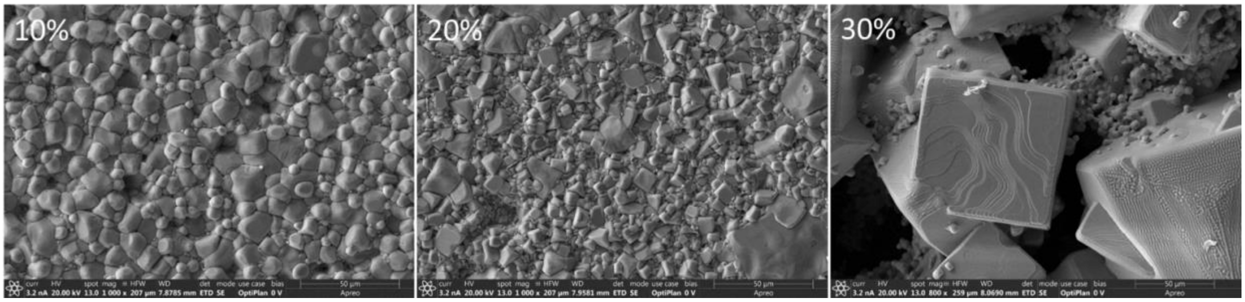

Figure 7.2 SEM morphology for LSM:Cu bulks with 10%, 20%, 30% Cu after sintering at 1400$_o$C

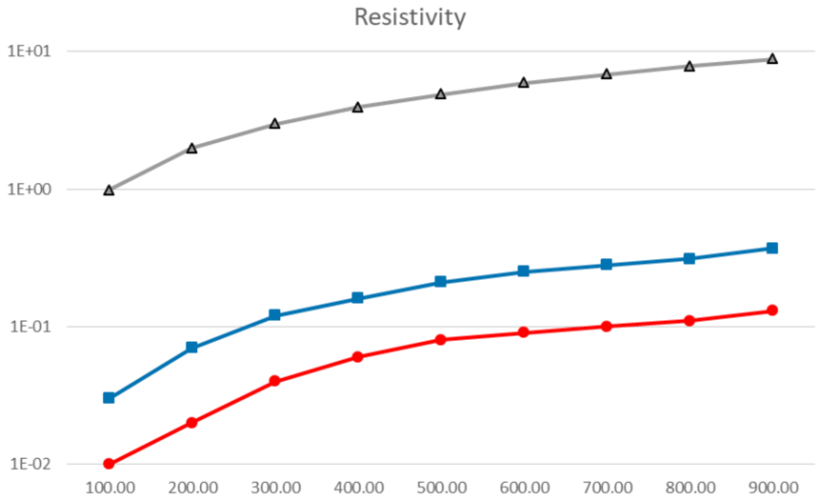

Figure 7.3 Sheet resistance of LSM:Cu mixture after sintering with 10%, 20% and 30% Cu after sintering

### 7.2.2 Perovskite with Low Sintering Temperature

Perovskite materials have been widely used as ceramic interconnect or coating layer on metallic interconnect. However, the ambiance-dependent conductivity impact is deteriorated. These perovskite oxides are either p-type or n-type, which indicates the electrical properties would be excellent only in oxidizing or reducing ambiance. To solve the problem, it is feasible to build a double-layer interconnect, with p-type coating on one side and n-type coating on the other side. Sintering and densification becomes the most important role to find the candidates materials for p-type layer and n-type layer.

LSF is commonly studied p-type conductors, La or Y doped STO, on the other hand, is good candidate for n-type conductors owing to their low sintering temperature. [191-192]Also, it has been found in our previous study, Sr doped LNO has good conductivity in air at intermediate temperature with low sintering temperature. It is essential to study on the p-type or n-type perovskite with low sintering temperature and fabricate the double layer ceramic interconnect with excellent conductivity under operating condition at intermediate/high temperature with high density to inhibit gas penetration effectively.

*Experimental and discussion*

Traditional solid-oxide synthesis method was applied to make LNO and Sr doped LNO, following the stoichiometry below:

$$La_2O_3 + NiO \rightarrow La_2NiO_4 \tag{7-2}$$

$$La_2O_3 + SrCO_3 + NiO \rightarrow La_{1.7}Sr_{0.3}NiO_4. \tag{7-3}$$

Both samples, especially LSNO, show excellent electrical conductivity in air. They also have been reported as cathode candidates. The conduction mechanism is small polaron hopping in a perovskite structure just like LSM. LSNO has extremely low resistance even at Room Temperature in oxidizing ambiance.

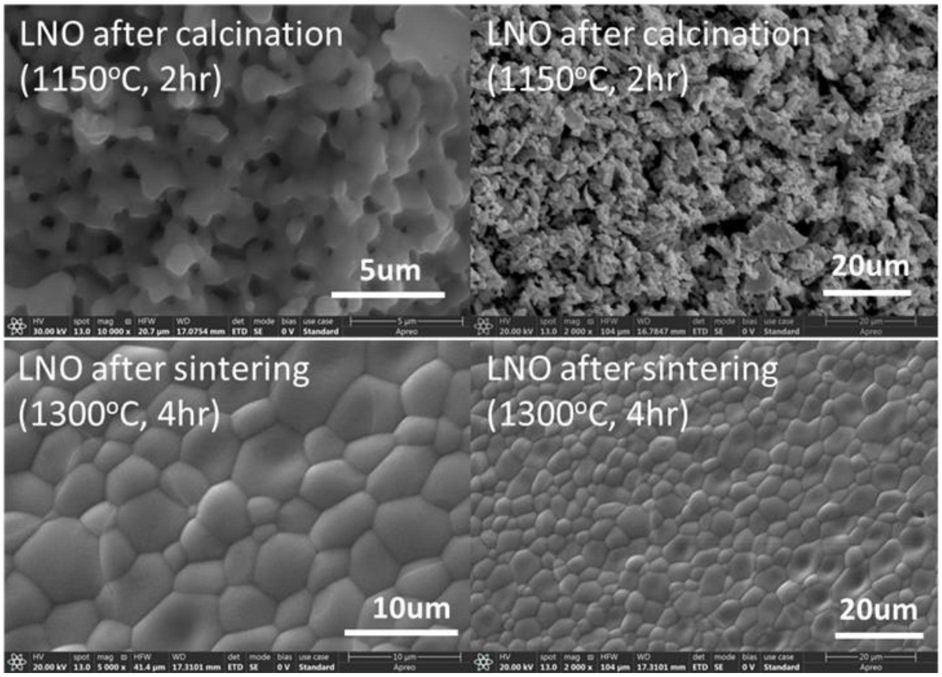

**Figure 7.4 Sr doped LaNiO3 (x = 0)**

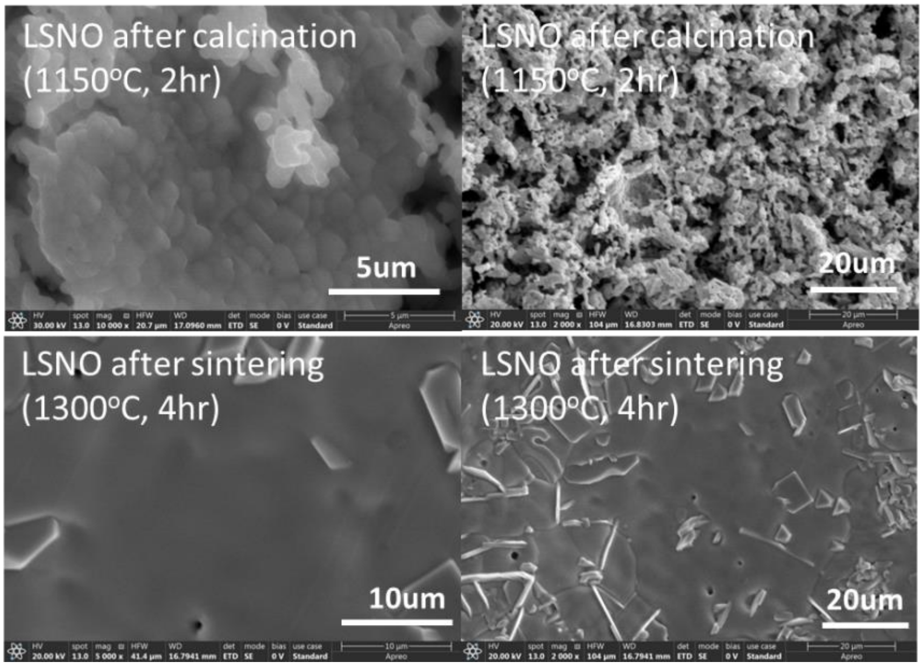

**Figure 7.5 Sr doped LaNiO3 (x = 0.3)**

Figure7.6 presents the top view (a) and cross section (b) of LSF coating after sintering at 1400$_{o}$C. The density of LSF layer is dense enough to block gas.

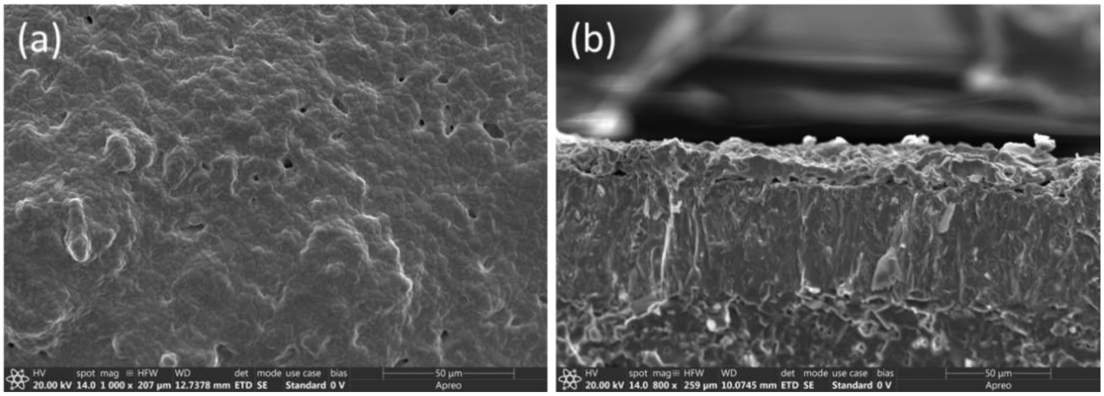

**Figure 7.6 LSF after sintering at 1400$_{o}$C**

It is worth noting that p-type coating, such as LSM or LSF, may have side chemical reaction with anode support, YSZ-NiO in reducing ambiance. As shown in the Figure 7.7, second phase is found in the mixture of LSF and YSZ:NiO power. Thereby, if n-type layer is capable to eliminate the reaction between p-type and anode support effectively, the lifetime of the whole structure is promising to be increased.

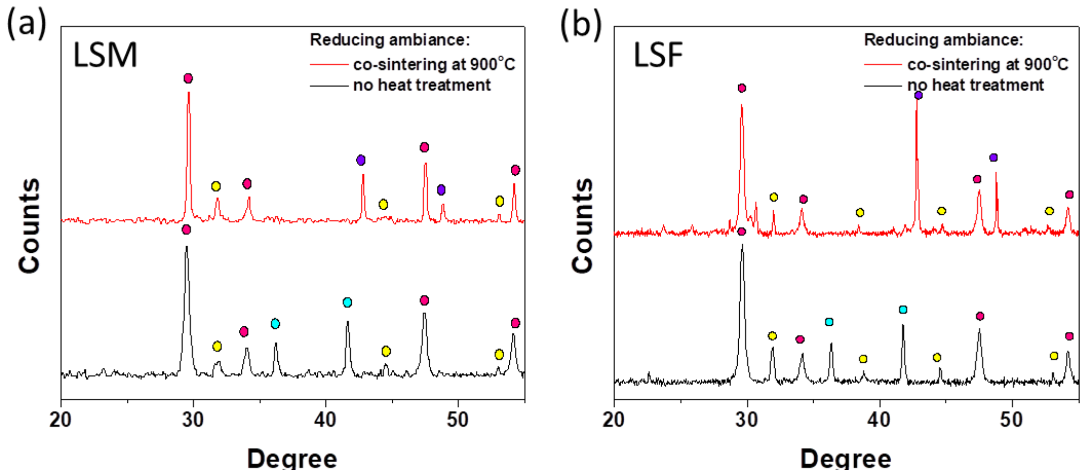

**Figure 7.7 Phase stability of (a) LSM, (b) LSF powder mixed with YSZ:NiO after heat treatment at $900_{o}$C in forming gas**

### 7.2.3 ZnO Shell Thickness Effect on Optical Properties

As presented in Figure, the overall thickness of nanowires turns to around 65nm. In Fig(c), the AgNW networks are completely covered by Al:ZnO and form a AgNWs/ZnO thin films.

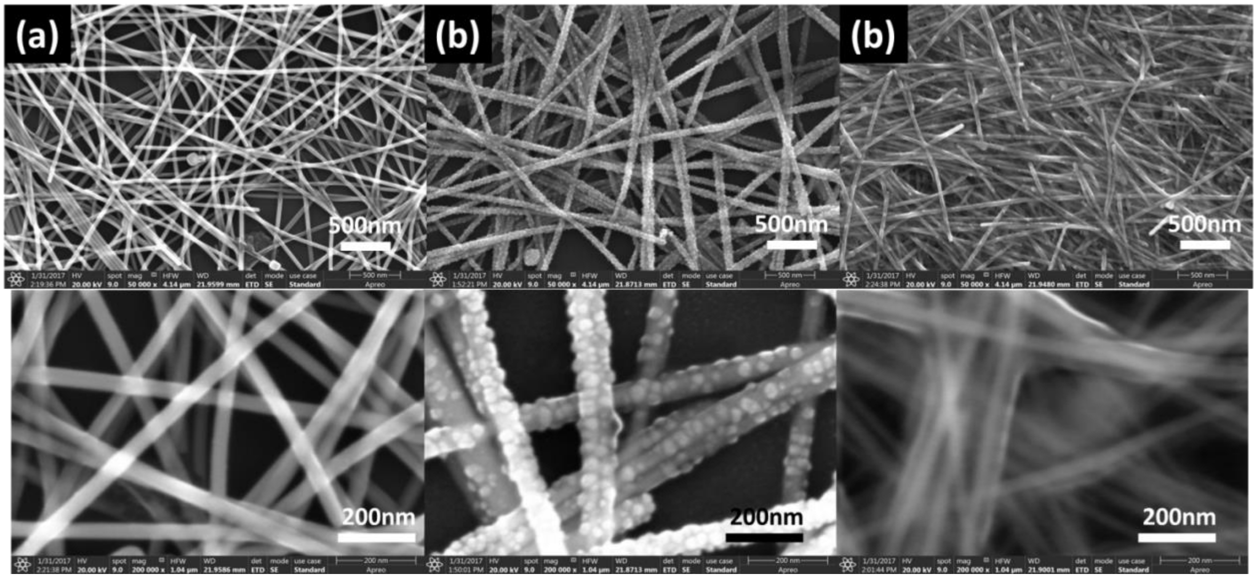

**Figure 7.8 SEM images for: (a) Ag NW networks w/o Al:ZnO; (b) Ag NWs capped with thin layer Al:ZnO; (c) AgNWs covered with Al:ZnO thin films**

According to the Figure7.8 (a), AgNWs capped thin layer Al:ZnO provides a higher transmittance than AgNWs/Al:ZnO thin films. Also, the transmittance is competitive with pure AgNWs networks in visible light range. This phenomenon can be explained using Mie theory calculation. The scattering and extinction for AgNWs, AgNW capped with AZO and AgNW covered totally with AZO are plotted in Figure7.8(b). Al:ZnO have influence on reducing the extinction and scattering in the visible light ranged >500nm, which also matches with our experimental measurement shown in Figure7.8(a).

This improvement can be explained using Mie theory for spheres or cylinders: [193-194]

$$C_{ext} = C_{abs} + C_{scatt} = \frac{12\pi k}{a^3}\frac{\varepsilon_m \mathrm{Im}(\varepsilon)}{|\varepsilon-\varepsilon_m|2}|\alpha|^2 + \frac{8\pi}{3}k^4|\alpha|^2 \tag{7-4}$$

$$\varepsilon_{eff} = \varepsilon_{AZO}\frac{(1+2f\beta_{Ag-AZO})}{(1-f\beta_{Ag-AZO})} \tag{7-5}$$

$$\alpha_{eff} = (r_{Ag}+d_{AZO})^3\frac{\varepsilon_{eff}-\varepsilon_m}{\varepsilon_{eff}+2\varepsilon_m} \tag{7-6}$$

, where Cabs and Cscatt represents the absorption and scattering cross-sections. a is a radius-related parameter. k is the wavenumber in the medium, ε is the permittivity. α is the electrostatic polarizability. The effective permittivity and electrostatic polarizability would change with Al:ZnO capping. The calculation was done in FDTD Lumerical software.

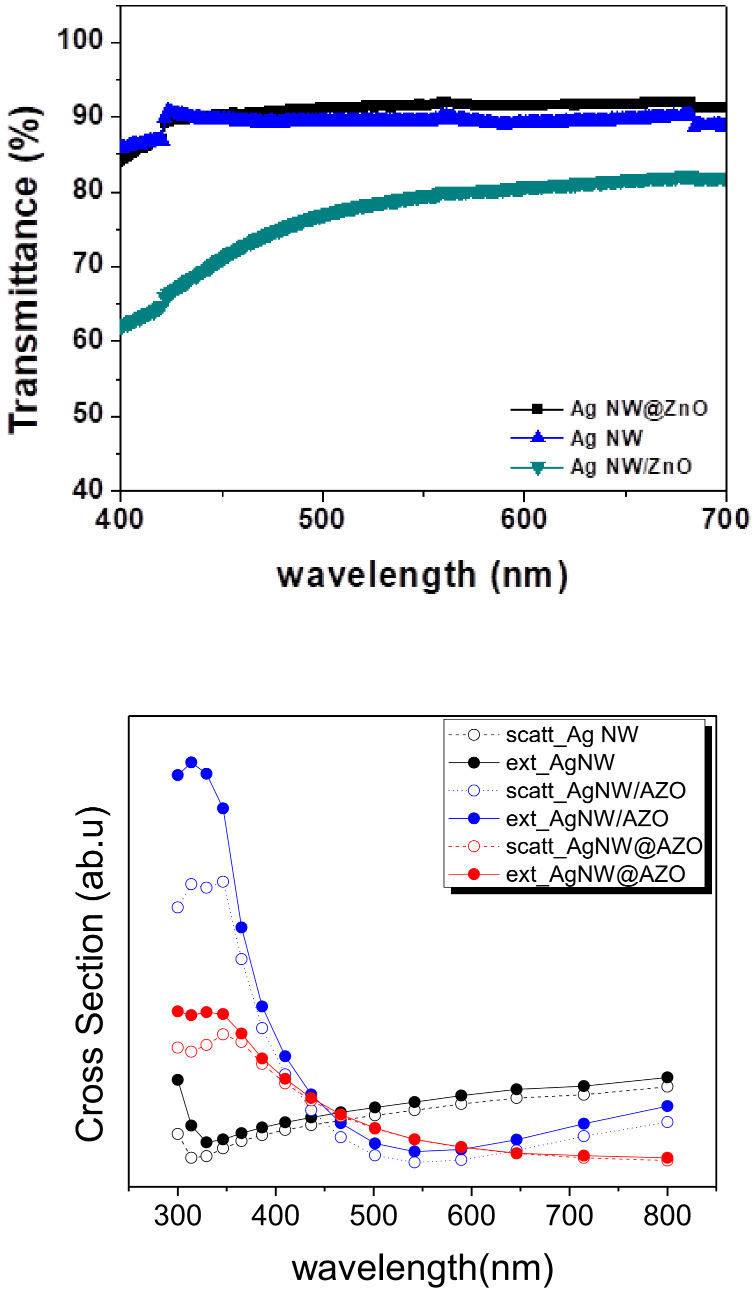

**Figure 7.9 (a) UV-vis spectrum on transmittance of AgNWs networks in three capping conditions; (b) simulation cross-section using Mie theory**

# Bibliography

[1] Technological Learning in the Transition to a Low-Carbon Energy System. (2020). Technological Learning in the Transition to a Low-Carbon Energy System. https://doi.org/10.1016/c2018-0-04547-8

[2] Zhang, M. M., Wang, Q., Zhou, D., & Ding, H. (2019). Evaluating uncertain investment decisions in low-carbon transition toward renewable energy. Applied Energy, 240, 1049–1060. https://doi.org/10.1016/j.apenergy.2019.01.205

[3] IRENA (2018). (2018). Renewable Power Generation Costs in 2017. International Renewable Energy Agency. https://doi.org/10.1007/SpringerReference_7300

[4] Bhatia, S. C. 1 - Energy Resources and Their Utilisation. In Advanced Renewable Energy Systems; Bhatia, S. C., Ed.; Woodhead Publishing India: 2014; pp 1-31.

[5] Gifford, R. Natural Environmental Psychology. In International Encyclopedia of the Social & Behavioral Sciences; Smelser, N. J.; Baltes, P. B., Eds.; Pergamon: Oxford, 2001; pp 10384-10388.

[6] Ren, H.; Chae, J. 2 - Fuel Cells Technologies for Wireless Mems. In Wireless Mems Networks and Applications; Uttamchandani, D., Ed.; Woodhead Publishing: 2017; pp 35-51.

[7] Keith Scott, Chapter 1:Introduction to Electrolysis, Electrolysers and Hydrogen Production , in Electrochemical Methods for Hydrogen Production, 2019, pp. 1-27

[8] Neaman, D. A. (2012). Semiconductor Physics and Devices: Basic Principles, Fourth Edition. McGraw-Hill. DOI:10.1016/B978-075067499-7/50001-8

[9] Torrance, J. B.; Lacorro, P.; Asavaroengchai, C.; Metzger, R. M. Simple and Perovskite Oxides of Transition-Metals: Why Some Are Metallic, While Most Are Insulating. Journal of Solid State Chemistry 1991, 90 (1), 168-172, DOI: https://doi.org/10.1016/0022-4596(91)90182-H.

[10] Siqueira, G., Belardi, R.-M., Almeida, P., Silva, C., Brant, M., Matencio, T., & Domingues, R. (2012). Determination of the Mn3+/Mn4+ ratio in La1−xSrxMnO3±d powders. Journal of Alloys and Compounds, 521, 50–54. https://doi.org/10.1016/j.jallcom.2012.01.023

[11] Jiang, S. (2008). Development of Lanthanum Strontium Manganite Perovskite Cathode Materials of Solid Oxide Fuel Cells: A Review. Journal of Materials Science, 43, 6799–6833. https://doi.org/10.1007/s10853-008-2966-6

[12] Larring, Y., & Norby, T. (2000). Spinel and Perovskite Functional Layers Between Plansee Metallic Interconnect (Cr-5 wt % Fe-1 wt % Y[sub 2]O[sub 3]) and Ceramic (La[sub

0.85]Sr[sub 0.15])[sub 0.91]MnO[sub 3] Cathode Materials for Solid Oxide Fuel Cells. Journal of The Electrochemical Society, 147(9), 3251. https://doi.org/10.1149/1.1393891

[13] Issa, B., Obaidat, I., Albiss, B., & Haik, Y. (2013). Magnetic Nanoparticles: Surface Effects and Properties Related to Biomedicine Applications. International Journal of Molecular Sciences, 14, 21266–21305. https://doi.org/10.3390/ijms141121266

[14] Mogensen, M. B.; Chen, M.; Frandsen, H. L.; Graves, C.; Hansen, J. B.; Hansen, K. V.; Hauch, A.; Jacobsen, T.; Jensen, S. H.; Skafte, T. L.; Sun, X. Reversible Solid-Oxide Cells for Clean and Sustainable Energy. Clean Energy 2019, 3 (3), 175-201, DOI: 10.1093/ce/zkz023

[15] Minh, N. Q.; Mogensen, M. B. Reversible Solid Oxide Fuel Cell Technology for Green Fuel and Power Production. Interface magazine 2013, 22 (4), 55-62, DOI: 10.1149/2.f05134if

[16] Przybylski, K.; Brylewski, T.; Durda, E.; Gawel, R.; Kruk, A. Oxidation Properties of the Crofer 22 Apu Steel Coated with La0.6sr0.4co0.2fe0.8o3 for It-Sofc Interconnect Applications. Journal of Thermal Analysis and Calorimetry 2014, 116 (2), 825-834, DOI: 10.1007/s10973-013-3594-1.

[17] Falk-Windisch H., Svensson J.E., Froitzheim J. The Effect of Temperature on Chromium Vaporization and Oxide Scale Growth on Interconnect Steels for Solid Oxide Fuel Cells. J. Power Sources. 2015;287:25–35. doi: 10.1016/j.jpowsour.2015.04.040.

[18] Payne, R.; Love, J.; Kah, M. Generating Electricity at 60% Electrical Efficiency from 1 - 2 Kwe Sofc Products. ECS Transactions 2009, 25, DOI: 10.1149/1.3205530

[19] Stadler, A. Transparent Conducting Oxides-an up-to-Date Overview. Materials (Basel) 2012, 5 (4), 661-683, DOI: 10.3390/ma5040661.

[20] Granqvist, C. G. Transparent Conductive Electrodes for Electrochromic Devices: A Review. Applied Physics A 1993, 57 (1), 19-24, DOI: 10.1007/BF00331211.

[21] Klein, A.; Körber, C.; Wachau, A.; Säuberlich, F.; Gassenbauer, Y.; Harvey, S. P.; Proffit, D. E.; Mason, T. O. Transparent Conducting Oxides for Photovoltaics: Manipulation of Fermi Level, Work Function and Energy Band Alignment. Materials (Basel) 2010, 3 (11), 4892-4914, DOI: 10.3390/ma3114892.

[22] Schumann, T.; Raghavan, S.; Ahadi, K.; Kim, H.; Stemmer, S. Structure and Optical Band Gaps of (Ba,Sr)Sno3 Films Grown by Molecular Beam Epitaxy. Journal of Vacuum Science & Technology A 2016, 34 (5), 050601, DOI: 10.1116/1.4959004.

[23] Minami, T. Substitution of Transparent Conducting Oxide Thin Films for Indium Tin Oxide Transparent Electrode Applications. Thin Solid Films 2008, 516 (7), 1314-1321, DOI: 10.1016/j.tsf.2007.03.082.

[24] Cao, W. R.; Li, J.; Chen, H. Z.; Xue, J. Transparent Electrodes for Organic Optoelectronic Devices: A Review. Journal of Photonics for Energy 2014, 4, DOI: 10.1117/1.JPE.4.040990.

[25] Huang, P.-S., Qin, F., Xiong, Z., Shim, H.-W., Gao, T., Leu, P., & Lee, J.-K. (2017). Novel Carrier Doping Mechanism for Transparent Conductor: Electron Donation from Embedded Ag Nanoparticles to the Oxide Matrix. ACS Applied Materials & Interfaces, 9(23), 19973–19979. https://doi.org/10.1021/acsami.7b03871

[26] Cao, W., Li, J., Chen, H., & Xue, J. (2014). Transparent electrodes for organic optoelectronic devices: a review. Journal of Photonics for Energy, 4(1), 1–28. https://doi.org/10.1117/1.JPE.4.040990

[27] Da Silveira Petruci, J. F.; Piccoli, J. P.; Fortes, P. R.; Cardoso, A. A. Chapter 14 - Nanomaterials in Air Pollution Trace Detection. In Nanomaterials Applications for Environmental Matrices; Nascimento, R. F. d.; Ferreira, O. P.; De Paula, A. J.; Sousa Neto, V. d. O., Eds.; Elsevier: 2019; pp 427-447.

[28] Wang, C.; Yin, L.; Zhang, L.; Xiang, D.; Gao, R. Metal Oxide Gas Sensors: Sensitivity and Influencing Factors. Sensors (Basel) 2010, 10 (3), 2088-2106, DOI: 10.3390/s100302088.

[29] Wu, X.; Xing, Y.; Pierce, D.; Zhao, J. X. One-Pot Synthesis of Reduced Graphene Oxide/Metal (Oxide) Composites. ACS Applied Materials & Interfaces 2017, 9 (43), 37962-37971, DOI: 10.1021/acsami.7b12539.

[30] Liu, C.-T.; Wang, Y.-C.; Dong, R.-X.; Wang, C.-C.; Huang, K.-C.; Vittal, R.; Ho, K.-C.; Lin, J.-J. A Dual-Functional Pt/Cnt Tco-Free Counter Electrode for Dye-Sensitized Solar Cell. J. Mater. Chem. 2012, 22, 25311-25315, DOI: 10.1039/C2JM35102A.

[31] Valenti, M., Jonsson, M. P., Biskos, G., Schmidt-Ott, A., & Smith, W. A. (2016). Plasmonic nanoparticle-semiconductor composites for efficient solar water splitting. Journal of Materials Chemistry A, 4(46), 17891–17912. https://doi.org/10.1039/C6TA06405A

[32] Banin, U., Ben-Shahar, Y., & Vinokurov, K. (2014). Hybrid Semiconductor–Metal Nanoparticles: From Architecture to Function. Chemistry of Materials, 26(1), 97–110. https://doi.org/10.1021/cm402131n

[33] Ablat, A., Kyndiah, A., Houin, G., Alic, T. Y., Hirsch, L., & Abbas, M. (2019). Role of Oxide/Metal Bilayer Electrodes in Solution Processed Organic Field Effect Transistors. Scientific Reports, 9(1), 6685. https://doi.org/10.1038/s41598-019-43237-z

[34] Fraser, D. B., & Cook, H. D. (1972). Highly Conductive, Transparent Films of Sputtered In[sub 2−x]Sn[sub x]O[sub 3−y]. Journal of The Electrochemical Society, 119(10), 1368. https://doi.org/10.1149/1.2403999

[35] Haacke, G. (1976). New figure of merit for transparent conductors. Journal of Applied Physics, 47(9), 4086–4089. https://doi.org/10.1063/1.323240

[36] Yan, X., Li, W., Aberle, A. G., & Venkataraj, S. (2015). Surface texturing studies of bilayer transparent conductive oxide (TCO) structures as front electrode for thin-film silicon solar cells. Journal of Materials Science: Materials in Electronics, 26(9), 7049–7058. https://doi.org/10.1007/s10854-015-3326-3

[37] Influence of Au thickness on the optical and electrical properties of transparent and conducting TiO2/Au/TiO2 multilayer films, Opt. Commun., 283 (2010), pp. 1792-1794

[38] Hu, L., Kim, H. S., Lee, J.-Y., Peumans, P., & Cui, Y. (2010). Scalable Coating and Properties of Transparent, Flexible, Silver Nanowire Electrodes. ACS Nano, 4(5), 2955–2963. https://doi.org/10.1021/nn1005232

[39] Kwon, J., Suh, Y. D., Lee, J., Lee, P., Han, S., Hong, S., … Ko, S. H. (2018). Recent progress in silver nanowire based flexible/wearable optoelectronics. Journal of Materials Chemistry C, 6(28), 7445–7461. https://doi.org/10.1039/C8TC01024B

[40] Yang, M., Kim, S. W., Zhang, S., Park, D. Y., Lee, C.-W., Ko, Y.-H., … Li, M. (2018). Facile and highly efficient fabrication of robust Ag nanowire–elastomer composite electrodes with tailored electrical properties. Journal of Materials Chemistry C, 6(27), 7207–7218. https://doi.org/10.1039/C8TC01691G

[41] Kim, A., Won, Y., Woo, K., Kim, C.-H., & Moon, J. (2013). Highly Transparent Low Resistance ZnO/Ag Nanowire/ZnO Composite Electrode for Thin Film Solar Cells. ACS Nano, 7(2), 1081–1091. https://doi.org/10.1021/nn305491x

[42] Yokokawa H, Sakai N, Horita T, Yamaji K, Brito ME (2005) Mater Res Soc Bull 30:591

[43] A. J. Darbandi, T. Enz and H. Hahn, "Synthesis and Characterization of Nanoparticulate Films for Intermediate Temperature Solid Oxide Fuel Cells," Solid State Ionics, Vol. 180, No. 4-5, 2009, pp. 424-430. doi:10.1016/j.ssi.2009.01.004

[44] M. Izumi, Y. Murakami, Y. Konishi, T. Manako, M. Ka- wasaki and Y. Tokura, "Structure Characterization and Magnetic Properties of Oxide Superlattices La0.6Sr0.4MnO3/La0.6Sr0.4FeO3," Physical Review B, Vol. 60, No. 20, 1999, pp. 1211-1215. doi:10.1103/PhysRevB.60.1211

[45] Kakihana M, Arima M, Yoshimura M, Ikeda N and Sugitani Y. Synthesis of high surface area LaMnO3+δ by a polymerizable complex method. Journal of Alloys and Compounds. 1999; 283(1-2):102-105.

[46] Xia CR, Zhang YL, Liu ML. LSM-GDC composite cathodes derived from a sol-gel process: Effect of microstructure on interfacial polarization resistance. Electrochem Solid-State Lett 2003;6:A290–A292.

[47] Jouannaux, J., Haeussler, A., Drobek, M., Ayral, A., Abanades, S., & Julbe, A. (2019). Lanthanum manganite perovskite ceramic powders for CO2 splitting: Influence of Pechini synthesis parameters on sinterability and reactivity. Ceramics International, 45(12), 15636–15648. https://doi.org/https://doi.org/10.1016/j.ceramint.2019.05.075

[48] Marinsek M, Zupan K, Razpotnik T, Macek J. A co-precipitation procedure for the synthesis of LSM material. Mater Technol 2007;41:85–90.

[49] Turky, A. O., Rashad, M. M., Hassan, A. M., Elnaggar, E. M., & Bechelany, M. (2017). Optical, electrical and magnetic properties of lanthanum strontium manganite La1−xSrxMnO3 synthesized through the citrate combustion method. Physical Chemistry Chemical Physics, 19(9), 6878–6886. https://doi.org/10.1039/C6CP07333F

[50] Jiang SP, Zhang JP, Foger K (2003) J Eur Ceram Soc 23:1865. doi:10.1016/S0955-2219(02)00447-8

[51] Banerjee, A., Pal, S., Rozenberg, E., & Chaudhuri, B. K. (2001). Adiabatic and non-adiabatic small-polaron hopping conduction in La1−xPbxMnO3+δ(0.0 ≤x≤ 0.5)-type oxides above the metal–semiconductor transition. Journal of Physics: Condensed Matter, 13(42), 9489–9504. https://doi.org/10.1088/0953-8984/13/42/310

[52] Geneste, G., Amadon, B., Torrent, M., & Dezanneau, G. (2017). DFT+ U study of self-trapping, trapping, and mobility of oxygen-type hole polarons in barium stannate. Physical Review B, 96. https://doi.org/10.1103/PhysRevB.96.134123

[53] Effect of Ca2+ and Sr2+ doping on the microstructure and cell performance of samaria-doped ceria electrolytes used in solid oxide fuel cells. June 2016 International Journal of Hydrogen Energy 41(31)DOI: 10.1016/j.ijhydene.2016.06.172

[54] Gude, V. G., Patil, P., Martinez-Guerra, E., Deng, S., & Khandan, N. (2013, June 6). Microwave energy potential for biodiesel production. Sustainable Chemical Processes. https://doi.org/10.1186/2043-7129-1-5

[55] F. J. Humphreys and M. Hatherly (1995); Recrystallization and related annealing phenomena, Elsevier

[56] Fernández van Raap, M. B., Coral, D. F., Yu, S., Muñoz, G. A., Sánchez, F. H., & Roig, A. (2017). Anticipating hyperthermic efficiency of magnetic colloids using a semi-empirical model: a tool to help medical decisions. Physical Chemistry Chemical Physics, 19(10), 7176–7187. https://doi.org/10.1039/C6CP08059F

[57] Chae, S. Y., Park, M. K., Lee, S. K., Kim, T. Y., Kim, S. K., & Lee, W. I. (2003). Preparation of Size-Controlled TiO2 Nanoparticles and Derivation of Optically Transparent Photocatalytic Films. Chemistry of Materials, 15(17), 3326–3331. https://doi.org/10.1021/cm030171d

[58] Faiyas, A. P. A., E. M., V., Joseph, J., Ganesan, R., & Pandey, R. K. (2010). Dependence of pH and surfactant effect in the synthesis of magnetite (Fe3O4) nanoparticles and its properties. Journal of Magnetism and Magnetic Materials, 322, 400–404. https://doi.org/10.1016/j.jmmm.2009.09.064

[59] Wilson, G. J., Matijasevich, A. S., Mitchell, D. R. G., Schulz, J. C., & Will, G. D. (2006). Modification of TiO2 for Enhanced Surface Properties: Finite Ostwald Ripening by a

MicrowaveHydrothermalProcess.Langmuir,22(5),2016–2027. https://doi.org/10.1021/la052716j

[60] Emin, D., & Holstein, T. (1969). Studies of small-polaron motion IV. Adiabatic theory of the Hall effect. Annals of Physics,53(3),439–520.https://doi.org/https://doi.org/10.1016/0003-4916(69)90034-7

[61] Wang, C. B., Shen, Y. J., Zhu, Y. X., & Zhang, L. M. (2015). Transport properties of La1−xSrxMnO3 ceramics above metal–insulator transition temperature. Physica B: Condensed Matter, 461, 57–60.https://doi.org/https://doi.org/10.1016/j.physb.2014.12.015

[62] van Roosmalen JAM, Cordfunke EHP, Helmholdt RB, Zandbergen HW (1994) J Solid State Chem 110:100. doi:10.1006/ jssc.1994.1141

[63] Mitchell JF, Argyriou DN, Potter CD, Hinks DG, Jorgensen JD, Bader SD (1996) Phys Rev B 54:6172. doi:10.1103/PhysRevB. 54.6172

[64] Alonso JA, Martinez-Lope MJ, Casais MT, MacManus-Driscoll JL, de Silva P, Cohen LF, Fernandez Diaz MT (1997) J Mater Chem 7:2139. doi:10.1039/a704088a

[65] Huang Q, Santoro A, Lynn JW, Erwin RW, Borchers JA, Peng JL et al (1997) Phys Rev B 55:14987. doi:10.1103/PhysRevB. 55.14987

[66] De Souza RA, Islam MS, Ivers-Tiffee E (1999) J Mater Chem 9:1621. doi:10.1039/a901512d

[67] van Roosmalen JAM, Cordfunke EHP (1994) J Solid State Chem 110:106. doi:10.1006/jssc.1994.1142

[68] Zheng F, Pederson LR (1999) J Electrochem Soc 146:2810. doi: 10.1149/1.1392012

[69] Mizusaki J, Mori N, Takai H, Yonemura Y, Minamiue H, Tagawa H et al (2000) Solid State.

[70] S. C. Singhal and K. Kendall, Editors, High Temperature Solid Oxide Fuel Cells: Fundamentals, Design and Applications, Elsevier, Oxford, UK (2003).

[71] Yang, Z. Recent Advances in Metallic Interconnects for Solid Oxide Fuel Cells. International Materials Reviews 2008, 53 (1), 39-54, DOI: 10.1179/174328007X212526.

[72] Zhou, X.-Y.; Huang, B.-L.; Zhang, T.-Y. Size- and Temperature-Dependent Young's Modulus and Size-Dependent Thermal Expansion Coefficient of Thin Films. Physical Chemistry Chemical Physics 2016, 18 (31), 21508-21517, DOI: 10.1039/C6CP03294J.

[73] Robinson, J. B.; Brown, L. D.; Jervis, R.; Taiwo, O. O.; Heenan, T. M. M.; Millichamp, J.; Mason, T. J.; Neville, T. P.; Clague, R.; Eastwood, D. S.; Reinhard, C.; Lee, P. D.; Brett, D. J. L.; Shearing, P. R. Investigating the Effect of Thermal Gradients on Stress in Solid Oxide Fuel Cell Anodes Using Combined Synchrotron Radiation and Thermal Imaging. Journal of Power Sources 2015, 288, 473-481, DOI: https://doi.org/10.1016/j.jpowsour.2015.04.104

[74] A Study on Sintering Inhibition of La0.8 Sr0.2 MnO3-∂ Cathode Material for Cathode-Supported Fuel Cells. Journal of the Korean Ceramic Society 2016; 53(5): 494-499.September 30, 2016 DOI: https://doi.org/10.4191/kcers.2016.53.5.494

[75] T. M. Barnes, M. O. Reese, J. D. Bergeson, B. A. Larsen, J. L. Blackburn, M. C. Beard, J. Bult, J. v. d. Lagemaat, Advanced Energy Materials, vol. 2, pp. 353-360, 2012.

[76] Viswanathan, V.; Wang, F. Y.-F. Theoretical Analysis of the Effect of Particle Size and Support on the Kinetics of Oxygen Reduction Reaction on Platinum Nanoparticles. Nanoscale 2012, 4 (16), 5110-5117, DOI: 10.1039/C2NR30572K.

[77] Li, L.; Abild-Pedersen, F.; Greeley, J.; Nørskov, J. K. Surface Tension Effects on the Reactivity of Metal Nanoparticles. The Journal of Physical Chemistry Letters 2015, 6 (19), 3797-3801, DOI: 10.1021/acs.jpclett.5b01746.

[78] Luo, X., Yang, Y., Yang, Y., Tian, D., Lu, X., Chen, Y., … Lin, B. (2017). Reduced-temperature redox-stable LSM as a novel symmetrical electrode material for SOFCs. Electrochimica Acta, 260. https://doi.org/10.1016/j.electacta.2017.11.071

[79] . H. Kuo, H. U. Anderson, and D. M. Sparlin,Journal of Solid State Chemistry,87,55 (1990).

[80] J. Mizusaki, N. Mori, H. Takai, Y. Yonemura, H. Minamiue, H. Tagawa, M. Dokiya,H. Inaba, K. Naraya, T. Sasamoto, and T. Hashimoto,Solid State Ionics,129,163(2000).

[81] H. Kamata, J. Mizusaki, H. Tagawa, K. Narayat, and T. Sasamotot,Joural of Physicsand Chemistry Solids,87,943(1995).

[82] Kaliaguine, S., Neste, A., Szabo, V., Gallot, J. E., Bassir, M., & Muzychuk, R. (2001). Perovskite-type oxides synthesized by reactive grinding: Part I. Preparation and characterization. Applied Catalysis A: General, 209, 345–358. https://doi.org/10.1016/S0926-860X(00)00779-1

[83] Hammami, R., Aïssa, S., & Habib, B. (2009). Effects of thermal treatment on physico-chemical and catalytic properties of lanthanum manganite LaMnO3+y. Applied Catalysis A: General, 353, 145–153. https://doi.org/10.1016/j.apcata.2008.10.048

[84] Alonso, J., Martínez-lope, M., Casais, M., MacManus-Driscoll, J., Silva, P., Cohen, L., & Fernández-díaz, M. (1997). Nonstoichiometry, structural defects and properties of LaMnO3+δ with high δ values (0.11≤δ≤0.29). Journal of Materials Chemistry - J MATER CHEM, 7, 2139–2144. https://doi.org/10.1039/a704088a

[85] Mizusaki, J., Arai, K., & Fueki, K. (1983). Ionic conduction of the perovskite-type halides. Solid State Ionics, 11(3), 203–211. https://doi.org/https://doi.org/10.1016/0167-2738(83)90025-5

[86] Yasuda, I., & Hishinuma, M. (1996). Electrical Conductivity and Chemical Diffusion Coefficient of Strontium-Doped Lanthanum Manganites. Journal of Solid State Chemistry, 123(2), 382–390. https://doi.org/https://doi.org/10.1006/jssc.1996.0193

[87] (1992). Prediction of sintered density for bimodal powder mixtures. Metallurgical Transactions, 23, 1455–1465. https://doi.org/10.1007/BF02647329

[88] Suri, P., & Park, S. J. (2008). Review: Liquid Phase Sintering. Journal of Materials Science, 44, 1–39. https://doi.org/10.1007/s10853-008-3008-0

[89] Ramakrishnegowda, N. (2016). Development of Layered Mg-Ti Composites for Biomedical applications. https://doi.org/10.13140/RG.2.1.4330.7929

[90] Qiao, L., Zhou, H., Chen, K., & Fu, R. (2003). Effects of Li2O on the Low Temperature Sintering and Thermal Conductivity of AlN Ceramics. Journal of the European Ceramic Society, 23, 1517–1524. https://doi.org/10.1016/S0955-2219(02)00344-8

[91] Cherepanov, V. A.; Barkhatova, L. Y.; Voronin, V. I. Phase Equilibria in the La–Sr–Mn–O System. Journal of Solid State Chemistry 1997, 134 (1), 38-44.

[92] Yoon, H.; Kim, T.; Park, S.; Sammes, N. M.; Chung, J.-S. Stable Lsm/Lstm Bi-Layer Interconnect for Flat-Tubular Solid Oxide Fuel Cells. International Journal of Hydrogen Energy 2018, 43 (1), 363-372.

[93] Park, B.-K.; Kim, D.-W.; Song, R.-H.; Lee, S.-B.; Lim, T.-H.; Park, S.-J.; Park, C.-O.; Lee, J.-W. Design of a Dual-Layer Ceramic Interconnect Based on Perovskite Oxides for Segmented-in-Series Solid Oxide Fuel Cells. Journal of Power Sources 2015, 300, 318-324.

[94] van Roosmalen, J. A. M.; Cordfunke, E. H. P.; Huijsmans, J. P. P. Sinter Behaviour of (La, Sr)Mno3. Solid State Ionics 1993, 66 (3), 285-293, DOI: https://doi.org/10.1016/0167-2738(93)90418-3.

[95] Dong, X.; Wu, Z.; Chang, X.; Jin, W.; Xu, N. One-Step Synthesis and Characterization of La2nio4+Δ Mixed-Conductive Oxide for Oxygen Permeation. Industrial & Engineering Chemistry Research 2007, 46 (21), 6910-6915.

[96] Khalil, M. S.; Wahba, M. Sr-Substitution Effects on La-Nio3, Sol-Gel Synthesis, Structural and Electrical Properties. 2016, 59, 719-729.

[97] Li, X.; Xin, M.; Guo, S.; Cai, T.; Du, D.; Xing, W.; Zhao, L.; Guo, W.; Xue, Q.; Yan, Z. Insight of Synergistic Effect of Different Active Metal Ions in Layered Double Hydroxides on Their Electrochemical Behaviors. Electrochimica Acta 2017, 253.

[98] Huang, Z.; Zhou, W.; Ouyang, C.; wu, J.; Fei, Z.; Jingguo, H.; Gao, Y.; Chu, J. High Performance of Mn-Co-Ni-O Spinel Nanofilms Sputtered from Acetate Precursors. Scientific reports 2015, 5, 10899.

[99] Raju, K.; Nkosi, F. P.; Viswanathan, E.; Mathe, M. K.; Damodaran, K.; Ozoemena, K. I. Microwave-Enhanced Electrochemical Cycling Performance of the Lini0.2mn1.8o4 Spinel Cathode Material at Elevated Temperature. Physical Chemistry Chemical Physics 2016, 18 (18), 13074-13083.

[100] Timurkutluk, B., Timurkutluk, C., Mat, M., & Kaplan, Y. (2016). A Review on Cell/Stack Designs for High Performance Solid Oxide Fuel Cells. Renewable and Sustainable Energy Reviews, 56, 1101–1121. https://doi.org/10.1016/j.rser.2015.12.034

[101] Irshad, M., Siraj, K., Raza, R., Ali, A., Tiwari, D. P., Zhu, B., Rafique, A., Ali, A., Kaleemullah, M., & Usman, A. (2016). A Brief Description of High Temperature Solid Oxide Fuel Cell's Operation, Materials, Design, Fabrication Technologies and Performance. Applied Sciences, 6, 75. https://doi.org/10.3390/app6030075

[102] Boroomand, F., Wessel, E., Bausinger, H., & Hilpert, K. (2000). Correlation Between Defect Chemistry and Expansion During Reduction of Doped LaCrO3 Interconnects for SOFCs. Solid State Ionics, 129, 251–258. https://doi.org/10.1016/S0167-2738(99)00330-6

[103] Magdefrau, N., Chen, L., Sun, E., Yamanis, J., & Aindow, M. (2013). Formation of spinel reaction layers in manganese cobaltite – coated Crofer22 APU for solid oxide fuel cell interconnects. Journal of Power Sources, 227, 318–326. https://doi.org/10.1016/j.jpowsour.2012.07.091

[104] Mah, J., Muchtar, A., Somalu, M., & Ghazali, M. (2016). Metallic interconnects for solid oxide fuel cell: A review on protective coating and deposition techniques. International Journal of Hydrogen Energy. https://doi.org/10.1016/j.ijhydene.2016.03.195

[105] Sachitanand, R., Sattari, M., Svensson, J.-E., & Froitzheim, J. (2013). Evaluation of the oxidation and Cr evaporation properties of selected FeCr alloys used as SOFC interconnects. International Journal of Hydrogen Energy, 38, 15328–15334. https://doi.org/10.1016/j.ijhydene.2013.09.044

[106] Jiang, S., & XINBING, C. (2014). ChemInform Abstract: Chromium Deposition and Poisoning of Cathodes of Solid Oxide Fuel Cells - A Review. International Journal of Hydrogen Energy, 39, 505–531. https://doi.org/10.1016/j.ijhydene.2013.10.042

[107] Belitskus, D. (1989). Fabrication processes for ceramic composites. Materials & Design, 10(1), 2–9. https://doi.org/https://doi.org/10.1016/0261-3069(89)90028-9

[108] Sayer, M., & Sreenivas, K. (1990). Ceramic Thin Films: Fabrication and Applications. Science, 247(4946), 1056 LP – 1060. https://doi.org/10.1126/science.247.4946.1056

[109] Briscoe, E., & Ponton, C. B. (1986). Ceramics – the fabrication challenge. Materials Science and Technology, 2(9), 910–912. https://doi.org/10.1179/mst.1986.2.9.910

[110] Thorel, A. (2010). Tape Casting Ceramics for High Temperature Fuel Cell Applications.

[111] Costa, R., Hafsaoui, J., Oliveira, A., Grosjean, A., Caruel, M., Chesnaud, A., & Thorel, A. (2009). Tape casting of proton conducting ceramic material. Journal of Applied Electrochemistry, 39, 485–495. https://doi.org/10.1007/s10800-008-9671-7

[112] Norsker, H., & Danisch, J. (1991). Slip Casting (pp. 148–160). https://doi.org/10.1007/978-3-663-06867-9_7

[113] Pollinger, J. P., & Messing, G. L. (1985). Thermal Analysis of Organic Binders for Ceramic Processing BT - Advances in Materials Characterization II (R. L. Snyder, R. A. Condrate, & P. F. Johnson (eds.); pp. 359–370). Springer US. https://doi.org/10.1007/978-1-4615-9439-0_28

[114] Xu, X., Oliveira, M. I. L. L., Fu, R., & Ferreira, J. M. F. (2003). Effect of dispersant on the rheological properties and slip casting of concentrated sialon precursor suspensions. Journal of the European Ceramic Society, 23(9), 1525–1530. https://doi.org/https://doi.org/10.1016/S0955-2219(02)00349-7

[115] Ma, L., Huang, Y., Yang, J., LE, H. R., & Sun, Y. (2005). Effect of plasticizer on the cracking of ceramic green bodies in gelcasting. Journal of Materials Science - J MATER SCI, 40, 4947–4949. https://doi.org/10.1007/s10853-005-3873-8

[116] Malzbender, J. (2004). Mechanical and thermal stresses in multilayered materials. Journal of Applied Physics, 95, 1780–1782. https://doi.org/10.1063/1.1642289

[117] Jiang, S. (2008). Development of Lanthanum Strontium Manganite Perovskite Cathode Materials of Solid Oxide Fuel Cells: A Review. Journal of Materials Science, 43, 6799–6833. https://doi.org/10.1007/s10853-008-2966-6

[118] Neumann, A., & Walter, D. (2006). The Thermal Transformation from Lanthanum Hydroxide to Lanthanum Hydroxide Oxide. Thermochimica Acta - THERMOCHIM ACTA, 445, 200–204. https://doi.org/10.1016/j.tca.2005.06.013

[119] van Roosmalen, J. A. M., Huijsmans, J. P. P., & Plomp, L. (1993). Electrical conductivity in La1−xSrxMnO3+δ. Solid State Ionics, 66(3), 279–284. https://doi.org/https://doi.org/10.1016/0167-2738(93)90417-2

[120] Meixner, D., & Cutler, R. (2002). Low-temperature plastic deformation of a perovskite ceramic material. Solid State Ionics, 146, 285–300. https://doi.org/10.1016/S0167-2738(01)01028-1

[121] Yoon, M., Choi, B.-H., Song, R.-H., & Hwang, H. (2012). Fabrication and characterization of a dual layer ceramic interconnect on a porous NiO-YSZ anode support. Ceramics International, 38, 6843–6847. https://doi.org/10.1016/j.ceramint.2012.05.084

[122] Park, B.-K., Kim, D.-W., Song, R.-H., Lee, S.-B., Lim, T.-H., Park, S.-J., … Lee, J.-W. (2015). Design of a dual-layer ceramic interconnect based on perovskite oxides for segmented-in-series solid oxide fuel cells. Journal of Power Sources, 300, 318–324. https://doi.org/https://doi.org/10.1016/j.jpowsour.2015.09.082

[123] Powell, M. J. (1979). Site percolation in randomly packed spheres. Physical Review B, 20(10), 4194–4198. https://doi.org/10.1103/PhysRevB.20.4194

[124] Kupke, M., Wentzel, H.-P., & Karl, S. (1998). Electrically conductive glass fibre reinforced epoxy resin. Material Research Innovations, 2, 164–169. https://doi.org/10.1007/s100190050079

[125] Mutiso, R. M., Sherrott, M. C., Li, J., & Winey, K. I. (2012). Simulations and generalized model of the effect of filler size dispersity on electrical percolation in rod networks. Physical Review B, 86(21), 214306. https://doi.org/10.1103/PhysRevB.86.214306

[126] Balberg, I. (2017). Unified Model for Pseudononuniversal Behavior of the Electrical Conductivity in Percolation Systems. Physical Review Letters, 119(8), 80601. https://doi.org/10.1103/PhysRevLett.119.080601

[127] Ambrosetti, G. et al. “Solution of the Tunneling-Percolation Problem in the Nanocomposite Regime.” Physical Review B 81.15 (2010): n. pag. Crossref. Web.

[128] Boustimi, M., Baudon, J., Feron, P., & Robert, J. (2003). Optical Properties of Metallic Nanowires. Optics Communications, 220, 377–381. https://doi.org/10.1016/S0030-4018(03)01400-7

[129] Chen, C., & Ye, C. (2018). Metal Nanowires: Materials, Synthesis, Characterization, Applications (pp. 105–131). https://doi.org/10.1002/9783527804603.ch2_3

[130] Lee, S., Kim, J., Kim, E., Suh, M., & Koo, S. (2015). Preparation of silver nanowires for transparent conductive films. Journal of Ceramic Processing Research, 16, 32–36.

[131] Huang, Q., Lilley, C., Bode, M., & Divan, R. (2008). Electrical Properties of Cu Nanowires. In 2008 8th IEEE Conference on Nanotechnology, IEEE-NANO. https://doi.org/10.1109/NANO.2008.163

[132] Xia, Z.; Wen, W. Synthesis of Nickel Nanowires with Tunable Characteristics. Nanomaterials 2016, 6, 19.

[133] Chawake, N., Varanasi, R. S., Jaswanth, B., Pinto, L., Kashyap, S., Koundinya, N. T. B. N., Srivastav, A. K., Jain, A., Sundararaman, M., & Kottada, R. S. (2016). Evolution of morphology and texture during high energy ball milling of Ni and Ni-5wt%Cu powders. Materials Characterization, 120, 90–96. https://doi.org/https://doi.org/10.1016/j.matchar.2016.08.019

[134] A. Hughes, A. Atkinson and A. Chadwick, MRS Online Proc. Libr., 1984, 24, 27–37

[135] A. Atkinson, Rev. Mod. Phys., 1985, 57, 437–470

[136] DOI: 10.1039/C7CP00476A (Paper) Phys. Chem. Chem. Phys., 2017, 19, 9045-9052

[137] A.T. Chadwick, R.I. Taylor, Solid State Ionics 12 (1984) 343.

[138] X. Peng, D. Ping, T. Li, W. Wu, J. Electrochem. Soc. 145 (1998) 389.

[139] A.A. Moosa, S.J. Rothman, L.J. Nowicki, Oxid. Met. 24 (1985) 115

[140] S. Mrowec, Z. Grzesik, B. Rajchel, A. Gil and J. Dabek, J. Phys. Chem. Solids, 2005, 66, 115

[141] D. Caplan, M. Graham and M. Cohen, J. Electrochem. Soc., 1972, 119, 1205–1215

[142] Ovalı, D., Balcı, Ö., Ağaoğulları, D., & Öveçoğlu, L. (2019). Effects of oxide particles on the microstructural and mechanical properties of W-Ni-WB composites. Particulate Science and Technology, 1–7. https://doi.org/10.1080/02726351.2018.1539798

[143] Sun, D., Liang, C., Shang, J., Yin, J., Song, Y., Li, W., Liang, T., & Zhang, X. (2016). Effect of Y2O3 contents on oxidation resistance at 1150°C and mechanical properties at room temperature of ODS Ni-20Cr-5Al alloy. Applied Surface Science, 385, 587–596. https://doi.org/https://doi.org/10.1016/j.apsusc.2016.05.143

[144] Zhang, X., You, R., Li, D., Cao, T., & Huang, W. (2017). Reaction Sensitivity of Ceria Morphology Effect on Ni/CeO2 Catalysis in Propane Oxidation Reactions. ACS Applied Materials & Interfaces, 9(41), 35897–35907. https://doi.org/10.1021/acsami.7b11536

[145] Shabir, Z., Van der Giessen, E., Duarte, C. A., & Simone, A. (2011). The role of cohesive properties on intergranular crack propagation in brittle polycrystals. Modelling and Simulation in Materials Science and Engineering, 19(3), 35006. https://doi.org/10.1088/0965-0393/19/3/035006

[146] Jung, W.-H. (2009). Adiabatic small polaron hopping conduction in La0.7Nd0.3Mn0.8Cr0.2O3. Physica B: Condensed Matter, 404, 1953–1956. https://doi.org/10.1016/j.physb.2009.03.017

[147] N. Khoi, W. Smeltzer and J. Embury, J. Electrochem. Soc., 1975, 122, 1495–1503

[148] Giusti, G., Langley, D., Lagrange, M., Collins, R., Jiménez, C., Bréchet, Y., & Bellet, D. (2014). Thermal annealing effects on silver nanowire networks. Int. J. of Nanotechnology, 11, 785–795. https://doi.org/10.1504/IJNT.2014.063788

[149] Langley, D. (2014). Silver nanowire networks : effects of percolation and thermal annealing on physical properties.

[150] Cai, W., Cha, J., Mahmood, F., Connor, S., Christoforo, M., Cui, Y., Mcgehee, M., & Brongersma, M. (2012). Self-limited plasmonic welding of silver nanowire junctions. Nature Materials, 11, 241–249. https://doi.org/10.1038/nmat3238

[151] Hosseinzadeh Khaligh, H., & Goldthorpe, I. (2014). Hot-rolling nanowire transparent electrodes for surface roughness minimization. Nanoscale Research Letters, 9, 310. https://doi.org/10.1186/1556-276X-9-310

[152] Hu, L., Kim, H. S., Lee, J.-Y., Peumans, P., & Cui, Y. (2010). Scalable Coating and Properties of Transparent, Flexible, Silver Nanowire Electrodes. ACS Nano, 4(5), 2955–2963. https://doi.org/10.1021/nn1005232

[153] Du, H., Wan, T., Qu, B., Cao, F., Lin, Q., Chen, N., Lin, X., & Chu, D. (2017). Engineering Silver Nanowire Networks: From Transparent Electrodes to Resistive Switching Devices.

ACS Applied Materials & Interfaces, 9(24), 20762–20770. https://doi.org/10.1021/acsami.7b04839

[154] Nian, Q., Saei, M., Xu, Y., Sabyasachi, G., Deng, B., Chen, Y. P., & Cheng, G. J. (2015). Crystalline Nanojoining Silver Nanowire Percolated Networks on Flexible Substrate. ACS Nano, 9(10), 10018–10031. https://doi.org/10.1021/acsnano.5b03601

[155] Minami, T. (2013). Transparent Conductive Oxides for Transparent Electrode Applications. Semiconductors and Semimetals, 88, 159–200. https://doi.org/10.1016/B978-0-12-396489-2.00005-9

[156] Aloui, W., Ltaief, A., & Bouazizi, A. (2013). Transparent and conductive multi walled carbon nanotubes flexible electrodes for optoelectronic applications. Superlattices and Microstructures, 64, 581–589. https://doi.org/10.1016/j.spmi.2013.10.027

[157] Grilli, M., Sytchkova, A., Boycheva, S., & Piegari, A. (2013). Transparent and Conductive Al-Doped ZnO Films for Solar Cells Applications. Physica Status Solidi (A), 210. https://doi.org/10.1002/pssa.201200547

[158] K P, S., Shashikala, H., Dey, A., Sridhara, N., Sharma, A., & Barshilia, H. (2017). Highly transparent and conducting ITO/Ag/ITO multilayer thin films on FEP substrates for flexible electronics applications. Solar Energy Materials and Solar Cells, 172, 277–284. https://doi.org/10.1016/j.solmat.2017.08.001

[159] Yan, M. (2002). Experimental study of wide bandgap transparent conducting oxide thin films.

[160] Lokanc, Martin, Eggert, Roderick, and Redlinger, Michael. Thu . "The Availability of Indium: The Present, Medium Term, and Long Term". United States. doi:10.2172/1327212. https://www.osti.gov/servlets/purl/1327212.

[161] Stubhan, T., Krantz, J., Li, N., Guo, F., Litzov, I., Steidl, M., Richter, M., Matt, G., & Brabec, C. (2012). High fill factor polymer solar cells comprising a transparent, low temperature solution processed doped metal oxide/metal nanowire composite electrode. Solar Energy Materials and Solar Cells, 107, 248–251. https://doi.org/10.1016/j.solmat.2012.06.039

[162] Yu, H., Stapleton, A., Lewis, D., & Wang, L. (2016). High performance flexible metal oxide/silver nanowire based transparent conductive films by a scalable lamination-assisted solution method. Journal of Materiomics, 3. https://doi.org/10.1016/j.jmat.2016.11.003

[163] Kim, A., Won, Y., Woo, K., Kim, C.-H., & Moon, J. (2013). Highly Transparent Low Resistance ZnO/Ag Nanowire/ZnO Composite Electrode for Thin Film Solar Cells. ACS Nano, 7(2), 1081–1091. https://doi.org/10.1021/nn305491x

[164] Essam, I., Gaunt, D., & Guttmann, A. (2001). Percolation theory at the critical dimension. Journal of Physics A: Mathematical and General, 11, 1983. https://doi.org/10.1088/0305-4470/11/10/016

[165] Steinhögl, W., Schindler, G., Steinlesberger, G., & Engelhardt, M. (2002). Size-dependent resistivity of metallic wires in the mesoscopic range. Physical Review B, 66(7), 75414. https://doi.org/10.1103/PhysRevB.66.075414

[166] Tung, R. (2001). "Formation of an electric dipole at metal-semiconductor interfaces". Physical Review B. 64 (20): 205310.

[167] Smith, B. L., & Rhoderick, E. H. (1971). Schottky barriers on p-type silicon. Solid-State Electronics, 14(1), 71–75. https://doi.org/https://doi.org/10.1016/0038-1101(71)90049-9

[168] Gutmann, S., Conrad, M., Wolak, M., Beerbom, M., & Schlaf, R. (2012). Work function measurements on nano-crystalline zinc oxide surfaces. Journal of Applied Physics, 111, 123710–123717. https://doi.org/10.1063/1.4729527

[169] Huang, P.-S., Qin, F., Xiong, Z., Shim, H.-W., Gao, T., Leu, P., & Lee, J.-K. (2017). Novel Carrier Doping Mechanism for Transparent Conductor: Electron Donation from Embedded Ag Nanoparticles to the Oxide Matrix. ACS Applied Materials & Interfaces, 9(23), 19973–19979. https://doi.org/10.1021/acsami.7b03871

[170] Coblentz, D., Slinker, J., Lin, X.-M., & Sorensen, C. (2001). Light Scattering from Magnetic Dipoles.

[171] Mortazavi, D., Kouzani, A., Kaynak, A., & Duan, W. (2011). Nano-plasmonic biosensors: A review. 2011 IEEE/ICME International Conference on Complex Medical Engineering, CME 2011. https://doi.org/10.1109/ICCME.2011.5876700

[172] Gooch, J. (2011). Mie Theory (p. 463). https://doi.org/10.1007/978-1-4419-6247-8_7496

[173] K. Fuchs , Math. Proc. Cambridge 1938 , 34 , 100 – 108 .

[174] Kim, T., Canlier, A., Cho, C., Rozyyev, V., Lee, J.-Y., & Han, S. M. (2014). Highly Transparent Au-Coated Ag Nanowire Transparent Electrode with Reduction in Haze. ACS Applied Materials & Interfaces, 6. https://doi.org/10.1021/am502632t

[175] Menamparambath, M. M., Muhammed Ajmal, C., Kim, K. H., Yang, D., Roh, J., Park, H. C., Kwak, C., Choi, J.-Y., & Baik, S. (2015). Silver nanowires decorated with silver nanoparticles for low-haze flexible transparent conductive films. Scientific Reports, 5(1), 16371. https://doi.org/10.1038/srep16371

[176] Miccoli, I., Edler, F., Pfnür, H., & Tegenkamp, C. (2015). The 100th anniversary of the four-point probe technique: the role of probe geometries in isotropic and anisotropic systems. Journal of Physics: Condensed Matter, 27(22), 223201. https://doi.org/10.1088/0953-8984/27/22/223201

[177] Haacke G (1976) New figure of merit for transparent conductors. J ApplPhys 47(9):4086–4089

[178] Feng, C., Liu, K., Wu, J.-S., Liu, L., Cheng, J. G., Zhang, Y., Sun, Y., Li, Q., Fan, S., & Jiang, K. (2010). Flexible, Stretchable, Transparent Conducting Films Made from Superaligned Carbon Nanotubes. Advanced Functional Materials, 20, 885–891. https://doi.org/10.1002/adfm.200901960

[179] Caricato, A., Cesaria, M., Luches, A., Martino, M., Maruccio, G., Valerini, D., Catalano, M., Cola, A., Manera, M. G., Lomascolo, M., Taurino, A., & Rella, R. (2010). Electrical and optical properties of ITO and ITO/Cr-doped ITO films. Applied Physics A, 101, 753. https://doi.org/10.1007/s00339-010-5988-2

[180] Wang, B., Yoo, T., Lim, J., Sang, B.-I., Lim, D., Choi, W. K., Hwang, D. K., & Oh, Y.-J. (2014). Enhanced Light Scattering and Trapping Effect of Ag Nanowire Mesh Electrode for High Efficient Flexible Organic Solar Cell. Small, 11. https://doi.org/10.1002/smll.201402161

[181] Calderón, S., Escobar Galindo, R., Benito, N., Palacio, C., Cavaleiro, A., & Carvalho, S. (2013). Ag+ release inhibition from ZrCN-Ag coatings by surface agglomeration mechanism: Structural characterization. Journal of Physics D: Applied Physics, 46, 325303. https://doi.org/10.1088/0022-3727/46/32/325303

[182] Zhao, Y., Liu, T., Shi, Q., Yang, Q., Li, C., Zhang, D., & Zhang, C. (2018). Perovskite oxides La0.4Sr0.6CoxMn1-xO3 (x = 0, 0.2, 0.4) as an effective electrocatalyst for lithium—air batteries. Green Energy & Environment, 3(1), 78–85. https://doi.org/https://doi.org/10.1016/j.gee.2017.12.001

[183] Chen, W., Wen, T., Nie, H., & Zheng, R. (2003). Study of Ln0.6Sr0.4Co0.8Mn0.2O3-δ (Ln=La, Gd, Sm or Nd) as the cathode materials for intermediate temperature SOFC. Materials Research Bulletin, 38(8), 1319–1328. https://doi.org/https://doi.org/10.1016/S0025-5408(03)00143-0

[184] Ishihara, T., Wang, S., & Wu, K.-T. (2017). Highly active oxide cathode of La(Sr)Fe(Mn)O3 for intermediate temperature CO2 and CO2-H2O co-electrolysis using LSGM electrolyte. Solid State Ionics, 299, 60–63. https://doi.org/https://doi.org/10.1016/j.ssi.2016.09.013

[185] Yue, X., & Irvine, J. T. S. (2012). (La,Sr)(Cr,Mn)O3/GDC cathode for high temperature steam electrolysis and steam-carbon dioxide co-electrolysis. Solid State Ionics, 225, 131–135. https://doi.org/https://doi.org/10.1016/j.ssi.2012.06.015

[186] Kim, M., Yang, J., Medvedeva, J., Yelon, W., Parris, P., & James, W. (2008). Electronic structure of La 0.7 Sr 0.3 Mn 1− x Cu x O 3 (0.0≤ x ≤0.30). Journal of Physics: Condensed Matter, 20, 255228. https://doi.org/10.1088/0953-8984/20/25/255228

[187] Bednorz, J. G., & Müller, K. A. (1986). Possible highTc superconductivity in the Ba−La−Cu−O system. Zeitschrift Für Physik B Condensed Matter, 64(2), 189–193. https://doi.org/10.1007/BF01303701

[188] Ino, A., Kim, C., Mizokawa, T., Shen, Z.-X., Fujimori, A., Takaba, M., Tamasaku, K., Eisaki, H., & Uchida, S. (1999). Fermi Surface and Band Dispersion in La 2-xSrxCuO 4.

Journal of the Physical Society of Japan, 68(5), 1496–1499. https://doi.org/10.1143/JPSJ.68.1496

[189] Baijnath, Tiwari, D. P., & Basu, S. (2017). Synthesis and performance of La0.5Sr0.5CoO3 cathode for solid oxide fuel cells. Advanced Materials Letters, 8, 791–798. https://doi.org/10.5185/amlett.2017.6895

[190] Goudochnikov, P., & Bell, A. J. (2007). Correlations between transition temperature, tolerance factor and cohesive energy in 2+:4+ perovskites. Journal of Physics: Condensed Matter, 19(17), 176201. https://doi.org/10.1088/0953-8984/19/17/176201

[191] Choi, M., Posadas, A. B., Rodriguez, C. A., O’Hara, A., Seinige, H., Kellock, A. J., Frank, M. M., Tsoi, M., Zollner, S., Narayanan, V., & Demkov, A. A. (2014). Structural, optical, and electrical properties of strained La-doped SrTiO3 films. Journal of Applied Physics, 116(4), 43705. https://doi.org/10.1063/1.4891225

[192] Sun, X.-F., Guo, R.-S., & Li, J. (2008). Preparation and properties of yttrium-doped SrTiO3 anode materials. Ceramics International, 34(1), 219–223. https://doi.org/https://doi.org/10.1016/j.ceramint.2006.09.009

[193] Grehan, G., & Gouesbet, G. (1979). Mie theory calculations: new progress, with emphasis on particle sizing. Applied Optics, 18(20), 3489–3493. https://doi.org/10.1364/AO.18.003489

[194] Xu, H. (2005). Multilayered metal core-shell nanostructures for inducing a large and tunable local optical field. Physical Review B, 72(7), 73405. https://doi.org/10.1103/PhysRevB.72.073405